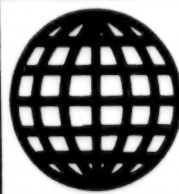


JPRS-CST-92-001

30 JANUARY 1992



FOREIGN
BROADCAST
INFORMATION
SERVICE

JPRS Report—

Science & Technology

China

JPRS-CST-92-001
30 JANUARY 1992

SCIENCE & TECHNOLOGY
CHINA

CONTENTS

AEROSPACE

Long March-4 Tracking System Detailed [Guo Fang; ZHONGGUO HANGTIAN, No 9, Sep 91].....	1
Complex-Ray Based Simulation, Optimization of EM Scattering From Engine Intakes [Ruan Yingzheng, Feng Wenlan; DIANZI XUEBAO, Vol 19 No 5, Sep 91].....	14
Status of, Prospects for Aerospace Applications of Composite Materials [Wang Manxia; ZHONGGUO HANGTIAN, No 8, Aug 91].....	22
Introduction to FY-1 Meteorological Satellite Data Receiving/Processing System [Fan Tianxi; ZHONGGUO KONGJIAN KEXUE JISHU, Vol 11 No 2, Apr 91].....	32

DEFENSE R&D

Optimal Design for Large-Caliber, Long-Range Artillery Projectiles [Tan Junjie; KONGQIDONGLIXUE XUEBAO, Vol 9 No 3, Sep 91].	43
--	----

ADVANCED MATERIALS

- Effect of SiC Whisker on Mechanical Strength of Si_3N_4
Matrix Composites
[Gu Peizhi, Xiao Yixin, et al.; GUI SUANYAN XUEBAO,
Vol 19 No 4, Aug 91]..... 52

LASERS, SENSORS, OPTICS

- Development of Flash X-Ray Machines at CAEP
[Tao Zucong, Zhang Shouyun, et al.; QIANG JIGUANG YU
LIZI SHU, Vol 3 No 3, Aug 91]..... 57
- VIRCATOR-Generated High Power Microwave Particle Simulation
[Shu Ting, Wang Min, et al.; QIANG JIGUANG YU LIZI
SHU, Vol 3 No 3, Aug 91]..... 65
- Flash-II: Relativistic Electron-Beam Accelerator
[Qiu Aici, Li Yuhu, et al.; QIANG JIGUANG YU LIZI
SHU, Vol 3 No 3, Aug 91]..... 77
- Satellite-Borne Remote Sensing System With CCD Camera, Data
Transmission Link
[Wang Mingyuan, Lin Kexiang; ZHONGGUO KONGJIAN KEXUE
JISHU, Vol 11 No 2, Apr 91]..... 88
- Gain-Guided GaAlAs/GaAs Phase-Locked Diode Laser Array
[Tu Yuzhen, Jin Zhiliang, et al.; ZHONGGUO JIGUANG,
Vol 18 No 8, Aug 91]..... 97
- Principle, Application of Twyman-Green Shearing Interferometer
[He Anzhi, Wang Hailin, et al.; ZHONGGUO JIGUANG,
Vol 18 No 10, Oct 91]..... 103
- PE-Calorimeter With Broad Spectra, High Sensitivity, and Fast
Response
[Zhou Fuzheng, Shen Liqing; ZHONGGUO JIGUANG, Vol 18
No 10, Oct 91]..... 109
- Development of High-Density Energy Storage Pulsed Capacitor
[Yuan Cunde, Han Aimei, et al.; ZHONGGUO JIGUANG,
Vol 18 No 10, Oct 91]..... 117

MICROELECTRONICS

- Picosecond Optical Pulse Generation at High Repetition Rate
by Gain-Switched Semiconductor Laser
[Sun Wei, Yi Maobin, et al.; BANDAOTI XUEBAO,
Vol 12 No 9, Sep 91]..... 120
- GaInAs/InP Quantum-Well Structures Grown by Low-Pressure MOVPE
[Duan Shukun, Xiong Feike, et al.; BANDAOTI XUEBAO,
Vol 12 No 9, Sep 91]..... 124

Long March-4 Tracking System Detailed

92FE0158A Beijing ZHONGGUO HANGTIAN [AEROSPACE CHINA] in Chinese No 9, Sep 91
pp 42-47

[Article by Guo Fang [6753 2397] of the Shanghai Space Electronic Equipment Design and Research Institute: "Long March-4 External Tracking/Safety System"]

[Text] Abstract

The Long March-4 (LM-4) launch vehicle has successfully launched two meteorological satellites, the FY-1A and FY-1B, into sun-synchronous orbit. The tracking system of the LM-4 is one of its key subsystems which can be linked to China's Space Telemetry Tracking and Control (TT&C) network; by obtaining trajectory data from the control stations of the TT&C network, the system is able to perform the tracking and measurement functions over the entire trajectory. The tracking accuracy of the system fully meets the overall design requirements of the launch vehicle. This article gives a brief description of the mission and composition of the tracking system and the operating principles of the major components on board the vehicle. In addition, the test results are also presented.

On 7 September 1988 and 3 September 1990, China's LM-4 launch vehicle successfully launched two meteorological satellites, the FY-1A and FY-1B, respectively, into sun-synchronous orbit from the Taiyuan Space Launch Center; these successful launches have demonstrated the LM-4's capability as a practical launch vehicle. Specifically, the LM-4 is capable of launching satellites into sun-synchronous orbit, geosynchronous orbit, or any other earth orbit.

The tracking system of the LM-4 is one of its key subsystems; it is designed to perform the LM-4's tracking and telemetry functions by coordinating with the control stations of China's Space TT&C network.

I. Description of the Telemetry and Control System of the LM-4 Launch Vehicle

1. Telemetry and Control Functions During Powered Flight

(1) Measuring the launch-vehicle drift as it leaves the launch tower during lift-off;

- (2) Tracking the rocket trajectory in real time from lift-off to orbit injection to provide monitoring and display information for the flight command center;
- (3) Monitoring the flight conditions of the first and second stages of the launch vehicle and providing the information to the safety officer for making real-time decisions to take appropriate measures if malfunctions occur in either stage with potentially grave consequences;
- (4) Measuring and recording the tracking data for post-flight analysis of the flight conditions and guidance accuracy;
- (5) Performing calculations and predictions of the initial satellite orbit.

2. Telemetry and Control Requirements During Powered Flight

- (1) To provide the raw data for determining the launch-vehicle drift as it leaves the launch tower during lift-off;
- (2) To provide real-time display of rocket positions, velocities, flight-path angles and predicted impact points along the trajectory from lift-off to stage separation; to provide real-time safety information and impact parameters from 60 seconds after lift-off to second-stage engine cut-off; to provide real-time information on third-stage flight trajectory and perigee height of satellite orbit;
- (3) Post-flight processing accuracy

During the period from 60 seconds after lift-off to second-stage engine cut-off:

$$\begin{aligned}\sigma_x = \sigma_y = \sigma_z &< 10\text{m} \\ \sigma_v = \sigma_j = \sigma_i &< 0.05\text{mps}\end{aligned}$$

and during the period from third-stage engine cut-off to satellite-rocket separation:

$$\sigma_i = \sigma_j = \sigma_z < 1\text{mps}$$

3. Composition of the Telemetry and Control System

Based on the overall design requirements of the launch vehicle, the telemetry and control system can receive data input from China's Space TT&C network--which includes tracking stations at the Taiyuan Space Launch Center and the Xian Space TT&C Center, as well as the ground stations at Yibin and Nanning--to perform its trajectory tracking and measurement functions. The system contains the following subsystems: measurement subsystem; safety and control subsystem; guidance subsystem; real-time data processing, monitoring and display subsystem; and communications, data transmission and time-integrated command and scheduling subsystem. The system components are shown in Figure 1 and the system layout is shown in Figure 2.

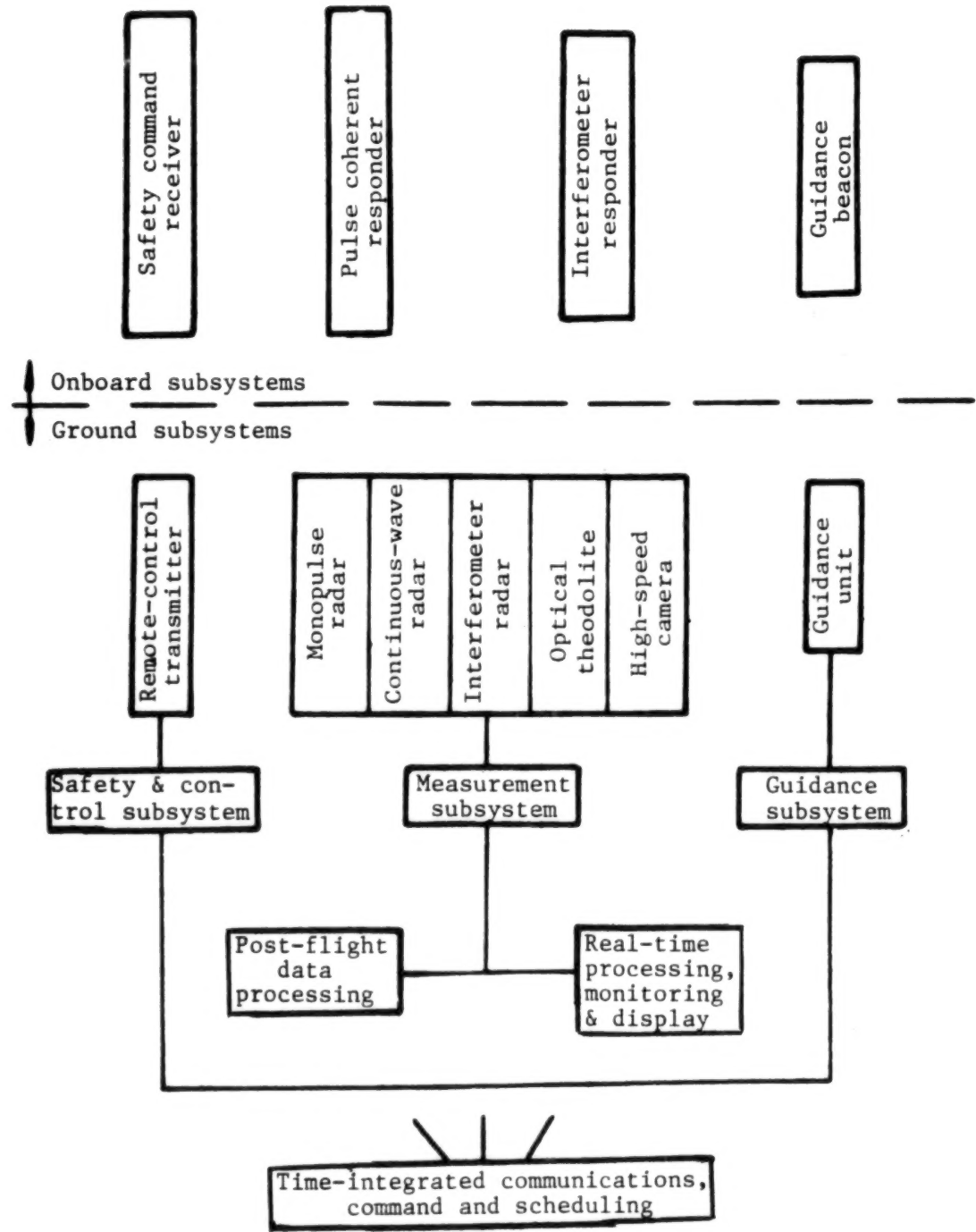
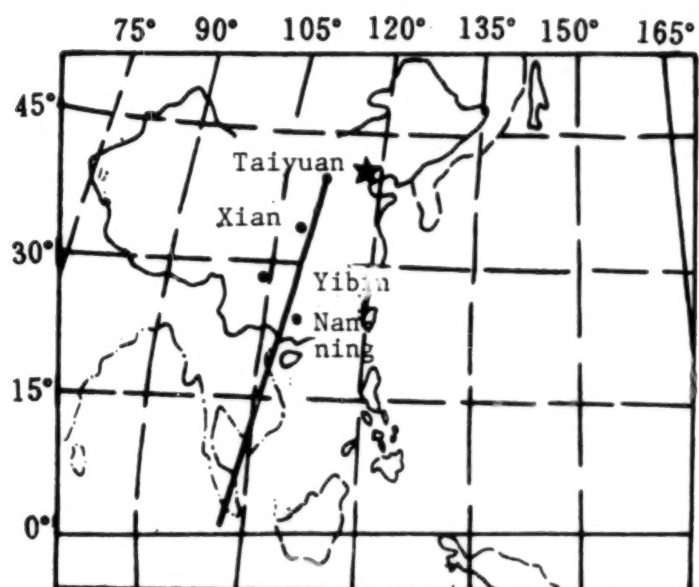


Figure 1. Components of the Telemetry and Control System



(a)

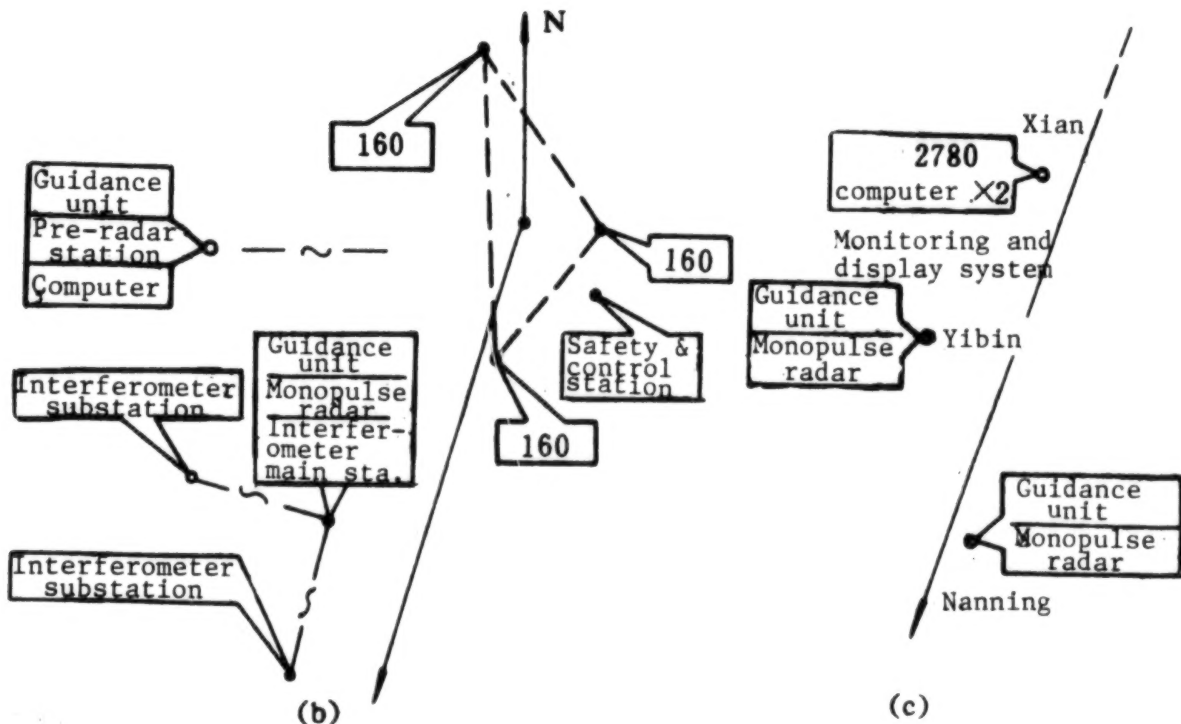


Figure 2. System Layout

- (a) Layout of tracking stations in the flight region
- (b) Layout of major components in the head
- (c) Layout of major components in the flight region

(1) Measurement Subsystem

The major components of the measurement subsystem include the high-speed cameras, the optical theodolites, the high-precision long-baseline interferometer system, the multi-station monopulse radar network and the onboard interferometer responder and pulse coherent responder.

-- High-speed cameras. Four 11-1 high-speed cameras are placed in the vicinity of the launch site to photograph the lift-off conditions of the launch vehicle for post-flight analysis of launch-vehicle drift during lift-off.

-- Optical theodolites. Three 160 optical theodolites are placed in the vicinity of the launch site to measure the range (R), azimuth (A) and elevation (E) of the launch vehicle within its field of view and to perform the functions of tracking and measurement during first-stage flight.

-- High-precision long-baseline interferometer system (comparable to the U.S. MISTRAM-1 system). It is designed to operate with the onboard interferometer to perform tracking and measurement functions over the entire trajectory; specifically, it provides high-precision safety and control information for the first and second stages and high-precision trajectory data for post-flight analysis. The original design requirements for the system are as follows: maximum range with guaranteed precision, 800 km, maximum unambiguous range 1920.24 km. In order to provide tracking capability beyond 2500 km, the following measures have been taken: 1) increasing the receiver sensitivity; 2) installing a microprocessor at the terminal unit to resolve range ambiguities greater than 1920.24 km, thus ensuring unambiguous range measurement at 2500 km; 3) increasing the antenna gain of the interferometer responder. In addition, the downlink frequency of the responder is received by the Yinchuan ground station (which is part of the Taiyuan Space Launch Center) to provide velocity information; measurements from the Yibin and Nanning stations are also incorporated into the long-baseline interferometer system to solve for the satellite-rocket separation parameters in order to improve the accuracy of predicting orbit injection.

-- Monopulse radar network. The monopulse radars at the Taiyuan Space Launch Center and at the Yibin and Nanning ground stations can share the same onboard pulse coherent responder to form a monopulse radar network; this network can be activated simultaneously by all three stations to provide extended tracking range. This radar network provides important information for predicting the initial satellite orbit and also provides information for the safety and control subsystem and the digital guidance subsystem.

(2) Safety and Control Subsystem

This subsystem processes the real-time information received from the measurement subsystem, displays various key parameters, and continuously monitors and assesses the flight conditions of the launch vehicle. Although the launch vehicle has been designed to self-destruct, its destruction is still controlled by the ground-based safety and control subsystem in order to

ensure the safety of cities and populated areas in the surrounding regions. When the first or second stage of the launch vehicle develops uncorrectable malfunctions, the safety officer or the computer will choose an appropriate time to issue the destruction command to blow up the vehicle in mid-air; at the same time, it will also compute the impact-point parameters of the main debris section of the destroyed vehicle.

The main components of the safety and control subsystem include the remote-control transmitter, the main monitoring station, the sub-monitoring station, the computer, the display equipment and the onboard safety command receiver (see Figure 3).

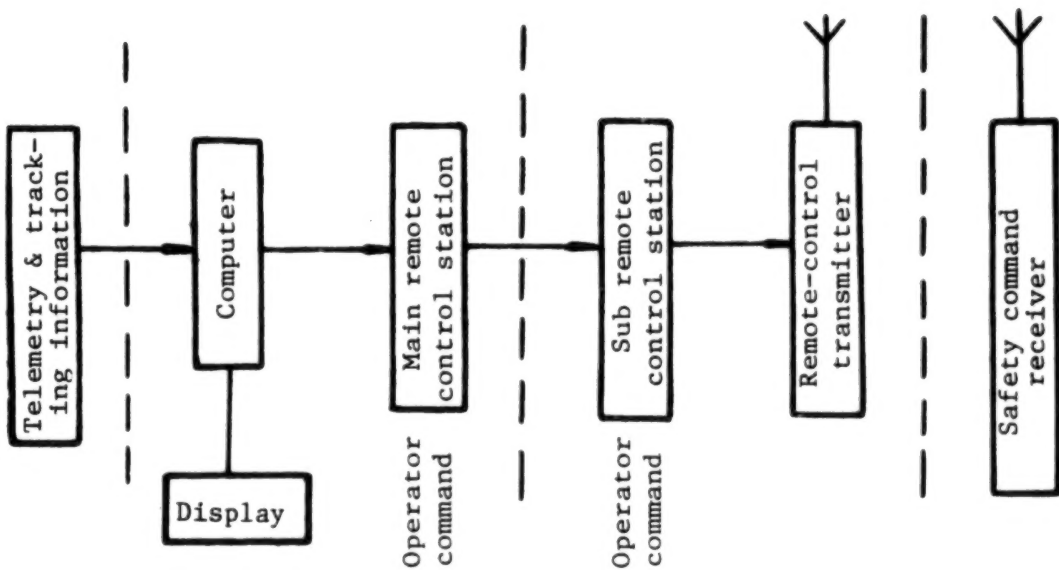


Figure 3. Block Diagram of the Safety and Control Subsystem

The control commands used by the subsystem include both computer-generated commands and operator commands; the computer is used to issue warnings, select impact points and issue destruction commands (in case the computer breaks down, then the destruction command can be issued directly by the operator). By taking advantage of the speed of the computer and the operator's ability to make real-time decisions in response to the actual environment, one can minimize the probability of destroying a good launch vehicle or failure to destroy a malfunctioning vehicle, and prevent sections of the debris from falling on populated areas.

(3) Guidance Subsystem

This subsystem can provide accurate and reliable guidance data to the various telemetry and control subsystems for timely target acquisition.

There are two guidance modes: analog and digital. The launch vehicle is equipped with a guidance beacon, which transmits guidance signals to the analog guidance units 161A (or B) located at the ground stations. The output

angle data, which are generated by the rotating transformer of the guidance beacon, are transmitted in the form of analog signals to the synchronizer or the rotating transformer of the guided unit.

Digital guidance is accomplished by exchanging real-time information between computers at the ground stations and the computer at the command and control center.

(4) Data Processing and Display Subsystem With Zoom Capability

The primary functions of this subsystem include:

- a) Processing real-time information received from the measurement subsystem and displaying various key parameters in different formats; also, continuously monitoring and assessing the flight conditions of the launch vehicle so that if malfunctions develop during first- or second-stage flight, a signal will be sent to the remote control unit to issue a destruction command, and to provide the estimated impact-point parameters in pseudo real time;
- b) Establishing a command procedure for conducting flight tests of the launch vehicle;
- c) Collecting and monitoring data on the flight conditions of the rocket and the operating conditions of the ground stations, and displaying the key parameters for subsequent stages;
- d) Transmitting real-time digital guidance information to the ground stations.

(5) Post-Flight Data Processing Subsystem

Its primary functions include:

- a) Data collection, editing, processing and compression;
- b) Reducing the effect of random errors and correcting for systematic errors;
- c) Solving for trajectory parameters of the launch vehicle and determining their mean square errors by incorporating all measured data.

II. Tracking/Safety System of the LM-4 Launch Vehicle

1. Primary Functions and Components of the System

(1) Primary Functions

Prior to satellite-rocket separation, this system coordinates with the telemetry and control system to perform real-time measurement and monitoring of the launch-vehicle trajectory.

After satellite-rocket separation, it continues to track the launch vehicle until the signal disappears.

If the launch vehicle develops uncorrectable malfunctions in its first or second stages, then the system will destroy the rocket in mid-air in response to either a destruction command issued by the safety and control subsystem or a signal transmitted by the launch vehicle indicating attitude instability.

(2) System Components

To perform the functions of trajectory measurement, safety and control, the system relies on the following components: the interferometer responder, the pulse coherent responder, the guidance beacon, the safety command receiver, the controller, the detonator and explosives, and the associated antennas, electric cables and batteries.

2. Description of the Major Components

-- The interferometer responder

The interferometer responder is a key component of the LM-4 tracking system. It operates in conjunction with the long-baseline interferometer system to perform high-precision tracking of the LM-4 launch vehicle, to verify the guidance accuracy of the control system, and to provide real-time data to the range safety system.

In an effort to correct some of the deficiencies of the initial design (an intermediate-frequency, or IF, responder design) such as large phase error, inter-channel interference, and low receiver sensitivity, a new phase-locked responder design has been adopted. In the new design, the tachometric channel f_{R1} is phase-locked, and the ranging channels $f_{R2} + PN_y$ and $f_{R3} + PN_x$ are IF transponded; a block diagram of the responder and the system signal design spectrum are shown in Figure 4 and Figure 5, respectively. The receive antenna is a right-hand circularly polarized (RHCP) microwave antenna and the transmit antenna is an LHCP antenna.

The outstanding feature of this responder is the simplicity of the phase-locked transponder design. It can be seen from Figure 4 that except for the ranging circuit, all uplink signals basically share the same channel. This design not only simplifies the circuitry and improves the reliability of the responder, but also increases the phase coherency of the signals and avoids inter-channel interference. As a result, the sensitivity of the responder, the phase accuracy, the on-off repeatability and the short-term frequency stability have all been significantly improved. Test results show that the tracking range of the interferometer exceeds 3500 km.

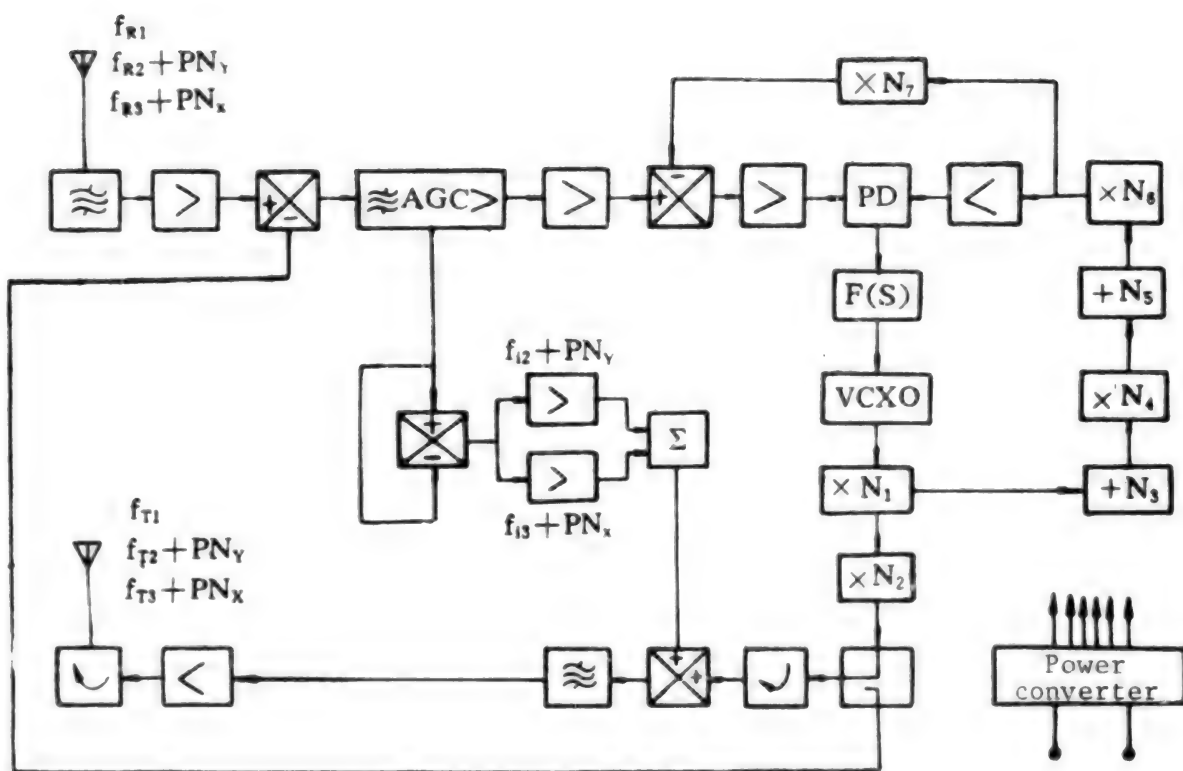


Figure 4. Block Diagram of the Interferometer Responder

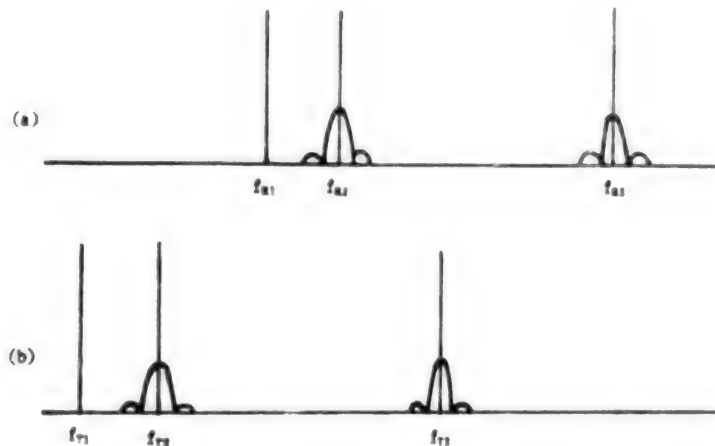


Figure 5. Designed Frequency Spectrum of the System Signal
 (a) Uplink signal spectrum; (b) Downlink signal spectrum

-- The pulse coherent responder

The pulse coherent responder is also an important component of the LM-4 tracking system. It operates with the monopulse radar network to perform the tracking and measurement functions over the entire trajectory; it also provides important data for predicting the initial orbit of the satellite.

A block diagram of the pulse coherent responder is shown in Figure 6. In order to activate the tracking radar network at the same time, logarithmic IF amplifiers and high-speed pulse modulation techniques have been used in the responder design to achieve fast response so that four monopulse radars can be activated simultaneously.

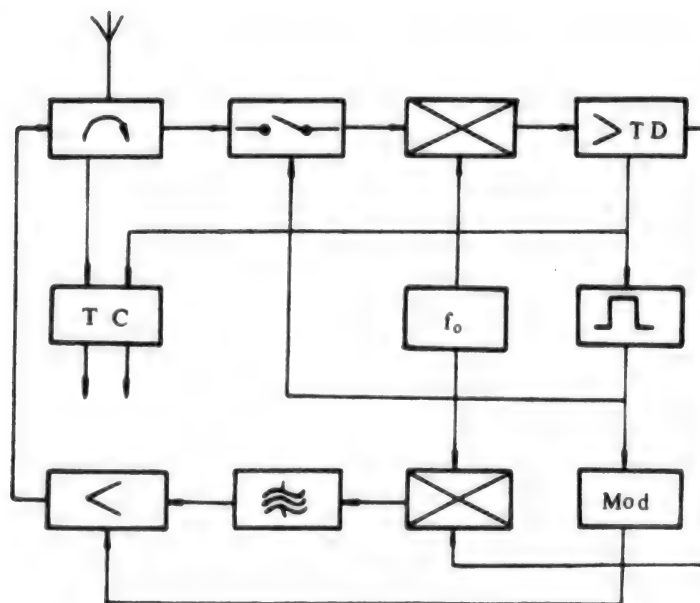


Figure 6. Block Diagram of the Pulse Coherent Responder

During the flight of the LM-4 launch vehicle, the pulse coherent responder and the monopulse tracking radar network jointly perform the tracking function over a duration of 422 seconds. Table 1 shows the operating range of the three monopulse radars.

Table 1. Operating Range of the Three Monopulse Radars

Name of radar station	Taiyuan Launch Center	Yibin	Nanning
Designed operating time (s)	40-675	210-675	290-675
Actual operating time (s)	26-756 ⁽¹⁾	180-790	300-919
	37-712 ⁽²⁾	180-813	290-815

(1) First data set collected in 1988.

(2) Second data set collected in 1990.

-- Microstrip antennas

The interferometer responder, the pulse coherent responder and the guidance beacon unit are all equipped with microstrip antennas. The pulse coherent

responder and the guidance beacon unit both use a single-element linearly polarized microstrip antenna, and the interferometer responder uses a four-element, circularly polarized microstrip antenna. These are wide-lobe, high-gain, easily fabricated antennas which share the same surface as the rocket body; the four-element circularly polarized antenna uses a polarization deflection design to increase the axial ratio at small angles with the rocket surface, thus improving the reliability of the tracking antenna.

III. Test Results

The test results of the LM-4 tracking system are summarized as follows:

1. Rocket Drift During Lift-Off

The maximum drift of the rocket tail section is derived by processing the data from the four high-speed cameras located near the launch site. The results are presented in Table 2.

Table 2. Maximum Drift of the Rocket Tail Section

Parameter	First test (1988.9.7)	Second test (1990.9.3)
Lift-off time (s)	6.18	6.58
Maximum drift of rocket tail section (m)	0.529	0.446

2. Measurement Accuracy

-- Optical measurement accuracy

Three 160 optical theodolites are used to perform trajectory measurements during the period from 20s-60s; the design values and the actual measurement accuracies are presented in Table 3.

Table 3. Optical Measurement Accuracy

Parameter	Design value	Actual measurement accuracy	
		First test	Second test
τ_x (m)	7.15~7.20	0.91~0.96	0.21~0.22
τ_y (m)	3.65~4.19	0.72~1.08	0.17~0.19
τ_z (m)	4.95~5.22	1.09~1.30	0.14~0.25
τ_i (mps)		0.053~0.056	0.009~0.025
τ_j (mps)		0.042~0.063	0.009~0.025
τ_z (mps)		0.064~0.076	0.007~0.037

-- Radar measurement and its accuracy

During the period from 60 seconds after lift-off to satellite-rocket separation, trajectory measurements are carried out using the high-precision long-baseline interferometer system supplemented by the monopulse radar network. The overall measurement requirements of the LM-4 launch vehicle and the actual measurement accuracy are presented in Table 4.

Table 4. Measurement Accuracy of the Interferometer System

Parameter	From 60 sec after lift-off to second-stage engine cut-off			From third-stage engine cut-off to satellite-rocket separation		
	Required value	Actual measurement accuracy		Required value	Actual measurement accuracy	
		First test	Second test		First test	Second test
r_x (m)	<10	0.498~2.491	0.10~2.13			
r_y (m)	<10	0.743~2.408	0.15~1.95			
r_z (m)	<10	0.788~2.891	0.14~2.70			
τ_x (mps)	<0.05	0.007~0.035	0.007~0.033	1	0.12~0.14	0.12~0.13
τ_y (mps)	<0.05	0.01~0.044	0.007~0.032	1	0.54~0.91	0.43~0.59
τ_z (mps)	<0.05	0.006~0.044	0.007~0.036	1	0.16~0.18	0.15~0.16

-- Satellite orbit parameters and their accuracy

One of the functions of the tracking system is to determine the initial orbit of the satellite. This is accomplished by combining the tracking data collected by the Nanning and Yibin ground stations and the stations at the Launch Center. The theoretical orbit parameters and the second-orbit parameters provided by the Xian Telemetry and Control Center, as well as orbit parameters calculated from the tracking data, are presented in Table 5.

IV. Concluding Remarks

Test results from the two flight tests of the LM-4 launch vehicle conducted at the Taiyuan Space Launch Center show that for a 900-km-high polar-orbit satellite, the overall tracking accuracy requirement can be satisfied by using a tracking system which consists of an onboard guidance beacon, a redundant interferometer responder and a pulse coherent responder operating in conjunction with China's space TT&C network (without relying on the tracking vessels, the Yuanwang). Such a tracking system is not only feasible and reliable, but also the most cost-effective. The test results have also demonstrated the reliability and accuracy of the LM-4 as a practical launch vehicle for injecting satellites into orbit.

Table 5. Satellite Orbit Parameters and Deviations

Parameter	Theoretical value	Second orbit	Calculated value
Period (s)	6171.6/6172.892	6166.359/6174.270	6166.356/6175.730
Inclination ($^{\circ}$)	99/98.90	99.109/98.9585	99.122/98.940
Eccentricity	0/0.000095	0.00243/0.00035	0.00273/0.000394
Perigee height (km)	901/897.221	883.024/896.449	891.373/897.275
Apogee height (km)	901/897.493	918.403/900.41	927.380/901.877
Deviation in period (s)	12/12	-5.241/1.378	-5.244/2.838
Deviation in inclination ($^{\circ}$)	0.12/0.12	0.109/0.0585	0.122/0.04
Deviation in eccentricity	0.005/0.005	0.00243/0.00035	0.00273/0.000394
Deviation in perigee (km)	40/40	-17.976/-0.772	-9.627/0.054
Deviation in apogee (km)	40/40	17.403/2.917	26.381/4.384

Complex-Ray Based Simulation, Optimization of EM Scattering From Engine Intakes

92FE0120A Beijing DIANZI XUEBAO [ACTA ELECTRONICA SINICA] in Chinese Vol 19 No 5, Sep 91 pp 22-26

[Article by Ruan Yingzheng [7086 4481 6927] and Feng Wenlan [7458 2429 3482] of the University of Electronic Science and Technology, Chengdu: "Simulation and Optimization of EM Scattering From Engine Intakes by Complex Rays"; MS received Feb 90, revised Nov 90. Project funded by State Education Commission and MMEI grants.]

[Text] Abstract

A method of calculating the far-field electromagnetic (EM) scattering from a concave cavity by using a set of complex source points to model the incident plane wave and applying the complex-ray paraxial approximation is presented. This method has been used in computer simulation and optimization of the radar cross section (RCS) of engine intakes. The method can also be used in the simulation of EM scattering from other complex objects.

I. Introduction

The entire intake of an aircraft generally produces very strong radar returns in the nose direction of the target. The phenomenon of EM scattering from such a large-aperture concave structure is difficult to simulate and the calculations require long computational time.

One of the approaches for analyzing this type of complex structure is the waveguide transmission-line method, where the large-aperture cavity is treated as an over-mode waveguide, and the modal method is used to calculate the field distribution over the aperture, from which the far-field distribution and the RCS can be obtained by integration.¹ However, for an actual engine intake whose aperture size is larger than tens of wavelengths, it would be a very tedious task to calculate the superpositions of hundreds or thousands of modal contributions, and the changing shape of the intake makes the analysis even more difficult.

Another approach is the classical method of geometric optics (G.O.). In this method, a set of incident geometric rays are constructed at the aperture, and

each ray is traced along its reflecting paths through the inner surface of the concave cavity to establish the scattering field at the aperture surface; integration of the field over the entire aperture then gives the far-field distribution.² But since the G.O. method provides the field values only along the rays, the distance between the incident rays should be less than $(0.1-0.2)\lambda$ in aperture field; for an aperture which is tens of wavelengths in size, this implies tedious ray-tracing and a large amount of computations.

In this paper, the incident plane wave is expanded into a field of Gaussian beams produced by a set of complex source points,³ and the simplified complex-ray paraxial approximation^{4,5} is used to calculate the far-field scattering of each Gaussian beam after multiple reflections inside the engine intake; by superimposing the contributions of the individual beams, the total field and RCS can be determined. Because the complex-ray paraxial approximation method provides the beam scattering field over a finite region, the number of complex source points can be an order of magnitude smaller than the number of rays used in the G.O. method; also, the paraxial approximation method provides the far-field distribution directly, thereby circumventing the intermediate of aperture integration. For this reason, this method can be easily applied in the numerical analysis and optimization of EM characteristics of engine intakes. In this paper, numerical results are presented for an engine intake with a rectangular aperture.

II. Complex Source-Point Expansion of Incident Plane Waves

Consider a uniform incident plane wave in the direction of positive z-axis; let the plane H at $z = z_0$ be a plane of complex source-point expansion. Any point $S_0 (x_0, y_0, z_0)$ on this plane can become a complex source point \tilde{S}_0 by analytic continuation; let its coordinates be

$$\tilde{x}_0 = x_0, \quad \tilde{y}_0 = y_0, \quad \tilde{z} = z_0 + jb \quad (1)$$

where b denotes the beamwidth parameter of the complex source points. Equation (1) indicates that the beam-peak direction coincides with the positive z-axis of the incident wave. For different source points on the H plane, only the coordinates \tilde{x}_0 and \tilde{y}_0 (or x_0 and y_0) vary; \tilde{z}_0 (i.e., z_0 and b) remain unchanged. By using the method of paraxial approximation, the field intensity at a given point $P(x, y, z_0)$ produced by the complex source point \tilde{S}_0 can be expressed as:⁶

$$G_0(x_0, y_0, x, y) = \frac{C \exp\{-k[(x-x_0)^2 + (y-y_0)^2]/2b\}}{\{1 - [(x-x_0)^2 + (y-y_0)^2]/b^2\}^{1/2}} \quad (2)$$

where C is a constant amplitude factor, and k is the wave number ($k = 2\pi/\lambda$). The above equation reveals that the amplitude distribution is a Gaussian function.

According to the extended Huygens-Fresnel principle in the complex domain,³ an incident plane wave with a constant amplitude E_i can be expressed as the linear superposition of all the source-point fields:

$$E_i = \int_{-\infty}^{\infty} \int_{-\infty}^{\infty} \tilde{W}(x_0, y_0) \tilde{G}_0(x_0, y_0; x, y) dx_0 dy_0 \quad (3)$$

where $\tilde{W}(x_0, y_0)$ are amplitude weighting functions of the complex source points. For a uniform plane wave, clearly $\tilde{W}(x_0, y_0) = \tilde{W}_0$, a complex constant.

In the case of an actual engine intake, because of the bunching effect of the complex rays and the complexity of the structure, not all the complex source points on the expansion plane will contribute to the scattering field; therefore, the infinite integral in the above equation can be replaced by a finite integral, and the continuous source distribution can be replaced by a set of equally spaced source points. Thus, the integral (3) can be written as a finite sum:

$$E_i = \tilde{W}_0 \Delta x_0 \Delta y_0 \sum_{m=1}^M \sum_{n=1}^N \tilde{G}(m \Delta x_0, n \Delta y_0; x, y) \quad (4)$$

where Δx_0 and Δy_0 are spacings between the source points, and $M \times N$ is the total number of effective scattering sources. Numerical results show that by properly selecting the expansion parameters b , Δx_0 , Δy_0 , M and N , the desired accuracy of source-point expansion can be achieved.⁷ For example, through an iterative fitting procedure on a computer, it is easy to achieve a relative error of less than 0.01 percent.⁸

III. Complex Ray-Tracing and Calculation of the Scattering Field

Consider an S-shaped intake pipe with a rectangular cross section, as shown in Figure 1; the smooth contour consists of two circular-arc segments and three straight-line segments. Except for the aperture surface, the walls and ends of the pipe are made of ideal electrically conducting metals. The aperture dimensions of the hollow pipe are $a \times b$; the three straight-line segments are respectively c , d and e ; the radius of the circular arc is r and the turn angle is α .

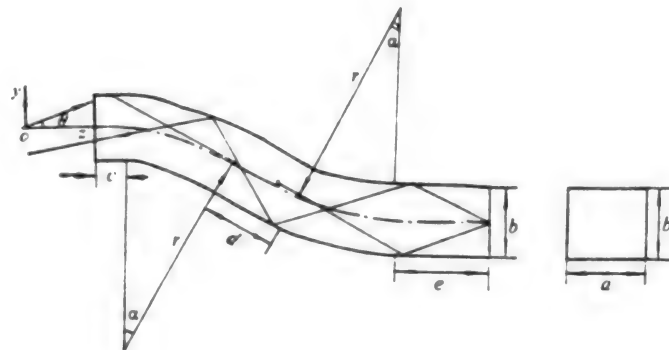


Figure 1. Model of the Engine Intake and the Ray Traces

Now assume that the incident wave is parallel to the yoz plane and makes an angle θ with the z -axis. By applying the complex source-point expansion, the multiple reflections of the ray axis of a particular complex source point can

be traced, as shown in Figure 1. The ray-tracing process is based on the linearity property of the complex axial rays,⁶ and can be programmed on a computer by applying the theorem of three-dimensional G.O. and replacing the curved interfaces by approximating tangential planes; the computer program also calculates various ray parameters.

The far-field contribution due to a point P_0 on the axial ray emanating from the aperture can be determined from the complex-ray theory:⁶

$$E_0(m, n; P_0) = \frac{A}{4\pi} \tilde{T}_{mn} \tilde{D}_{mn} \exp(jk\tilde{R}_{mn}) \quad (5)$$

where A is the constant amplitude factor of the scattering field of a unit complex source point; m, n are the sequence numbers of the source points; \tilde{T}_{mn} is the total complex reflection coefficient, whose absolute value for a metallic surface is defined as 1; \tilde{D}_{mn} is the total complex amplitude diffusion coefficient, which includes the natural diffusion factors and the diffusion factors caused by reflections at various interfaces of the curved surface; \tilde{R}_{mn} is the total optical path of the complex rays, i.e., the complex radius of curvature of the wavefront at the far-field observation point. These parameters can all be determined from the complex-ray theory.

Based on the complex-ray paraxial approximation, the field intensity at point P inside the far-field paraxial region can be expressed as:⁵

$$\tilde{E}(m, n; P) = \tilde{E}_0(m, n; P_0) \exp(jk\Delta\tilde{R}) \quad (6)$$

where $\Delta\tilde{R}$ is the complex phase correction factor between P_0 and P:

$$\Delta\tilde{R} \approx d^2/2(\tilde{R}_0 + R) \quad (7)$$

Here d denotes the off-axis distance from P_0 to P, \tilde{R}_0 is the complex radius of curvature of the wavefront emanating from the source point A on the intake aperture, and R is the ray path from point A to point P_0 .

The total field distribution of the incident wave through the intake pipe can be obtained by superposition of the scattering fields of all the complex source points:

$$E_i = \tilde{W}_0 \Delta x_0 \Delta y_0 \sum_{m=1}^M \sum_{n=1}^N \tilde{E}(m, n; P) \quad (8)$$

From this one can derive the RCS of the engine intake:

$$\sigma = 4\pi \lim_{R \rightarrow \infty} R^2 \frac{|E_i|^2}{|E_i|^2} \quad (9)$$

IV. Numerical Results

Based on the complex-ray expansion and paraxial approximation method, a general computer program consisting of approximately 2,000 lines of code

in C language has been written for calculating the RCS of an S-shaped rectangular intake pipe. To perform the ray-tracing of 121 points on an IBM-PC/XT microcomputer requires approximately 8 minutes of CPU time, which corresponds to approximately 4 seconds for each observation point.

Typical results of numerical computations and parameter optimization are presented in Figures 2-5. Figure 2 shows the RCS pattern of a straight pipe with square aperture ($a = b = 57$ mm, $c + d + e = 225$ mm, $\alpha = 0$) and horizontally polarized incident wave at X-band. The dotted curve and the solid curve are respectively the measured data and the calculated results using the waveguide modal method;¹ the dash-dot curve denotes the calculated results using the method proposed in this article. Within the range of observation angles $\theta < 40^\circ$, the results of this article are in better agreement with experimental data than the results calculated from the waveguide modal method.

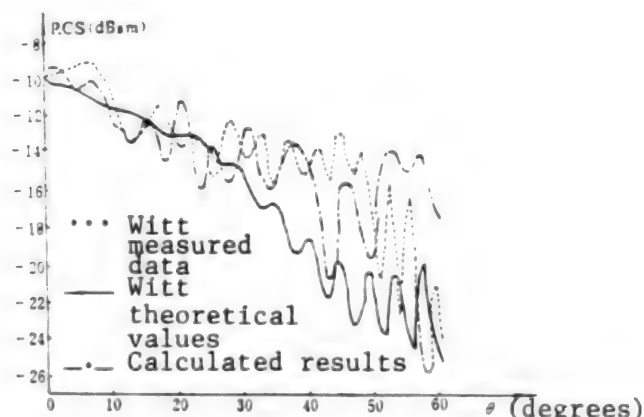


Figure 2. RCS Pattern of a Straight Square Pipe ($\lambda = 3.26$ cm, horizontal polarization)

Figure 3 shows the RCS pattern of a curved pipe with rectangular aperture ($a = 110$ mm, $b = 84$ mm, $c = 10$ mm, $d = 80$ mm, $e = 100$ mm, $r = 228$ mm, $\alpha = 35^\circ$) and horizontally polarized wave at X-band. The dotted curve is the calculated results of this article, the solid curve is the measured data, and the dash-dot curve is the calculated results using the waveguide modal method.⁸ It can be seen from the figure that the calculated results of this article are in good agreement with experimental data; both exhibit similar variations, and the relative error is less than 3 dB. On the other hand, the calculated results using the modal method deviate considerably from the measured values; the relative error is larger than 10 dB.

By varying the parameters of the S-shaped intake pipe, one can optimize the design by minimizing the RCS using the above procedure. Figure 4 shows the variation of the peak RCS with the turn angle α while keeping the total length of the pipe constant. It can be seen that the peak RCS can be significantly reduced by using a curved pipe in place of a straight pipe; for example, the RCS for $\alpha = 40^\circ$ is approximately 8 dB lower than that of a straight pipe.

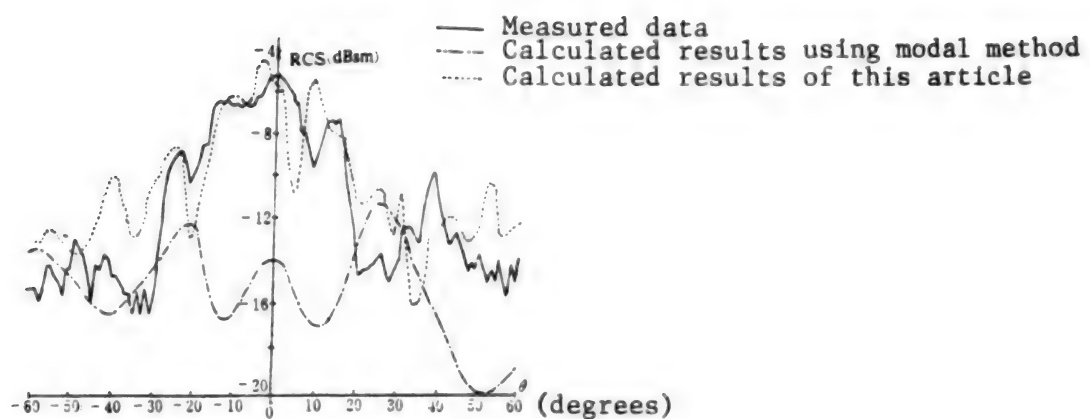


Figure 3. RCS Pattern of a Curved Rectangular Pipe ($\lambda = 3$ cm, horizontal polarization)

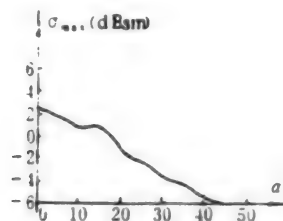


Figure 4. Effect of the Degree of Curvature of the Intake Pipe on RCS

Figure 5 shows the variation of the peak RCS with the width-to-height ratio (a/b) of the aperture while keeping the aperture area of the intake pipe constant; the minimum RCS value occurs at $a/b = 1.0-1.5$.

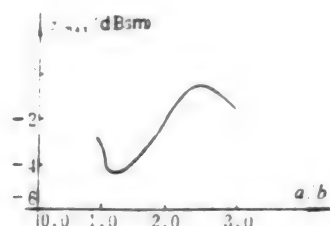


Figure 5. Effect of the Width-to-Height Ratio of the Intake Aperture on RCS

V. Discussion

In this analysis, the contribution of the diffraction field at the edge of the aperture has not been taken into account. This contribution in principle can be estimated using geometric theory of diffraction; however, for an actual engine intake whose aperture dimensions are more than an order-of-magnitude larger than the radar wavelength, the effect of edge diffraction in general can be neglected. In practice, the lip of the intake pipe with

finite thickness cannot be simulated using simple geometric diffraction technique; but given the geometric shape and other parameters of the lip, one can apply the method of this article to calculate the RCS contribution by direct reflections around the lip.

The procedure developed in this article for calculating the EM scattering from engine intakes is simple, efficient, accurate and robust, and can be used for aperture dimensions ranging from several wavelengths to several hundred wavelengths. As the aperture size increases, one can increase the spacings Δx_0 and Δy_0 between the source points and adjust the beamwidth parameter b in order to control the total computation time. By using three-dimensional complex scattering and paraxial approximation theory,⁹ this procedure can be extended to simulate EM scattering from intake pipes with circular or elliptical apertures, and to calculate RCS patterns in three-dimensional space.

Analysis of EM scattering using the method of complex-ray expansion and paraxial approximation provides an effective approach for predicting target RCS. In addition to engine intakes, this method can also be used to analyze the scattering from other complex objects such as reflector antennas,¹⁰ dielectric radomes,¹¹ sharp structures and wing-fuselage sections¹² and coated and structural wave-absorbing materials.¹³

References

1. H.R. Witt, E.L. Price, "Scattering From Hollow Conducting Cylinders," PROC. IEE, Vol 15, No 1, pp 94-99, 1968.
2. E.F. Knott, "A Progression of High-Frequency RCS Prediction Techniques," PROC. IEEE, Vol 73, No 2, pp 252-264, 1985.
3. Ruan Yingzheng, "Huygens Principle in Complex Space," CHENGDU DIANXUN GONGCHENG XUEYUAN XUEBAO [JOURNAL OF CHENGDU INSTITUTE OF RADIO ENGINEERING], Vol 16, No 1, pp 28-33, 1987.
4. Ruan Yingzheng, L.B. Felsen, "Principle and Application of Complex-Ray Paraxial Approximation," Applied Science Bulletin, Vol 7, No 2, pp 174-178, 1989.
5. Y.Z. Ruan, L.B. Felsen, "Reflection and Transmission of Beams at a Curved Interface," J. OPT. SOC. AM., A, Vol 3, No 4, pp 566-579, 1986.
6. Ruan Yingzheng, "Fundamentals of Electromagnetic Scattering Theory," Chengdu Institute of Radio Engineering Publishing House, 1989, Ch. 5.
7. Ruan Yingzheng, "Parameter Selection for Complex Huygens Source Expansion," DIANZI KEJI DAXUE XUEBAO [JOURNAL OF THE UNIVERSITY OF ELECTRONIC SCIENCE AND TECHNOLOGY], Vol 18, No 5, pp 456-461, 1989.
8. Feng Wenlan, "Radar Cross Section Analysis of a Stealthy S-Shaped Intake Pipe," University of Electronic Science and Technology, Master's Thesis, 1988, 12.

9. Wang Yueqing, "Electromagnetic Properties of a Three-Dimensional Dielectric Radome," University of Electronic Science and Technology, PhD Thesis, 1989, 9.
10. Ruan Yingzheng, Deng Shuhui, "Analysis of EM Scattering From a Two-Dimensional Reflector Antenna Using the Complex-Ray Method," DIANZI XUEBAO [ACTA ELECTRONICA SINICA], Vol 19, No 3, pp 78-83, 1991.
11. He Ling, Ruan Yingzheng, "Scattering Characteristics of the Nose Section of a Cruise Missile," University of Electronic Science and Technology, Second Department, Technical Report, 1989, 5.
12. Tian Jun, "Electromagnetic Scattering of Wing-Fuselage Sections and Sharp Reflectors," University of Electronic Science and Technology, Master's Thesis, 1990, 1.
13. Du Huiping, "Complex-Ray Analysis of the RCS of Coated Metal Plates," University of Electronic Science and Technology, Graduate Student Research Papers, 1990, pp 84-91.

Status of, Prospects for Aerospace Applications of Composite Materials

92FE0145A Beijing ZHONGGUO HANGTIAN [AEROSPACE CHINA] in Chinese No 8, Aug 91
pp 31-35

[Article by Wang Manxia [3769 2581 7209] of the Beijing Materials Processing Institute: "Current Status of, Future Prospects for Aerospace Applications of Composite Materials"]

[Text] Abstract

Composite materials have been used extensively in the aerospace industry. In this paper, the current status of composite-material research in China and the prospects for future development are discussed. Also, the repair technology, testing techniques at high and low temperatures, performance characterization and quality control as well as applied and basic research of composite materials are described.

[Introduction]

Composite materials have many unique properties that are of special importance to the aerospace industry. Experience has shown that high-grade composite materials play a decisive role in reducing the weight, increasing the payload and improving the tactical performance of aerospace vehicles. In order to reduce the size and weight and to achieve higher performance, next-generation space vehicles will increasingly rely on the use of composite materials. Numerous papers can be found in the literature describing the status of aerospace application of composite materials in foreign countries; this article will primarily focus on the current status and future prospects of aerospace applications of composite materials in this country. It is hoped that this discussion will stimulate the development of composite materials for China's aerospace industry.

I. A Review of Aerospace Applications of Composite Materials

Application of high-grade composite materials in the aerospace industry can be divided into the following four areas:

1. Composite materials are used to solve the heat-shield problem for reentry vehicles. Significant progress has been made in the study of heat-resistant

composite materials and many generations of such materials have evolved. For example, heat-resistant materials for the nose cones of reentry vehicles have evolved through four generations: fiberglass composite materials, silicon-oxide fiber materials, ceramic-base composite materials, and tri-directional carbon/carbon composite materials; current research has entered the stage of developing fifth-generation heat-resistant composite materials.

2. Structural composite materials have found increasing applications on space vehicles. Specifically, they are being developed for large structural components and load-bearing components; they have also made contributions in reducing the weight of space vehicles. For example, the front and rear columns of the LM-2E rocket fairings are honeycomb structures made of apore, durable aluminum whose dimensions are $\Phi 4.2\text{ m} \times 1.5\text{ m}$ and $\Phi 4.2\text{ m} \times 3.0\text{ m}$. The satellite interface support structure is made of carbon/epoxy composite material whose dimensions are $\Phi 1664\text{ mm}$ at the top, $\Phi 2042\text{ mm}$ at the bottom and 300 mm in height; it is 40 percent lighter than an equivalent structure made of aluminum alloys. Table 1 shows the various composite-material structural components used on space vehicles.

3. Significant progress has been made in functional composite materials such as wave-absorbing stealth materials, nuclear-hardened materials and anti-particle-cloud materials. Progress has also been made in the development of dual-function and multi-function composite materials such as structural/heat-resistant materials, structural/stealth materials, heat-resistant/nuclear-hardened materials, and structural/heat-resistant/stealth materials. These materials will be used on next-generation space vehicles.

4. A great deal of research and development work has been done in the areas of ceramic-base, metal-base, carbon-base and resin-base composite materials. These materials provide a foundation for high-tech development in the aerospace industry.

II. Repair Technology for Composite-Material Components

The correction of defects and repair of damages in composite-material components is an important consideration in aerospace applications of composite materials. As composite materials are increasingly used on space vehicles, defects or damages may occur during the manufacturing, storage, shipping and operation processes or due to collisions. In order to ensure the quality and reliability of these components and to reduce cost and minimize losses, efforts must be made to develop the technology for correcting the defects and repairing the damages of these composite-material components.

For example, on the fairing of a particular space vehicle, X-ray and ultrasonic inspections showed that the joints of the honeycomb structure had separated and the adhesives holding the two plates together had come loose; also, there was evidence of collision damages caused by an accident. Based on the requirement established by the design department, we have developed different repair materials such as G7A-5 and G7A-9 and the corresponding repair techniques. The G7A-5 material can be injected with a pressure gun, and will solidify under normal temperature and pressure conditions. The

mechanical properties of the solidified repair material can satisfy the design requirements; its density is approximately 40 percent lower than that of epoxy-resin materials, and the contraction rate at the solidification curve is only one-half to one-third that of epoxy-resin.

Table 1. Composite-Material Structural Components Used on Space Vehicles

Sequence number	Name of component	Description	Comment
1	Satellite interface support structure	Cone-shaped structure, $\phi 1664$ mm at the top, $\phi 204$ mm at the bottom, 300 mm in height, thickness of cover skin 1.8 mm (Fig. 1)	Weight reduced by 40 percent compared to equivalent aluminum-alloy support structure
2	Forward cone of fairing	Fiberglass honeycomb structure (Fig. 2)	Used on LM-2E and LM-3
3	Fairing column	Aporate durable aluminum honeycomb structure $\phi 4.2$ m \times 1.5 m and $\phi 4.2$ m \times 3 m	Used on LM-2E
		Porous aluminum honeycomb structure	Used on LM-3
4	Reverse cone of fairing	Aporate durable aluminum honeycomb structure $\phi 3.38$ m \times $\phi 4.2$ m \times 1.34 m	Used on LM-2E
5	Support tube of despun antenna	Replacing aluminum-alloy support tube	Weight reduced by more than 50 percent compared to aluminum-alloy support tube
6	External reinforced shell	Outer diameter 450 mm, height 850 mm, weight 6.6 kg, axial compression test load ~600 kN	Weight reduced by 30 percent by replacing aluminum-alloy shell
7	Internal reinforced shell	Outer diameter 450 mm, height 850 mm, weight 5.5 kg, axial compression test load ~650 kN	Weight reduced by 30 percent by replacing aluminum-alloy shell
8	Horizontal beam	Exterior dimensions 946 mm \times 580 mm, composite beam made of variable-cross-section and variable-thickness "I" beams, "T" beams and "T" beams	Weight reduced by 50 percent compared to nickel-aluminum beams

[Continued on following page]

Sequence number	Name of component	Description	Comment
9	Four-rib reinforced plate	500 mm long, 426 mm wide, skin thickness 1.31 mm, 0.938 kg in weight, average axial compression failure load 109 kN	Weight reduced by 30 percent compared to aluminum-alloy reinforced plate
10	Horn antenna	Good thermal stability, low signal loss	Used on experimental geosynchronous communications satellite
11	Reinforced conic shell	Made of triangular lattice reinforcements (consisting of bi-directional sloped ribs and circular ribs), cover skins, and upper and lower frames; rigid and stable structure with high volume efficiency	Used on the nose cone and fuselage section of space vehicles

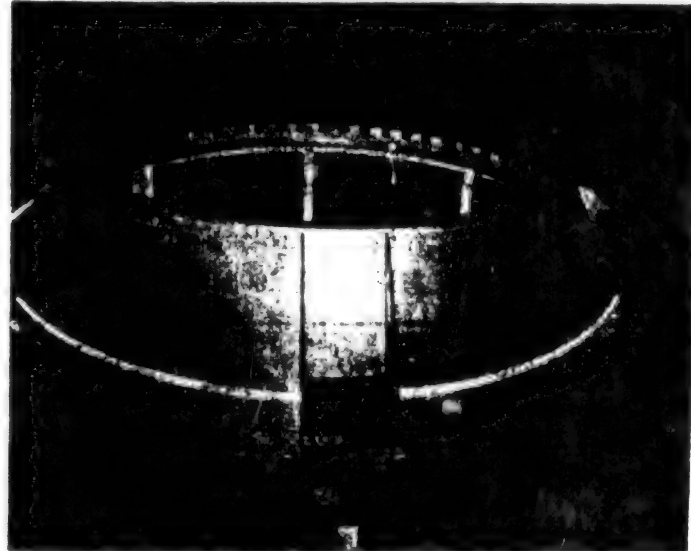


Figure 1. LM-2E Satellite Interface Support Structure



Figure 2. Fiberglass Honeycomb Structure Used on the Forward Fairing Cone of the LM-2E Launch Vehicle

In order to test the performance of the repaired component, a special side-pressure simulation test was conducted. The simulation test object was 250 mm x 250 mm x 4 mm in size and had an artificial defect. After the object was repaired using the G7A-9 material, it was load-tested with its two load-bearing ends reinforced with fiberglass. According to design requirements, the simulated object should fail under a load of 19.61-29.42 kN; however, the test results showed that it did not fail until the load was increased to 54.3 kN. Furthermore, the failure occurred in the vicinity of the fiberglass reinforcements; there was no evidence of damage at or near the repaired location.

In another example, inspection of a honeycomb sandwich structure showed seven defects of various sizes where joints of the honeycomb structure were separated; the maximum length of a defect was 350 mm, the maximum width was 40 mm, and the average defect was 100 mm x 20 mm x 40 mm in size. After the structure was repaired using G7A-5 material, a static load test was conducted to determine the quality and reliability of the repaired structure. The test results showed that the structure can withstand a load of 1.569 kN without damage, which fully satisfies the design and operational requirements. Experience has shown that the repair technology of composite materials is a very important technology for bringing economic and social benefits to the aerospace industry.

III. Testing Techniques for Composite Materials at High and Low Temperatures

The development of aerospace technology requires the ability to determine material properties under special environmental conditions; thus, testing and analyzing the properties of composite materials at high and low temperatures is an important consideration in this regard. As a reentry vehicle enters the atmosphere, its velocity may exceed Mach 20, its temperature can reach several thousand degrees, its pressure can exceed 100 atmospheres (approximately 10 MPa), the heat flux can reach several hundred thousand kJ/m²s, and the overload can reach 100 g. High-grade composite materials provide a key to the survivability of missiles under such severe conditions; however, a prerequisite for studying composite materials is to first solve the problem of high-temperature material testing. For example, for a high-grade carbon/carbon composite material, we must be able to test and analyze its properties at a temperature above 2000°C. As another example, materials selection for the third-stage hydrogen-oxygen engine used on the launch vehicle for communications satellites depends solely on its properties at the temperature of liquid-hydrogen and liquid-oxygen; thus, we must also be able to solve the problem of testing composite materials at super-low temperatures.

After conducting an extensive systematic study, we have successfully solved the problem of testing composite materials at both high and low temperatures; we have also developed the necessary test equipment and established test standards. The required high-temperature test properties of aerospace composite materials include mechanical properties, heat-conduction coefficient, average linear expansion coefficient, specific heat and elastic constant. The test methods used include: electric heating and non-contact strain measurement techniques (for testing mechanical properties in the temperature range of room temperature to 2400°C); pulse laser techniques (for measuring heat-conduction coefficient in the temperature range from room temperature to 2500°C); quartz differential technique and laser scan technique (for measuring average linear expansion coefficient in the temperature range from room temperature to 900°C and from 1000°C to 2500°C respectively); insulated copper calorimeter technique (for measuring specific heat in the temperature range from room temperature to 2900°C) and tungsten-chain resonance technique (for measuring elastic constant in the temperature range from room temperature to 2900°C). By using these testing techniques, we have determined a complete set of high-temperature characteristics of high-grade carbon/carbon composite materials which include strength, modulus, fracture strain, expansion coefficient, heat-conduction coefficient, specific heat and heat radiation coefficient. We have provided this data to the design department for performing thermal analysis and design.

The required low-temperature test properties of aerospace composite materials include mechanical properties, heat-conduction coefficient, average linear expansion coefficient, specific heat and elastic constant. The test methods include: multi-sample immersion technique (for testing mechanical properties in the temperature range of 20°K-300°K); pulse laser technique and longitudinal steady-state heat-flux technique (for measuring heat-conduction coefficient); quartz differential technique (for measuring average linear expansion coefficient); vacuum heat-insulated calorimeter technique (for

measuring specific heat) and dynamic technique (for measuring elastic constant).

IV. Performance Characterization and Quality Control

The performance characterization and quality control of composite materials and raw materials have always been a key issue in promoting the application of composite materials in the aerospace industry. A central question in composite-material research is how to maintain the high quality of space-vehicle components, i.e., how to ensure performance repeatability, quality stability, and operational reliability.

Since the 1970's, significant efforts have been devoted to the issue of performance characterization and quality control of resin-base composite materials. The NASA Langley Research Center initiated work in quality control of epoxy-resin composite materials using graphite fiber reinforcements. Its goal was to develop effective techniques for performance characterization, testing and analysis, and quality control to ensure the "repeatability," "stability" and "reliability" of composite materials. Significant progress has also been made by the U.S. Air Force Materials Laboratory, the Naval Ground Weapons Center, the Naval Research Laboratory, the Army Materials and Mechanics Research Center, the Lockheed Co., the McDonnell-Douglas Co., the (Na-mu-ke) Materials Co. and the Spar Co.

We have conducted systematic studies of the characterization analysis of more than 60 base resins of different brands and different types used in aerospace composite materials. We have used the most advanced testing and analysis techniques which include high-efficiency liquid-phase chromatography technique, gel chromatography technique, Fourier-transform infrared-spectrum technique, differential scan-calorimeter analysis technique, thermal analysis technique, and nuclear-magnetic-resonance (NMR) spectrum technique. We have also studied the relationships between the structure, constituents, and performance of base resins. The results of these studies show that the six commonly used performance indices, i.e., epoxy value, epoxy equivalence, viscosity, contents of volatile matter, organic chlorine and inorganic chlorine do not reflect or control the quality of base resin, and therefore cannot ensure the repeatability, stability and reliability of high-grade aerospace composite materials. We must identify the key parameters for quality control and determine the allowable range of fluctuations of the parameter values; we must control the characteristic peak values by using high-efficiency liquid-phase chromatography and infrared spectrum techniques and express them in "fingerprint" form. On this basis, we have established five ground-rules for characterizing epoxy resins, which are:

1. The DSC measurement and test method for epoxy-resin solidification;
2. The epoxy-resin thermal analysis method;
3. The epoxy-resin infrared characteristics measurement and test method;
4. The high-efficiency liquid-phase chromatography analysis method;
5. The H' NMR analysis method.

In the area of quality control, we have established a quality assurance system based on the following five techniques:

1. The X-ray flaw detection technique, which can detect flaws in different types of composite-material components;
2. The ultrasonic flaw detection technique, which can detect various defects in composite materials such as adhesive detachment and layer separation; it can also measure the contents of air cavity and the total volume of fiber in the material;
3. The acoustic emission technique, which can simulate the dynamic characteristics and predict the state of structural components under load;
4. The laser holography technique, which is used for quality inspection and control of special structures;
5. The C scan technique, which can determine the size and spatial position of the defects.

These non-destructive techniques are considered to be the most advanced in this country and in some aspects are comparable to the state-of-the-art techniques used by advanced countries. They play a very important role in ensuring the quality of composite-material components used in the aerospace industry.

V. Applied/Basic Research of Aerospace Composite Materials

The applied/basic research of composite materials plays an important role in promoting the application of composite materials in the aerospace industry. In support of this effort, we have initiated research and development work in the following areas:

1. Failure analysis of aerospace composite-material components;
2. Ablation and denudation analysis of ablation composite materials;
3. Relationship between the occurrence of defects and damages and the mechanical properties of composite materials;
4. Relationship between the microscopic structure and the performance of composite materials;
5. Research in fracture and interface of composite materials;
6. Methods of estimating the values and design ranges of the mechanical properties of composite materials;
7. Relationship between the constituents, structure and performance of the base resin of composite materials;

8. Performance testing and analysis of composite materials under simulated space environment.

The results of applied/basic research provide important information for understanding physical mechanisms, improving quality, resolving uncertainties and extending the range of applications of composite materials. For example, on a particular component made of tri-directional carbon/carbon composite material, an ablation groove appeared on the surface. It was determined from X-ray inspection that this groove was a fan-shaped crack 50 mm deep and 40 mm long; however, results of failure analysis eliminated the possibility that the crack was caused by thermal stress during the ablation process. The analysis provided conclusive evidence that the crack was not caused by a design flaw but rather was a random occurrence because it did not expand during fabrication. In another example, it was found in studying the relationship between the microscopic structure and performance of carbon/carbon composite material that the "spherical cluster" carbon structure has a significant effect on its performance such as ablation, denudation and fracture. Therefore, in order to obtain high-performance carbon/carbon composite material, it is necessary to control the fabrication process so that "spherical cluster" carbon structures do not appear. In a third example, when applying the dynamic process of the acoustic emission technique, it was found that failure usually does not occur at the location where a static defect is present; the weakest point often is the interface. Therefore, in assessing the performance and quality of aerospace composite materials, it is not sufficient to rely on evidence of static defects alone; one must determine the source and the variation of damage under actual operating conditions, and identify the relationship between the occurrence of damage and the interface structure and performance of the composite material. Only such an integrated assessment approach can provide a scientific evaluation of whether or not the product is acceptable.

VI. Future Prospects

With the development of new space vehicles, future applications of high-grade composite materials in the aerospace industry are expected to grow steadily. The future prospects of aerospace composite materials can be summarized in the following areas:

1. The development of aerospace technology requires future products to be smaller, lighter and to have higher performance. Therefore, the proportion of composite materials used on strategic missiles, tactical missiles, launch vehicles, solid-propellant rocket engines and satellites will continue to increase.
2. In view of the economic conditions and technical capabilities of this country, the application of composite materials in the aerospace industry must be driven strictly by needs and must have limited objectives.
3. To meet the needs of future space-vehicle development, efforts should be devoted to the research and development of high-performance fiber composite materials, heat-resistant composite materials, high-grade carbon/carbon composite materials and multi-function composite materials.

4. Additional efforts should also be devoted to the study of performance characterization, quality control and performance testing and analysis of composite materials under special conditions.
5. The manufacturing and fabrication of aerospace composite-material components should be mechanized and computerized by applying CAD/CAM (computer-aided design/computer-aided manufacturing) techniques.
6. Efforts in applied/basic research of aerospace composite materials should be expanded.
7. Funds should be allocated to complete the construction of the aerospace composite-material research center and to procure additional research equipment.

Introduction to FY-1 Meteorological Satellite Data Receiving/Processing System

92FE0060A Beijing ZHONGGUO KONGJIAN KEXUE JISHU [CHINESE SPACE SCIENCE AND TECHNOLOGY] in Chinese Vol 11 No 2, Apr 91 pp 39-45

[Article by Fan Tianxi [5400 1131 6932] of the Satellite Meteorological Center, SMA: "Introduction to FY-1 Meteorological Satellite Data Receiving and Processing System"; MS received 12 Nov 90]

[Text] Abstract

A brief description of the FY-1 meteorological satellite data receiving/processing system, which consists of three ground stations located in Beijing, Guangzhou and Urumqi, and a data processing center located inside the Satellite Meteorological Center of the State Meteorological Administration, is given. The system also has the capability of receiving and processing data from the U.S. NOAA satellites and Japan's GMS weather satellite.

I. Introduction

On 7 September 1988, China launched its first polar-orbit meteorological satellite, the FY-1A; on 3 September 1990, the second meteorological satellite, the FY-1B, was launched. In 1987, a meteorological satellite data receiving/processing facility was constructed primarily to receive and process the data from the FY-1 satellites. Having demonstrated its data receiving and processing capabilities for the FY-1A satellite, the system is now receiving and processing data from the FY-1B satellite and is also expanding its services for other applications.

The launch of the FY-1 meteorological satellite and the construction of its ground system was an important milestone for the advancement of China's meteorological science. The system plays an important role in many different areas including weather forecasting, monitoring of natural disasters, monitoring of the ecology of the environment, meteorological research, aviation, navigation and military weather service. It can potentially provide large social and economic benefits.

In order to fully exploit the utility of meteorological satellites, it is necessary to construct ground data receiving/processing facilities designed to extract useful information from the raw data collected by the satellite and transmit it to the user in some appropriate output format. The data collected by meteorological satellites are indirectly measured data which must be processed to derive the various physical parameters of the weather or the environment, and must be transformed into some graphical form for presentation to the user. This data-processing task requires not only the development of appropriate physical models and processing techniques but also efficient software and hardware systems. Therefore, it is a problem involving physics and mathematics as well as systems engineering.

II. System Description

The FY-1 Meteorological Satellite Data Receiving/Processing System has three ground stations (Beijing, Guangzhou and Urumqi) and a data processing center (Satellite Meteorological Center, Beijing). The system can also receive and process data from the U.S. polar-orbit NOAA satellites and wide-band data from Japan's GMS satellite. A block diagram of the system is shown in Figure 1.

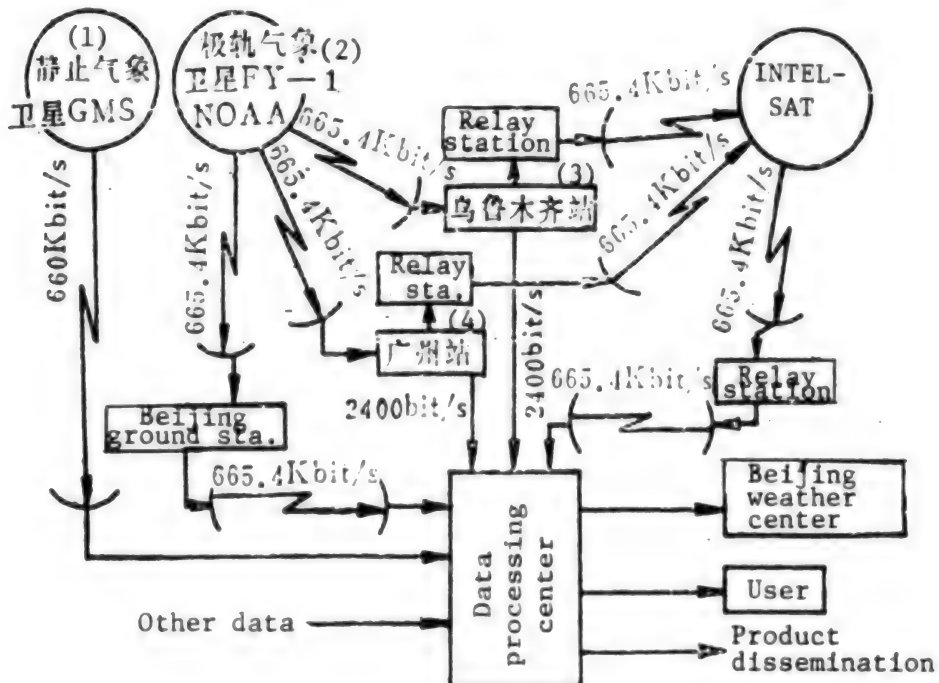


Figure 1. Block Diagram of the FY-1 Meteorological Satellite Data Receiving and Processing System

Key:

1. Geostationary meteorological satellite GMS
2. Polar-orbit meteorological satellites FY-1, NOAA
3. Urumqi ground station
4. Guangzhou ground station

All three ground stations can receive data from the FY-1 satellite and the NOAA satellites. Data received by the Guangzhou station and Urumqi station are transmitted to the data processing center via INTELSAT; data received by the Beijing station are transmitted directly to the data processing center via microwave links; the wide-band data from the GMS satellite are received directly by the data processing center.

To perform the data processing task, the center collects meteorological data from all three ground stations as well as orbit parameters of the FY-1 satellite from the State Telemetry, Tracking and Control (TT&C) Center; it also receives conventional meteorological data from the State Weather Center and orbit information of the NOAA satellites. Within a specified time period, the center generates various graphical products and quantitative products, as well as products for special applications. These products are sent to the State Weather Center through different channels; some of the products are disseminated to other users and the whole nation via television broadcast.

III. Main Features of the Meteorological Satellite Data Processing System

The FY-1 meteorological satellite delivers both real-time data and time-delayed data stored on the satellite. A limited geographic region of this country is covered by foreign satellites because only real-time data can be received from these satellites. A ground station can receive data from three consecutive orbit passes, each pass lasting a maximum duration of 15 minutes. The real-time data received by the three ground stations in Beijing, Guangzhou and Urumqi cover a geographic region of approximately 0° - 65° N and 60° - 150° E. Relative to any location on earth, the FY-1 satellite passes over twice a day and the NOAA satellites (with a two-satellite constellation) have four observation opportunities per day; the Japanese GMS satellite can collect enough data to generate one disk map per hour. The main features of the meteorological satellite data receiving/processing system are as follows:

- 1) High transmission speed and high information content. The HRPT [high-resolution picture transmission] data transmission speed of the FY-1 satellite and the NOAA satellite is 0.6654 Mbits/s; the information content of the raw data from these satellites is approximately 2,000 Mbits; the information content of each GMS disk-map observation is approximately 120 Mbits, which corresponds to more than 5,000 Mbits per day.
- 2) Versatility of data input/output format. To satisfy the needs of data processing and analysis for different applications, the system receives not only satellite data, but also data in a variety of input formats including conventional meteorological data, radar data and data collected by aircraft, field data based on objective analysis and forecast, historical data and other data. The output data formats include interactive graphic terminals, data transmission and simulated signal transmissions, magnetic video recordings, facsimile pictures, contour maps, digital printed output, color and black-and-white hard copies, magnetic tapes and floppy disks, and microfilms.

- 3) Variety of products and processing complexity. To generate various meteorological and environmental parameters, the system must perform not only image processing and graphic processing, but also quantitative processing. In addition, the derivation of higher-order parameters requires other processing operations such as statistical calculations and comparison, matching, normalizing, and accumulation between the different parameters and between satellite data and non-satellite data.
- 4) Data storage and data files. Each magnetic disk should have the capacity of storing one to three days of satellite data that can be retrieved at any time. The satellite raw data and processed results are stored as data files on magnetic tapes; approximately 10,000 tapes are created each year.
- 5) Speed and automation of data processing. Because of the timeliness requirement, the large volume and variety of satellite data and the processing complexity, high-speed and automated processing is essential.
- 6) Reliability. Since meteorological satellite data must be received and processed continuously on a 24-hour basis, a highly reliable real-time operational system is required.

The features described above show that the receiving/processing system is different from an ordinary scientific computational system because it must have a highly robust data input/output capability. For example, the daily volume of information of conventional weather data is less than 15 Mbits, which is 2-3 orders of magnitude lower than the volume of satellite data; digital weather forecasting involves large amounts of computations, but the input/output data volume is relatively moderate. In addition, the system also differs from other remote-sensing data processing systems because of the stringent requirements of timeliness, reliability and product versatility. These features lead to a very complex system design with a highly automated processing capability.

As the measurement techniques, processing methods and applications of meteorological satellites continue to evolve and grow at a rapid pace, the data processing system, particularly the application software, must also be undergoing continuous enhancement and improvement. Therefore, the system design must be operationally stable on the one hand, and be sufficiently flexible to incorporate constant improvements on the other.

IV. System Configuration

To carry out its primary mission of receiving and re-transmitting meteorological satellite data, the system is equipped with antennas, receivers, timing subsystems and communication equipment. To carry out the tasks of data editing, storage, monitoring and antenna tracking, it is equipped with a small computer system which consists of two IBM S/1 computers, two 200-Mbit disk drives (4967), one tape drive, two-three PC/AT microcomputers as well as image processing and display equipment.

The data processing center consists of the receiving system, the communications system, the timing system and the central computer system. The central computer system is divided into two parts: the main computer and the input/output subsystem, as shown in Figure 2.

The input/output subsystem is equipped with four IBM S/1 control computers, each with a 1-Mbit main storage; it is also equipped with four 200-Mbit disk drives (4967), two tape drives (4968), four video monitors (PC/AT) and other equipment. Of the four S/1 computers, two are used for HRPT data input, one is used for GMS data input, and one is used for data output.

The main computer system is equipped with three IBM 4381-PO3 computers each with a 16-Mbit memory; the computers are connected to one another by 3088 channel connectors. The system is also equipped with 32 disk drives (3375), each with a 819.7-Mbit storage capacity; five high-density (38,000 bits/in) tape drives (3480); three 6,250-bits/in tape drives (3420) and three 1,600-bits/in tape drives (3422); four row printers (4245); two floppy disk drives (3540); three interactive image processing systems, including two 7350 systems and one system provided by the University of Wisconsin; two graphic data processing units (5080); two X-Y plotters (7375); 36 user terminals (3178) and 10 printers. In addition, there are two switching management systems (3814), two communications controllers (3725), three disk controllers (3880), three tape controllers (3480 and 3803), four terminal controllers (3274) and several PC/AT microcomputers. The peripheral equipment, particularly the disk drives, can generally be shared by the three main computers. The main computer system is linked to the computer system of the State Meteorological Center via the LCN high-speed network.

The software of the central computer system can be divided into six different parts, as shown in Figure 3.

- 1) The S/1 and 4381 system software. This software includes the operating system, the language programs, the communications software, the image processing and graphics software, and other applications software. They are the basic software that support computer operations, administrative operations and user interface. The operating system for the S/1 computer is EDX (Event Driven Executive Operating System), and the operating system for the 4381 computer is MVS (Multiple Virtual Storage Operating System).
- 2) The S/1 data input/output software. It is designed to relay the data from the satellite to the 4381 computer, and to transmit the video cloud maps and television pictures generated by the 4381 computer.
- 3) The 4381 communications software. It is designed to perform the tasks of data transmission between the 4381 communications system and the S/1 computer, and data input/output through the 3725 communications controller and the LCN network.
- 4) The applications software. It resides on the main computer and performs the functions of pre-processing and processing of satellite data, processing of man-machine interactive images and graphics, data searching and filing.

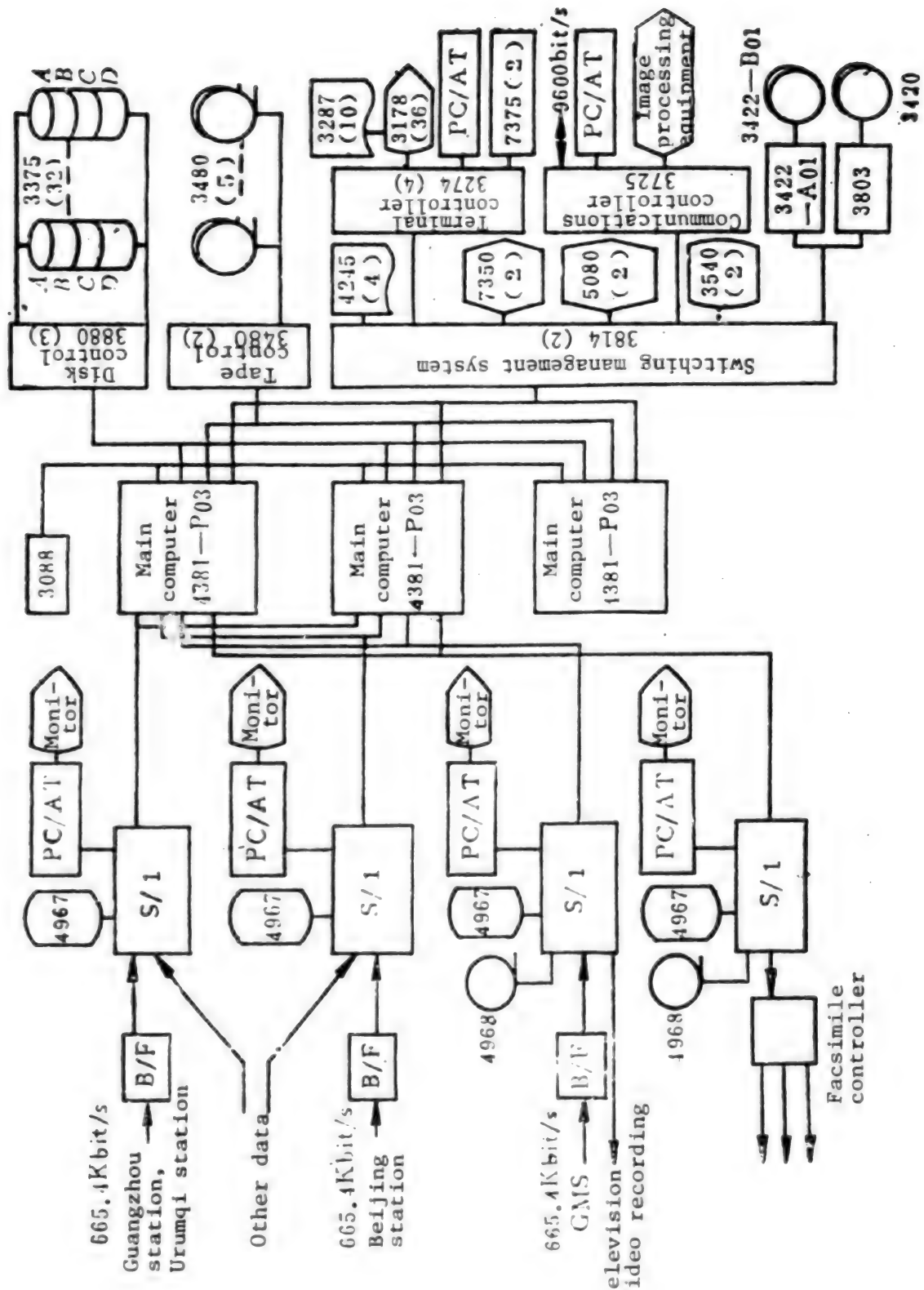


Figure 2. Configuration of the Data Processing Central Computer System

5) The process scheduling and management software. It controls the automatic starting of most processes, provides information on the operating status of each process, and also has some capability of fault processing.

6) The command scheduling and product distribution/service software. It is designed to manage the transmission of information and delivery of products between the input/output system of the processing center and various organizations outside the center; it also performs the monitoring and management functions of the operations of the three ground stations and the processing center.

Of the six software subsystems, the system software of the S/1 and 4381 computers are provided by IBM; the others are all dedicated software developed by the Satellite Meteorological Center.

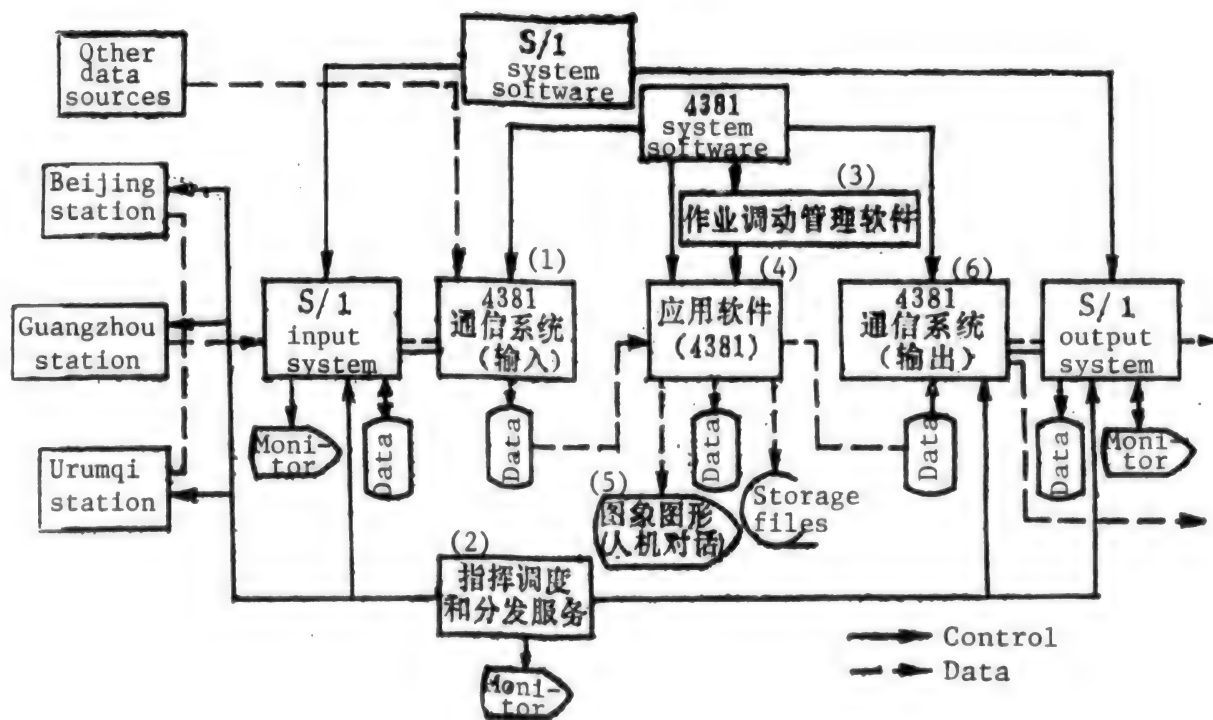


Figure 3. Block Diagram of the Software System

Key:

1. 4381 communications system (input)
2. Instruction scheduling and distribution services
3. Transaction swapping management software
4. Application software (4381)
5. Graphics and image processing (man-machine interaction)
6. 4381 communications system (output)

V. Data Processing Flow

The processing of meteorological satellite data can be divided into four steps: (1) data input; (2) pre-processing; (3) data processing; (4) output of processed results and storage of data files.

After the raw data received by the ground stations are transmitted to the processing center, they must first pass through the bit synchronizer, the frame synchronizer and the buffer storage unit before they reach the S/1 computer; they are then sent to the 4381 main computer via the interface (4993), and stored on disks in the form of formatted files; these files are called the "1A" data set. Conventional weather data and other types of data are also compiled into a file to be stored on disks.

The satellite raw data must first be pre-processed, which includes quality inspection, processing of calibration coefficients, geo-positioning, classification and editing, reformatting, etc., to form an intermediate data set; this data set is referred to as the "1A.5" or the "1B" data set. For example, in pre-processing the scanning radiometer data from the FY-1 satellite, additional data such as quality index, calibration coefficients, solar zenith angle and geographic latitude and longitude are appended to each scanning line to provide the reference information for subsequent data processing.

Different types of data processing are performed to meet the requirements of different applications; generally they can be divided into two categories: image processing and quantitative processing. In image processing, data from the FY-1 satellite and the NOAA satellites are used to create single-orbit cloud maps and perspective or Mercator projection maps; data from the GMS satellite can be used to create disk maps, regional maps and projection maps. The cloud maps and ground-feature maps can be enhanced and synthesized using multi-spectral techniques. In quantitative processing, various meteorological parameters such as ocean surface temperature, cloud parameters, long-wavelength radiation, ground vegetation index, atmospheric temperature and humidity contours can be processed and the results presented in graphic form.

The processed results are generally stored as disk files which can be produced in various output formats. Image and graphic products can be displayed through interactive graphics terminals, facsimiles, television broadcasts and other means of transmission. Digital products can be displayed through digital transmissions (in the form of coded or digital files), tapes, floppy disks or on digital printers.

Data storage is also an important segment of the data processing system. Because of the large volume of meteorological satellite data, only a selected portion of the data are stored in the form of pictures and printed files; most of the data are stored on magnetic tapes and microfilms.

VI. Main Products and Applications

The FY-1 meteorological satellite data receiving/processing system is currently receiving data from four meteorological satellites: China's FY-1B satellite, the U.S. NOAA-10 and NOAA-11 satellites, and Japan's GMS-4 satellite. It generates a variety of products for a wide range of different applications.

In the area of short-term weather forecasting of such typhoons and rain storms that involve strong convective currents, the GMS plays a unique role because it can monitor rapid changes in the weather system through continuous observations. Unfortunately, Japan's GMS has limited coverage of China's landmass because it is situated at 140°E; therefore, its geographic resolution is significantly degraded, particularly over the western part of this country. The polar-orbit meteorological satellite is in a low-altitude orbit; it provides higher spatial resolution, a larger number of radiometer channels and higher measurement accuracy. In addition to playing an important role in routine weather forecasting, it also has potential applications in the study of long-term weather forecast and climatology. The polar-orbit meteorological satellites can effectively monitor the weather systems and their movement in a region extending from western China to the Soviet Union; in particular, they can be used to study the behavior and the effect of weather systems over the Qinghai-Tibet highland. Meteorological satellite data also plays an important role in aviation, navigation and military weather service.

Because of the wide area coverage, timeliness and objectivity of meteorological satellite data, its utility has extended far beyond the traditional area of weather analysis; today it is used to monitor the earth's environment, natural disasters, and ecological development. In this country, there has also been a significant growth in the application of satellite data in recent years, particularly in the area of monitoring forest fires, floods, ground vegetation, ocean surface temperature, sediment deposits in rivers, ocean ice formation, snow accumulation, urban hot spots, and wheat production; in addition, other areas of application such as developing earthquake indicators are also being explored.

These applications impose special requirements on the products of meteorological satellites; however, certain products are generic in nature and can be used in many different applications. Table 1 shows a selected number of important products of China's FY-1 satellite; products generated by data from the Delayed Picture Transmission (DPT) system are not included.

VII. Concluding Remarks

The ground subsystem of the FY-1 meteorological satellite system is one of the five major subsystems, which include the satellite, the launch vehicle, the launch subsystem, the telemetry and control subsystem and the ground application subsystem. Currently, it is primarily used to process data from polar-orbit meteorological satellites. Since the system was built prior to the launch of the FY-1 satellite, its system check-out and operational tests

Table 1. Important Products of the FY-1 Meteorological Satellite

Product number	Product name	Range	Resolution (km)	Processing frequency (times/day)	Output format
1	Polar-equatorial projection mosaic map	0°-85°N, 60°-150°E	3.7 (equatorial region), 7.4 (polar region)	2 (infrared), 1 (visible)	121 pictures (negative), graphic display
2	Multiple-channel synthesized map (1, 2, 5)	Chinese land-mass	3.7 (equatorial region), 7.4 (polar region)	1	Graphic display
3	Multiple-time brightness synthesized map	25°-65°N, 60°-125°E	3.7 (equatorial region), 7.4 (polar region)	1	Graphic display
4	Locally enhanced cloud map	Local	1-4	Based on need	Graphic display
5	Single-orbit extended cloud map	Single-orbit detection region	1-4	2	Graphic display, 121 pictures (typical)
6	Ocean temperature	0°-50°N, 105°-155°E 0°-50°N, 105°-155°E	0.5° × 0.5° (latitude, longitude) 0.5° × 0.5° or 2.5° × 2.5° (latitude, longitude)	1	Telecode, printed symbols
7	Emitted long-wavelength radiation	0°-50°N, 75°-150°E	0.5° × 0.5° (latitude, longitude)	Daily average, seasonal average, 10-day average, monthly average	Daily avg., seasonal avg., 10-day avg., & monthly avg.
8	Cloud parameters (temperature on top cloud and volume of cloud)	15°-55°N, 70°-155°E	5 or 50	2	Telecode, printed symbols
9	Map of ground vegetation index	China and neighboring countries (Global) (Regional) arbitrary	6	1 per 10 days	Graphic display
10	Map of oceanic ice distribution	36°-41°N, 117.5°-122.5°E	0.02° × 0.02° (latitude, longitude)	1	Graphic display, printed symbols

were performed by receiving and processing data from foreign meteorological satellites. As a consequence, when FY-1 was launched into orbit, the system was ready to receive and process its data immediately; furthermore, it can also combine FY-1's data with those from foreign satellites to enhance the application and utility of the system.

The FY-1 is an experimental satellite which not only provides operational value in many areas of application, but also serves as a prototype for future development of China's meteorological satellite technology. In the 1990's, China will launch a geostationary meteorological satellite, the FY-2; also, it will incorporate many improvements on and enhancements to the polar-orbit satellite FY-1. To accommodate the new developments in future satellites, improvements and enhancements must be incorporated into the ground application subsystem. Currently, the system is being expanded to receive and process data from the FY-2 satellite.

With the successful development of the FY-1 meteorological satellite and the construction of the ground application facilities, the 1990's will be a very important era for rapid growth of China's satellite meteorological services.

Optimal Design for Large-Caliber, Long-Range Artillery Projectiles

92FE0101A Mianyang KONGQIDONGLIXUE XUEBAO in Chinese Vol 9 No 3, Sep 91
pp 344-350

[Article by Tan Junjie [62233 0193 2638] of East China Institute of Technology]

[Text] Abstract

Designing large-caliber and long-range projectiles with maximum range, ample power, flight stability, and launching strength is a significant problem. This paper presents a mathematical model of aerodynamic and exterior ballistic optimum design for large-caliber and long-range projectiles and addresses for the first time the shape optimization problem of base bleed projectiles.

Introduction

In the design of large-caliber, long-range projectiles, it is important to strive for ample power, flight stability, launching strength and maximum range without altering the artillery piece. To this end, the author has studied the aerodynamic and exterior ballistic optimization for large-caliber, long-range projectiles. A general design optimization model was established and the designs of 130 mm and 175 mm projectiles were optimized. The results showed that the range of the optimized projectile was greater than the original design while meeting the requirements on flight stability and launching strength without modifying the artillery piece. This paper has also investigated, for the first time, the shape optimization problem for base bleed projectiles. As a preliminary study, this paper has not considered such factors as concentration and base bleed structures.

I. Review of Mathematical Method^{1,2}

Consider the following constrained optimization problem:

$$\begin{cases} \min f(\mathbf{x}), & (\mathbf{x} \in \mathcal{D}_0) \\ \mathcal{D}_0 := \left\{ \mathbf{x} \mid h_i(\mathbf{x}) = 0, (i = 0, 1, 2, \dots, m) \right. \\ \quad \left. g_i(\mathbf{x}) \geq 0, (i = m+1, \dots, n) \right\} \subset \mathbb{R}^n \end{cases} \quad (1)$$

where the vector x , given by

$$x = (x_1, x_2, \dots, x_n)^T \quad (2)$$

is the optimization variable. The target function $f(x)$ and constraint functions $h_i(x)$ and $g_i(x)$ are real functions in R^n , and the allowed domain is $\mathcal{D}_0 \subset R^n$. The problem in Eq. (1) is known as the minimum value problem for $f(x)$ that satisfies $h_i(x) = 0$ and $g_i(x) \geq 0$. The problem addressed in this paper is the maximum range $F(x)_{\max}$, that is,

$$\begin{cases} \max F(x), & (x \in \mathcal{D}_0) \\ \mathcal{D}_0 = \left\{ x \mid h_i(x) = 0, \quad (i = 0, 1, 2, \dots, m) \right. \\ \quad \left. g_i(x) \geq 0, \quad (i = m+1, \dots, n) \right\} \subset R^n \end{cases} \quad (3)$$

Let $f(x) = -F(x)$, (3) is reduced to (1).

The original constrained problem may be transformed to finding the serial solution of the unconstrained optimization problem. That is, finding the minimum of $f(x)$ under the constraint of

$$\phi^{(k)} - T(x) \geq 0 \quad (4)$$

where $\phi^{(k)}$ is the allowable error for the feasibility of the k th step and $T(x)$ is a measure that point x will violate the constraint condition. In the calculation, $T(x)$ is taken to be

$$T(x) = \left\{ \sum_0^m h_i^2(x) + \sum_{i+1}^n \left[\frac{|g_i(x)| - g_i(x)}{2} \right]^2 \right\}^{\frac{1}{2}} \quad (5)$$

In this paper we solve the unconstrained problem using the variable polyhedron method. The calculation is essentially a search routine for a variable polyhedron and is achieved through four basic operations: reflection, expand, compression, and contraction. It should be mentioned that simple shapes may degenerate to lower dimension; a small perturbation beforehand is helpful for finding the solution.

II. Mathematical Model for General Optimization

1. Target Function $f(x)$

In this work the range of the projectile is chosen as the single target function and calculated as follows:

$$\left\{ \begin{array}{l} \frac{dv}{dt} = - \frac{\rho v^2 S}{2m} C_x - g \sin \theta \\ \frac{d\theta}{dt} = - g \cos \theta / v + \frac{1}{2m} \rho v^2 S C_y^2 a \\ \frac{dy}{dt} = v \sin \theta \\ \frac{dx}{dt} = v \cos \theta \end{array} \right. \quad (6)$$

Equation (6) shows the target correlation functions. In determining the value of the target function $f(x)$, the values of v , θ , and x under the initial condition $t = 0$ are:

$$\left\{ \begin{array}{l} v = v_0 \\ \theta = \theta_0 \\ x = y = 0 \end{array} \right. \quad (7)$$

In the calculation the effects of gravitational acceleration, temperature, and density on the flight height were considered. The resistance functions $C_x(M, a)$ and C_y^2 were determined using the method described in Ref. 4. Once the exterior shape of the projectile was determined, $C_x(M, a)$ and C_y^2 were also determined. Furthermore, for given initial conditions of velocity, weight, and projectile angle, Eq. (6) had a unique solution. Hence, different trajectories were obtained by varying the exterior shape of the projectile, and the optimization was done this way.

2. Selection of the Optimization Variable

Profile parameters of the projectile include the diameter, head length, cylinder length, stern length, stern angle, top diameter, and head shape. These parameters have a direct effect on the aerodynamic characteristics of the projectile. In addition, the shape of the inner chamber, the projectile material, and the specific gravity of the explosive are related to the projectile characteristics, which all have a great effect on the flight behavior of the projectile.

If the only goal is to minimize the resistance, then no matter which method is used, the optimum shape is that of a date pit; there will not be a cylindrical portion. A projectile of this shape cannot be centered in the barrel unless additional centering blocks were installed. Projectiles of this shape also hold less charge and have lower power. In order to overcome this problem and to reconsider the ease of manufacturing, the basic shape of the projectile was taken to be an ovate head, followed by a cylindrical body, and a tail. Optimization was done for this layout. The diameter was determined from tactical considerations, and the diameter of the top was determined by the size of the detonator, these sizes were not to be optimized. The external profile parameters to be optimized are the length of the head l_H , radius of the head R , the length of the cylinder l_C , the length of the tail l_{BT} , and the angle of the tail θ_{BT} .

The volume of the inner chamber of the projectile determines the amount of the explosive charge and the wall thickness. Generally speaking, the greater the inner chamber volume, the greater the explosive charge, the thinner the wall thickness, and the weaker the strength; the converse is also true. In order to consider the strength and the power, a wall thickness parameter ξ is introduced to determine the shape of the inner chamber of the projectile.

The mass m and the initial velocity v_0 of the projectile have a large effect on the range. However, for a given gun and the same barrel pressure, the muzzle kinetic energy E is almost a constant. The following relationship exists:

$$E = \frac{1}{2} m v_0^2 \quad (8)$$

Therefore, when the external profile parameters, internal chamber parameters, and the material of the projectile are determined, m and v_0 are also determined uniquely.

3. Selection of the Constraint Conditions

The optimized projectile should satisfy the following constraint conditions.

(1) Based on the overall layout of the gun and the flight stability of the projectile, the total length of the projectile should be controlled within the following range:

$$l - l_s - l_e - l_{pt} \geq 0 \quad (9)$$

If the length of the projectile is to be a constant, then Eq. (9) will contain an equal sign. When there are no stringent requirements on the length of the projectile, then Eq. (9) may assume the form of an inequality and serve as a loose constraint. In this case, the final value of the length will be determined by satisfying other constraints.

(2) To ensure adequate power, the relative mass of the projectile and the explosive should satisfy a certain requirement. In Table 2-1 of Ref. 5, the relative mass of the killing projectile was given as $C_\Omega = (11-15) \times 10^3$ (kg/m³), and the corresponding relative mass of the explosive was $C_\omega = (1.5-2.2) \times 10^3$ (kg/m³).

(3) The projectile must satisfy the gyroscopic stability conditions:

$$\left\{ \begin{array}{l} S_1 = \frac{\rho}{k_1} + C_\omega \\ \beta = \frac{C_\omega}{2A} \left(\frac{\dot{y}}{v} \right) \\ k_1 = \frac{\rho S}{2A} l m \end{array} \right. \quad (10)$$

where S_t is the gyroscopic stability factor, C_1 is constant greater than unity (usually 1.5 at the muzzle), A and C are respectively the equator angular momentum and the polar angular momentum, S is a reference area, l is the length of the projectile, v is the velocity, and m'_2 the derivative of the pitching moment coefficient.

(4) The projectile must also satisfy the tracking stability condition. Under the influence of gravity, the projectile continuously deflects downward. The so-called tracking stability is the ability for the projectile axis to rotate as the velocity vector rotates. This requires that the dynamic equilibrium angle δ_p cannot be too large. For example, the actual dynamic equilibrium angle of a 203 mm shell is $11^\circ 23'$. The dynamic stability angle is determined by the following method:

$$C \dot{\gamma} \dot{\theta} = \frac{\rho}{2} v^2 S l C_m' \quad (11)$$

where $\dot{\gamma}$ is the angular velocity of the shell, $\dot{\theta}$ is the angular velocity of deflection of the velocity vector of the projectile, and C_m' is the pitching moment coefficient. In the presence of the dynamic equilibrium angle δ_p , C_m' may be expressed as

$$C_m' = C_m \delta_p - \frac{1}{6} C'''_m \delta_p^3 \quad (12)$$

where C_m' and C'''_m are respectively the first- and third-order derivatives of the attack angle. Substituting (12) into (11), and letting

$$Q = \frac{2C \dot{\gamma} \dot{\theta}}{\rho v^2 S l}$$

Equation (11) can then be written as

$$\delta_p^3 - \frac{6C_1}{C''_m} \delta_p - \frac{6Q}{C''_m} = 0 \quad (13)$$

The value of δ_p obtained from the above equation should satisfy the tracking stability condition

$$\delta_p < \delta_s \quad (14)$$

(5) The projectile should satisfy the requirement of dynamic stability. In addition to gyroscopic and tracking stability, the projectile should also satisfy dynamic stability, otherwise the projectile will be unstable in flight. The dynamic stability factor S_d may be expressed as

$$S_d = \frac{2 \left(\frac{d}{l} C_1^2 - \frac{d^2}{R^2} m'_2 \right)}{\frac{d}{R^2} m'''_2 - \frac{d}{l} C'''_m - \frac{d^2}{R^2} m''_2} \quad (15)$$

where m_y' is the derivative of the Magnus moment coefficient, m_{xz}' is the derivative of the polar damping moment coefficient, m_{zz}' is the derivative of the equator damping moment coefficient, and R_A and R_C are respectively the equatorial and polar turning radius. To ensure stable flight, S_d and S_t should satisfy the following relationship:

$$S_d(2 - S_d) \geq \frac{1}{S_t} \quad (16)$$

(6) The projectile must satisfy the requirement of the launching strength. The strength criteria are divided into a body strength criterion and a base strength criterion. Reference 5 gave the following criteria:

$$\begin{cases} \bar{\sigma}_1 \leq k \sigma_{..} & \text{(Body)} \\ \bar{\sigma}_1 \leq \sigma_{..} & \text{(Base)} \end{cases} \quad (17)$$

where k is a fitting coefficient, generally between 1.2 and 1.4, and $\bar{\sigma}$ and $\bar{\sigma}_1$ are computed using the formulas given in Ref. 5.

Based on the analysis above, the constraint zones to be satisfied by the optimization process are:

$$\begin{aligned} & \left\{ \begin{array}{l} h_1(\mathbf{x}) = l - l_s - l_c - l_{BT} = 0 \\ \text{or} \end{array} \right. & & \text{(Fixed length)} \\ & \left\{ \begin{array}{l} g_1(\mathbf{x}) = l - l_s - l_c - l_{BT} \geq 0 \\ g_2(\mathbf{x}) = C_s - C_{s0} \geq 0 \\ g_3(\mathbf{x}) = C_s - C_{s*} \geq 0 \\ g_4(\mathbf{x}) = \delta_s - \delta_s^* \geq 0 \\ g_5(\mathbf{x}) = S_t - S_s \geq 0 \\ g_6(\mathbf{x}) = S_d(2 - S_d) - 1/S_t \geq 0 \\ g_7(\mathbf{x}) = k \sigma_{..} - \sigma_{..} \geq 0 \\ g_8(\mathbf{x}) = \sigma_{..} - \bar{\sigma} \geq 0 \end{array} \right. & & \text{(Variable length)} \end{aligned} \quad (18)$$

The derivation given above is for a general projectile. The situation is basically the same when there is base bleed, except that the effects of the base bleed should be considered in the resistance term C_x in Eq. (6). In the initial design, the base resistance coefficient may be expressed as

$$C_{x0} = C_{x0} + e^{-J} \quad (19)$$

where C_{x0} is the base resistance without base bleed, $I = \dot{m}/\rho_\infty v_\infty A_b$ is the velocity of the incoming flow, ρ_∞ is the density of the incoming flow, A_b is the area of the bottom, J is the resistance reduction coefficient to be determined in a wind tunnel test, and \dot{m} is the mass flow, determined by the following equations:

$$\begin{aligned}
 dp_0 &= \frac{RT_0}{v} [S_1 \rho_1 (a+b p_0^n) - \dot{m}] dt \\
 S_1 &= 2\pi l_1 \left[r \left(\frac{\pi}{m} - \theta_1 \right) + \sqrt{r^2 + r_2^2 - 2rr_2 \cos \beta_1} \right] \\
 v_1 &= v_{01} + \int_0^t (a+b p_0^n) S_1 dt \\
 r &= r_1 + \int_0^t (a+b p_0^n) dt \\
 C &= C_1 + \int_0^t (a+b p_0^n) dt \\
 \dot{m} &= \frac{A_e p_1}{\sqrt{RT_1}} \sqrt{\frac{2k}{k-1} (\chi_1^{\frac{k}{k-1}} - \chi_2^{\frac{k}{k-1}})} \\
 \chi_1 &= p_1 / p_0 \\
 \beta_1 &= \arcsin(c/r) - \arcsin(c/r_1) \\
 \theta_1 &= \arcsin(c/r)
 \end{aligned} \tag{20}$$

where p_0 is the internal pressure of the burning gas, p_e is the environmental pressure, T_0 is the temperature of the burning gas, R is the gas constant, S_1 is the area of the combustion, m is the number of explosive charge lobes, ρ_1 is the density of the charge, $a + b p_0^n$ is the burning speed, A_e is the area of the nozzle, l_1 is the length of the charge, r_1 is the initial bore radius of the charge, r_2 is the external radius of the charge, t is time, r_t is the instantaneous bore radius of the charge, C_1 is one-half of the initial gap between the charge lobes, C_2t is one-half of the instantaneous gap between the charge lobes, and k is the thermal insulation factor of the burning gas.

Once the composition of the base bleed charge is determined, Eq. (20) may be used for the computation of the mass flow and burning time at any instance of time. Equation (19) can then be used for the calculation of base resistance coefficient with base bleed. When the burning is complete, the resistance reduction effect also disappears.

In this paper, a mathematical model is given for the external profile optimization of large-caliber projectiles, including the target function, the optimization variable, and the correlation and constraint conditions for the target function. The aerodynamic trajectory optimization results may be obtained by invoking conventional nonlinear mathematical methods.

III. Typical Results and Analysis

Using programs based on the method described above, calculations were made for 175 mm and 130 mm projectiles. Optimization was also made for 130 mm projectiles with base bleed with satisfactory results.

The 175 mm projectile of the M107 cannon is one of the advanced projectiles in the world. Its initial velocity is 914 m/s, the mass is 67 kg, the range is 32,760 m for a 50° angle. The optimization design results for the 175 mm projectile are listed in Table 1.

Table 1

	$\frac{l}{d}$	$\frac{l_n}{d}$	$\frac{R}{d}$	$\frac{l_{BT}}{d}$	β (degree)	v_o (m/s)	G (kg)	Range (m)
Original design	5.48	2.93	25.45	1.0	8.17	914	67	32,670
Optimized	5.49	3.28	28.3	0.67	5.41	914	67	34,176

The results in Table 1 show that the 175 mm shells of the M107 cannon have approached the optimal performance. The optimized model has a range that is 5.22 percent greater than the original design. This indicates that the original design still has room for improvement.

The muzzle velocity of the 130 mm shells of model 59 cannons is 930 m/s, the mass is 33.4 kg, the maximum range is 27,490 m, the profile coefficient is $i_{43} = 0.93$, and the resistance coefficient is among the smaller ones of the projectiles of that vintage. The external profile of the 130 mm shell has one flaw: the tail is too short, only 0.23 times the shell diameter. The short tail caused a larger resistance and a shorter range. Through optimization, the range can be made 31,179 m without changing the muzzle kinetic energy and without resorting to base bleed. With base bleed, the range can be made 38,006 m. The increases in range through optimization are respectively 13.42 percent and 38.25 percent. This shows that optimization may be used to increase the range substantially.

Analysis of extensive calculations led to the following conclusions:

1. The length of the head of optimized projectiles is about 3.0 to 3.5 times the shell diameter. Others being equal, the head length is greater with base exhaust.
2. The length of the tail of optimized projectiles is about 0.6 to 1.0 times the shell diameter. Others being equal, the tail length is shorter with base bleed.
3. The best tail angle is about 4° to 8° . Others being equal, the tail angle is about 1° smaller with base bleed.
4. Over a wide range, the resistance coefficient decreases with increasing length-to-width ratio of the shell. But the flight stability is difficult to maintain at excessively large length-to-width ratio.
5. From the viewpoint of reducing resistance, the shorter the cylindrical portion the better. But from a flight stability viewpoint, the length of the cylinder should not be less than 1.4 times of the diameter without resorting to other measures, such as installing center stabilizing blocks.
6. The generating line of the head should cut the cylinder and the cut angle is generally 2 to 4 degrees. The cut angle is greater without base bleed.

References

1. Wang Deren [3769 1795 0066], "Nonlinear Equations: Solution and Optimization," Higher Education Publication Company, 1979.
2. He Xuchu [0149 2485 5902/0430] and Sun Lingping [1327 7792 1627], "Methods of Constrained Optimization," Nanjing University Publisher, 1986.
3. Pu Fa [3184 4099], "External Trajectory," Defense Industry Publication Company, 1980.
4. Tan Junjie, "A Calculation Method for the Longitudinal Aerodynamics of a Rotating Shell," Proceedings of the China Defense Engineering and Rocket and Missile Society, Vol 3, No 4, 1987.
5. Wei Huizhi [7614 1920 0027], "Projectile Design Theory," Defense Industry Publication Company, 1985.
6. Zhang Yanqing [1728 3508 3237], "Internal Trajectory of a Projectile With Base Bleeding," JOURNAL OF TRAJECTORIES, Vol 3, 1986.
7. Technical Report on the Development of Base Bleed Motors for the SRC-ERFB-MK 10 Mod 2 Projectile, SRC BB R/D 1710 (1983).

Effect of SiC Whisker on Mechanical Strength of Si_3N_4 Matrix Composites

92FE0150A Beijing GUISUANYAN XUEBAO [JOURNAL OF THE CHINESE CERAMICS SOCIETY] in Chinese Vol 19 No 4, Aug 91 pp 381-384, 311

[Article by Gu Peizhi [7357 1014 5365] and Xiao Yixin [5135 5030 2450] of Shandong Institute of Industrial Ceramics, others involved include He Jinji [0419 6210 1015], Zhang Weiru [1728 0251 0320], Fan Qisheng [2868 0796 8508], Xu Gang [1776 0474], Liu Qing [0491 3237], Yang Jingsheng [2254 0079 3932], and Ma Lieming [7456 0441 2494]: "Effect of SiC Whisker on Mechanical Strength of Si_3N_4 Matrix Composite"; MS received 1 Sep 90. Cf. JPRS-CST-91-021, 22 Oct 91 p 15]

[Text] Abstract

Si_3N_4 composites containing 10, 20 and 30 volume percent (vol%) SiC whisker were prepared and their room-temperature and high-temperature mechanical strengths were measured. Results clearly show that SiC whisker can significantly enhance the high-temperature mechanical characteristics of the matrix. The 20 vol% SiC whisker composite has a strength of 780 MPa at 1200°C. Compared to the matrix material, this is a 50 percent increase. The strengthening causes are discussed based on SEM and TEM results.

Key words: SiC whisker, strengthening, Si_3N_4 matrix composite

I. Introduction

In recent years a large number of studies¹⁻⁵ show that significant improvements in strength and toughness could be achieved by uniformly dispersing a certain amount of ceramic whisker in a ceramic matrix. The study on SiC whisker/ Si_3N_4 matrix composite (SC(w)/SN) is primarily concentrated in three areas. (1) Selection of whisker. The characteristics of the whiskers supplied by different manufacturers are quite different. Therefore, the source becomes very important. (2) Whisker and ceramic powder dispersion technique. Clustered whisker and powder often creates major defects in the composite, which limits its performance. (3) Physical and chemical compatibility between SiC whisker and silicon nitride matrix and sintering binder. The SiC whisker must have a higher elastic modulus and a slightly higher thermal expansion coefficient compared to the Si_3N_4 matrix. In order to have maximum strengthening and toughening effect, control of the interface state between whisker and matrix is critical.

The preparation of SC(w)/SN composite and the effect of SiC whisker on the mechanical strength of the material are described. It is found that the high-temperature strength of silicon nitride can be significantly enhanced by adding SiC whisker. The main mechanism of this strengthening effect and some potential strengthening and toughening factors are discussed based on study of its microscopic structure.

II. Experimental

β -SiC whisker (0.1-1 μm diameter, 50-200 length-to-diameter ratio) manufactured by Tokai Carbon Co., Ltd. of Japan and Si_3N_4 powder (>90 wt% α phase, 16 m^2/g BET specific surface, mean particle size < 0.2 μm) prepared by Shandong Institute of Industrial Ceramics were used in this work. Suitable amounts of sintering agents, such as Y_2O_3 , Al_2O_3 and ZrO_2 , were used to prepare 10, 20 and 30 vol% SC(w)/SN composite materials. The additive used is 6 wt% relative to the Si_3N_4 matrix.

SiC whiskers are dispersed ultrasonically in a liquid to become a stable slurry. This is mixed with a predetermined amount of ceramic slurry by a high-speed mixer. This mixture is dried and then hot-press-sintered for 1 hour at 1700-1750°C at a pressure of 20-30 MPa. The sintered disk is cut, ground, and polished to become 3 x 4 x 36 mm samples. They are used at room temperature and 1200°C in three-point bending strength tests. SEM analysis was done on the cross section and polished surface of the composites. TEM and microprobe electron-beam diffraction analyses were done to study its microscopic structure and interface state.

III. Results and Discussion

1. Density and Room-Temperature Bending Strength of the Composite

Figure 1 shows that the density of the composite decreases as the whisker content increases when the additive-to-matrix ratio remains constant. This is because the sintering agent only promotes the sintering of Si_3N_4 . SiC whisker must not undergo phase transition or contraction during sintering. In addition, the whisker acts as a bridge, which hinders the compacting process. As a result, the relative densities dropped from > 99 percent (Si_3N_4 matrix) to 97 percent, 95 percent and 89 percent, respectively, for 10 vol%, 20 vol% and 30 vol% SiC. Although the relative density is decreased after adding SiC whisker, there is still a significant strengthening effect. The strength of 20 vol% SC(w)/SN is 810 MPa, a 16 percent increase compared to 700 MPa for the matrix. As for 30 vol% SC(w)/SN, its strength drastically falls to 460 MPa due to very low density.

These results indicate that the strengthening effect would be enhanced if the density can be further increased.

2. High-Temperature Strength of SC(w)/SN Composite

Figure 3 shows that the high-temperature strength of the composite increases as the whisker content rises. The strength of the 20 vol% SC(w)/SN composite

at 1200°C is 780 MPa, which is a 50 percent increase compared to that of the matrix. As for the 30 vol% SC(w)/SN composite whose relative density is merely 89 percent, its strength at 1200°C is 650 MPa, which is 25 percent higher than that of the matrix and 40 percent higher than its own strength at room temperature.

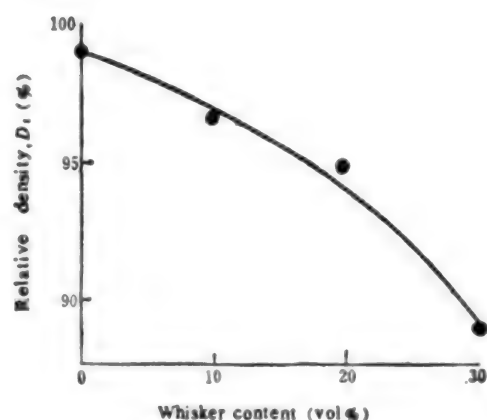


Figure 1. Relative Density of the Composites vs. Whisker Content

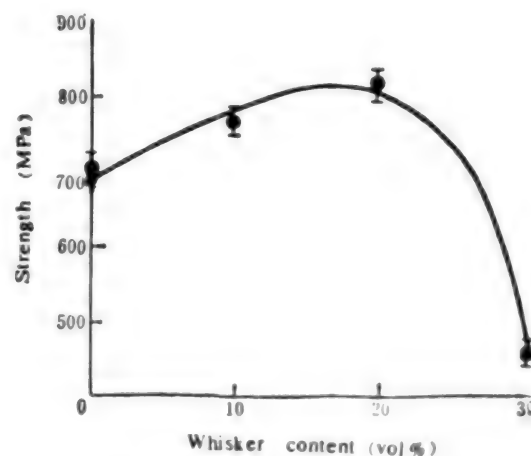


Figure 2. R.T. Bending Strength of the Composites vs. Whisker Content

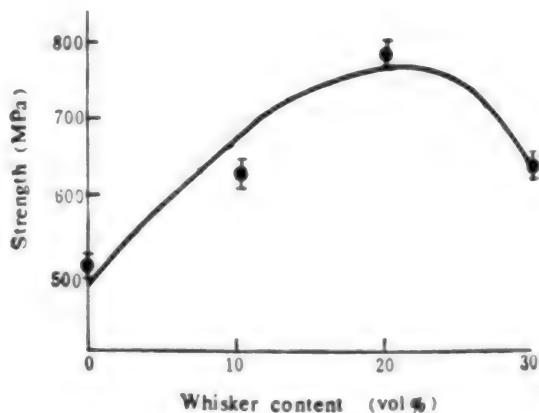


Figure 3. 1200°C High-Temperature Bending Strength of the Composite vs. Whisker Content

Figure 4 shows that compared to hot-pressed silicon nitride, SC(w)/SN composite has a better high-temperature strength retention ratio (high-temperature strength/room-temperature strength). At 1200°C, this ratio does not vary much for the composite. It is 96 percent at 1200°C and 70 percent at 1300°C. The strength retention ratio falls significantly for hot-pressed silicon nitride at 1000°C: at 1200°C, it is 70 percent and it drops to 50 percent at 1300°C.

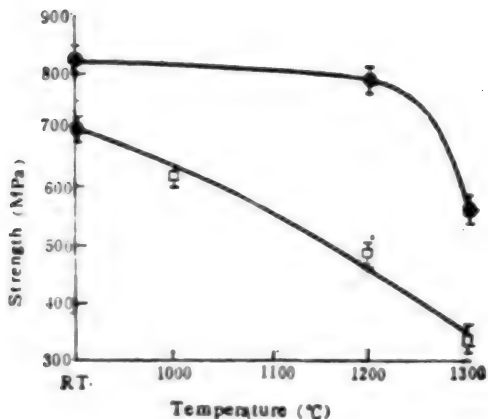


Figure 4. Bending Strength vs. Temperature for $\text{SC}(\text{w})/\text{SN}$ Composite and Hot-Pressed Si_3N_4
 □ Hot-pressed Si_3N_4 ; ● $\text{SC}(\text{w})/\text{SN}$ composite

To sum up, the addition of SiC whisker has significantly enhanced the high-temperature strength of the composite and improved the high-temperature weakening of silicon nitride at temperatures above 1000°C. The mechanical strength of the composite remains essentially constant at 1200°C. It has an excellent potential in high-temperature applications.

3. Mechanism for $\text{SC}(\text{w})/\text{SN}$ Strengthening by SiC Whisker

For a given system, a good technique is the key to preparing a superior composite. The whisker must be evenly dispersed in the matrix and it must have a good interface with the matrix. It is necessary to have very careful control.

Figure 5 [photograph not reproduced] shows a secondary emission (SE) electron micrograph of a polished sample of 20 vol% $\text{SC}(\text{w})/\text{SN}$. It shows uniform distribution of SiC whisker in the matrix. This demonstrates that the mixing and dispersing technique used is effective.

Figure 6 [photograph not reproduced] clearly shows the interface between SiC whisker and Si_3N_4 matrix. There is no sign of any violent reaction between the whisker and the matrix at the interface. This shows excellent chemical compatibility between SiC whisker and Si_3N_4 matrix in the composite prepared.

Figure 7 [photograph not reproduced] shows that SiC whiskers and the long cylindrical β' - Si_3N_4 crystals are closely intertwined. There is very little amorphous structure in between. This tight three-dimensional structure enables the material to maintain high mechanical strength at high temperature.

Figure 8 [photograph not reproduced] shows propagation of stress cracking (SC) of the composite along the SiC whisker/ Si_3N_4 crystal interface. It is deflected many times and is associated with fracturing of Si_3N_4 . This illustrates an important mechanism of the strengthening effect of SiC - crack deflection.

Figure 9 [photograph not reproduced] is the SEM picture of the fracture surface of 20 vol% SC(w)/SN composite. The characteristics include a rough and uneven surface which is typical for crack deflection. The fracture also shows broken SiC whisker and separation of SiC whisker from the matrix interface, which are signs of different toughening and strengthening mechanisms.

IV. Conclusions

SiC whisker can significantly improve the mechanical strength, particularly high-temperature strength, of Si_3N_4 matrix. 20 vol% SC(w)/SN composite has a high-temperature strength of 780 MPa at 1200°C which is 96 percent of the strength at room temperature. Compared to the high-temperature strength of the matrix, it is increased by 50 percent.

References

1. G.C. Wei and R.F. Becher, AMER. CERAM. SOC. BULL., 64[2] (1985) 298.
2. C. Greskovich and J.A. Palm, J. AMER. CERAM. SOC., 63[9-10] (1980) 597.
3. G. Peizhi, Z. Weiru, X. Yixin, et al., 3rd Inter. Symp. on Ceramic Material and Components for Engines, Proc. (1988) 260.
4. S.T. Buuljan, J.G. Baldoni and M.L. Huckabee, AMER. CERAM. SOC. BULL., 66[2] (1987) 347.
5. P.D. Shalek, et al., AMER. CERAM. SOC. BULL., 65[2] (1986) 351.

1

LASERS, SENSORS, OPTICS

Development of Flash X-Ray Machines at CAEP

92FE0092A Chengdu QIANG JIGUANG YU LIZI SHU [HIGH-POWER LASER AND PARTICLE BEAMS] in Chinese Vol 3 No 3, Aug 91 pp 269-285

[Article by Tao Zucong [7118 4371 5115], Zhang Shouyun [728 1108 0061], and Liu Xisan [0491 6932 0005] of the China Academy of Engineering Physics (CAEP): "Development of Flash X-Ray Machines at CAEP"; MS received 12 Mar 91, revised 18 Apr 91]

[Excerpts] Abstract

Flash X-ray technology has been developed at CAEP for over 30 years. It plays an important role in the study of detonation physics and gamma-ray radiation effects. This paper summarizes the development of several flash X-ray machines at CAEP, including progress made in high-voltage pulse technology, field emission technology and high-power beam focusing technology. Major parameters of these machines are also described. Flash X-ray machines are important tools in the study of detonation physics and high-speed transient processes. The development of large-scale flash X-ray machines has some significance in defense-related technology. New applications for high-power electron beams are also discussed.

I. Introduction

Flash X-ray technology has been developed for over 30 years at CAEP. It plays a vital role in detonation physics and gamma-ray radiation effects.¹ The major characteristics of flash X-ray penetrating radiography include:

- (1) Capability to unveil transient structures and high-velocity motion;
- (2) Providing complete visual pictures to clarify the physical concept.

Therefore, together with other electrical (such as probe and microwave) and optical (such as high-speed rotating mirror and laser hologram) methods, this technology becomes the primary tools for studying high-velocity transient processes. It is widely used in detonation physics, implosion kinetics, shock-wave physics, and high-energy explosives for studying high-pressure equation of state, shock-wave compression, laminar fracture effects and jet flow. It can also be used to study internal trajectory, armor and anti-armor

development, and transient effects in fields such as plasma physics, materials, biology and medicine. In arms research, flash X-ray radiography provides a basis for controlling the explosion pattern, verifying the computer program and optimizing the design. Detonation physics work done at CAEP provides a great push to move flash X-ray technology forward. At the same time, flash X-ray technology makes it possible for detonation physics to reach a more profound level.

This is a summary of intense-current accelerator technology developed at CAEP for flash X-ray radiography. Advances in high-voltage pulse technology, field emission technology and intense beam focusing are described. In addition, major technical specifications for a number of machines are introduced.
[passage omitted]

III. Overview of Development of Flash X-Ray Machines

CAEP began to get involved with flash X-ray technology in the late 1950's with the development of a microsecond-level flash X-ray machine using a Marx generator. In the late 1960's, nanosecond-level high-voltage pulse technology was developed. In the 1970's, CAEP switched to the development of a pulsed transmission-line-type intense-current flash X-ray machine. In the 1980's, CAEP began to develop an inductive linear-accelerator-type (induction linac) high-power flash X-ray machine.³⁻⁶ Five flash X-ray machines have been developed to date, and are used in various detonation-experiments facilities and laboratories to solve a series of practical problems. In the development process, CAEP received cooperation from many outside organizations. Some results are being widely used in China. The major technical parameters of some typical flash X-ray machines are listed in Table 1.

Table 1. Output Characteristics of Some Typical Flash X-Ray Machines

Machine	Kind	Voltage (MV)	Current (kA)	Pulse width (ns)	Dose (at 1m) (R)	Spot (mm)	Jitter (μs)	Start- up	Note
X	SCYF type Marx	1.5*	5.2*	400	0.4	6	0.5	1964	4 sets made
X-A	SIMPAC Marx	3	8	40	0.4	10	0.1	1972	industry production
X	water Blumlein line	0.8	30	50	0.8	6	0.1	1977	3 sets combined
X-A	oil Blumlein line	0.75	8	40	0.6	8	0.1	1974	beam physics research
Flash-1	oil Blumlein line	6.1	20	80	200	6~8	0.1	1983	radiation source and radiography
MEI-	induction linac	4	2	30	10	8	0.1	1990	being upgraded; electron energy

* This voltage is nominal value; in fact the 3-stage voltage 300kV

Number 1 is currently involved in the diode current

[Passage omitted]

Although the energy utilization efficiency of an induction-free capacitive Marx generator is relatively high, it cannot easily store a great deal of energy. Thus, its development was limited. The pulse transmission line played an important role in the formation of nanosecond-level high-voltage square-wave pulses. J.C. Martin at the British Atomic Weapons Research Center first successfully applied transmission-line technology to pulse power research, which created a new era for flash X-ray technology.⁷ A transmission line, added between the Marx generator and the X-ray diode, could compress microsecond pulses from the generator into nanosecond high-voltage pulses. In the 1970's, 1 MV oil-dielectric and 1 MV water-dielectric transmission line flash X-ray machines were developed. On this basis, in 1975 CAEP began to design and construct a large intense-current pulse electron-beam accelerator, Flash-I, as shown in Figure 5. Flash-I is a high-impedance, high-voltage, high-current accelerator designed for gamma-ray radiation effects studies. It could also meet the requirements for flash X-ray radiography, and is a multi-purpose machine. In-depth research was done on intense electron-beam focusing,⁸ synchronous jitter⁹ and stability of operation; very satisfactory results were obtained. Flash-I has raised the standard of flash X-ray radiography to a new level.



Figure 5. Flash-I Photograph

The voltage of a typical Marx-generator/transmission-line flash X-ray machine cannot reach too high because it is limited by high-voltage insulation. In addition, the beam quality (emissivity and energy dispersion) of this type of flash X-ray machine is relatively poor. It is difficult to obtain a small focal point. In order to obtain higher-energy X-ray output and better beam focusing, CAEP in the early 1980's began to develop an intense-current (1-10 kA) electron induction linac with multiple accelerating gaps, a type which combines the advantages of high-power pulse technology and linac technology. The voltage wave has a better plateau, a more stable current-time profile and a smaller energy dispersion, which provides better conditions for beam focusing. Figure 6 [photograph not reproduced] is a picture of the

4 MeV induction linac already completed. This linac consists of 12 series-connected accelerating elements. Electron energy rises with increasing number of accelerating elements, and it is possible to add accelerating elements based on demand. The completion of this accelerator provides a basis for increasing accelerator energy in the future. It has also brought flash X-ray technology at CAEP into a new stage. [passage omitted]

VI. New Applications of Intense Electron Beams

CAEP has developed intense electron-beam technology as a result of conducting research on flash X-ray radiography and gamma-ray radiation effects. Intense electron beams are now used in many important research areas. In recent years, CAEP has actively been pursuing the following two areas.

1. Free Electron Lasers (FEL)

With advantages such as high power, high efficiency, tunable wavelength and high beam quality, the FEL attracts a great deal of attention worldwide. FEL experiments require a bright electron beam with low emissivity and low energy dispersion. This is the direction of research on intense-current accelerators at CAEP. In recent years, technological improvements have been made on the XII-A oil transmission-line accelerator to upgrade the voltage waveform and beam quality to begin experimental work on a Raman FEL.

Using an annular electron beam at 440 kV and 1 kA and a 1-m-long doubly wound solenoid wiggler, a 3 MW spontaneous radiation amplification output at 28-30 GHz was obtained. Experiments on a solid-core amplifier followed immediately. In these two sets of experiments, a strong axial magnetic field was used to focus the electron beam. The presence of an axial magnetic field not only generates cyclotron radiation, but also complicates the electron trajectory; this makes theoretical analysis more difficult. In order to avoid these complicating factors, we designed Raman-FEL experiments which do not require a guiding magnetic field. A transverse magnetic field generated by a doubly wound solenoid was used to control the transport of the intense beam. Without any doubt, this requires even higher-quality electron beams. Experimentally, at 560 kV, 110 A, $\epsilon < 0.04 \text{ cm-rad}$, $\Delta E/E < 5 \text{ percent}$, saturation was observed when the length of the wiggler was lengthened to 1.5 m. The saturated power output is 7.5 MW at 35-38 GHz.¹⁶ The success of the zero-guiding-field Raman FEL experiment is an encouraging milestone in the development of FELs in China.

An experimental FEL, the SG-1, using an induction linac as its electron source, is being installed and tested.¹⁷ A 3.5 MeV, 1.5 kA, 90 ns electron beam generated by the linac is selected for emissivity and energy dispersion in a current modulation zone to supply a suitable electron beam that meets the FEL requirements. From the design of the waveguide millimeter FEL, based on the program FRED developed at Livermore Laboratory, a three-dimensional numerical simulation program WAGFEL¹⁸ was written to optimize the SG-1 design. The design parameters for the wiggler and electron beam are shown in Table 4. The wiggler is a 3-m-long bi-directional focusing linearly polarized electromagnet (with a parabolic magnet surface). Computer simulation shows that when

the microwave power input is 20 kW at 34.6 GHz, the amplified peak output is expected to reach 10^8 W. The completion of this facility is of great significance to the study of FEL operating mechanisms and the control of FEL experimental technology.

Table 4. SG-1 FEL Design Parameters

Electron beam	Wiggler
energy : $E = 3.5 \text{ MeV}$	wiggler period : $\lambda_w = 11 \text{ cm}$
beam current : $I = 450 \text{ A}$	wiggler magnet field : $B_z = 3.1 \text{ kGs}$
normalized emittance : $\epsilon_n = 0.47 \text{ cm} \cdot \text{rad}$	period number : $N = 30$
beam brightness : $B_b = 4.1 \times 10^7 \text{ A} \cdot (\text{m} \cdot \text{rad})^2$	wiggler parameter (rms) : $a_w = 2.2$
energy spread : $\Delta E/E \leq 3\%$	
beam radius : $r_b = 0.8 \text{ cm}$	

2. High-Power Microwaves (HPM)

Experiments on the production of HPM with intense electron beams are very intriguing. Microwave sources with power ranging from several hundred MW to several dozen GW in the frequency range of 1-100 GHz are of substantial military interest, and provide the means to study electronic warfare, weakness of weapons against microwaves, electromagnetic coupling and long-range radar. Furthermore, there is the potential that HPM weapons can be used in the future.

One feasible scheme is to use the intense electron beam generated by Flash-I to produce GW-level microwaves. D. Sullivan¹⁹ first proposed using a virtual cathode oscillator (VIRCATOR) in 1979. The VIRCATOR is different from other microwave sources and has two distinct features: (1) It neither uses a resonant structure nor a long interaction zone between the electromagnetic wave and the electron beam. (2) It operates in a state much higher than the space-charge-limited current level. Its operating mechanism is as follows: When the current injected into the drift tube exceeds the space-charge-limited current I_{L} , we have:

$$I = I_{\text{L}} \frac{(\gamma^{1/2} - 1)^{1/2}}{1 + 2 \ln R/r_b} \quad (\text{kA}) \quad (17)$$

Here, a virtual cathode is formed not far away from the anode. In the equation, γ is a relativistic factor, R is the radius of the drift tube, and r_b is the electron-beam radius. The position of the virtual cathode and the potential barrier height vary periodically with time and oscillate. Electrons also oscillate between the cathode and virtual cathode. Both modes of oscillation generate microwaves. The basic frequency of microwave radiation is:

$$f = 2 \pi \omega_c \quad (18)$$

where $\omega_p = \left(\frac{n_0 e}{m} \right)^{1/2}$ is the plasma frequency, n_0 is the electron density, e is the electron charge, m_0 is the electron mass, γ is the relativistic factor, and ϵ_0 is the dielectric constant in vacuum. The coefficient a varies between $1/2\pi$ and $1/\sqrt{2}\pi$ depending upon the strength of the virtual cathode. In order to raise the virtual cathode oscillation efficiency and improve the frequency spectrum, it is necessary to suppress electron reflection in order to eliminate competition and interference between these two mechanisms. When beam-transport experiments were done on an XII-A accelerator, intense microwave radiation was found²⁰ as the thin-lens focusing magnetic field was turned up to 20-40 kGs. This is the microwave radiation from virtual cathode oscillation. In order to investigate the mechanism of a VIRCATOR and to obtain HPM output, we lowered the diode impedance of Flash-I to conduct experiments on the VIRCATOR. The HPM experimental design parameters of Flash-I are shown in Table 5. This is CAEP's first milestone in HPM research. On this basis, in conjunction with other microwave generation studies, HPM technology will advance at CAEP.

Table 5. HPM Experiment Design Parameters of Flash-I

Diode voltage*	$V = 5MV$
Beam current	$I = 100 - 120kA$
Plasma current	$I_p = 50kA$
Virtual cathode current	$I_v = 40kA$
Drift zone radius	$R_d = 1.7m$
Beam radius	$R_b = 1.3m$
Beam density	$n_b = 1 \times 10^{18} cm^{-3}$
Microwave frequency	$f = 1GHz$
Microwave power	$P = 1GW$

Acknowledgement: The authors wish to thank Professor Wang Ganchang [3769 3137 3490] for his guidance and concern and Mr. Huang Shiming [7404 3711 2494] for his participation in the development of flash X-ray techniques at CAEP. The summary includes a large number of studies conducted by people involved in high-power pulse technology and intense-current accelerator technology at CAEP. In device development, many organizations have offered assistance and support.

References

1. Wang Ganchang, "High-Power Particle Beams and Their Applications," "JIANG JIGUANG YU LIJI SHE (HIGH-POWER LASER AND PARTICLE BEAMS)" in Chinese Vol. 1, No. 7, 1989, p. 5.
2. T.H. Martin, "A Computerized Method of Producing Electromagnetic Bremsstrahlung Radiation With Specific Application to High-Voltage Flash X-Ray Machines," SC-RB-89-141, 1989; R.A. Lucht and S. Eckhouse, "Intense X-Ray Machine for Penetrating Radiography," LA-UR-89-1935, 1989.

1. Liu Xisan, "Development of Flash X-Ray Machine Testing Technology at CAEP," Proceedings of the National Experimental Aerodynamic Non-Contact Measurement Conference, 1978.
2. Li Yannian [2621 1693 1628] et al., "Study of Using XII Flash X-Ray Machine for Explosion Measurement," BAOZHA YU CHONGJI [EXPLOSIONS AND SHOCK WAVES], Vol 3, No 2, 1983, p 57.
3. Xu Yizhi [1776 1355 1807] et al., "Flash-I Intense-Current Pulsed Electron Beam Accelerator," YUANZIHE WULI [NUCLEAR PHYSICS], Vol 9, 1987.
4. Ding Bonan et al., "Preliminary Debugging of 1.5 MeV Induction Linac," QIANG JIGUANG YU LIZI SHU [HIGH-POWER LASER AND PARTICLE BEAMS] in Chinese Vol 1, No 1, 1989, p 92.
5. J.C. Martin, Internal Report, SSWA/JCW/704/49 AWRE, England, 1970.
6. Liu Zusheng [0491 4371 3932], "Study of Self-Focusing of Intense Electron Beam," Volume 1 of Technical Report from the Institute of Applied Electronics of CAEP, "High-Power Pulse Technology and Free Electron Lasers," 1976, p 73.
7. Dye Kigang [6508 6932 0474], "Improvement of Synchronization of Flash-I," China Academy of Engineering Physics, Technical Journal, Proceedings of Symposium on High-Power Pulse Technology, 1986.
8. R.A. Mishadze, "Production of High-Power Nanosecond Pulses" (in Russian), Atomic Energy Publishing House, 1982.
9. Zhang Enguan [1728 1869 1351], et al., "Development of Pulse Power Modulation System for LIA Elements," QIANG JIGUANG YU LIZI SHU [HIGH-POWER LASER AND PARTICLE BEAMS] in Chinese Vol 2, No 1, 1990, p 39.
10. R.B. Miller, "Physics of Intense Charged Particle Beams," Atomic Energy Publishing House, 1990.
11. J.D. Lawson, J. ELECTRON, Vol 5, 1958, p 146.
12. J.D. Lawson, "Physics of Charged Particle Beams," Atomic Energy Publishing House, 1988.
13. Liu Chengjun [0491 2110 0193], "Focusing of Intense Electron Beam Under Solenoid Magnetic Lens," Proceedings of the Fourth National Conference on High-Power Particle Beams, Xian, 1990.
14. Hu Kesong [5170 0344 2646] et al., "Zero-Guiding-Field Raman-FEL Experiment," QIANG JIGUANG YU LIZI SHU [HIGH-POWER LASER AND PARTICLE BEAMS] in Chinese Vol 2, No 2, 1990, p 158 [cf. JPRS-CST-91-022, 12 Nov 91 pp 22-33].
15. He Zhongxi [1920 6988 6932], "Design Study of Shuguang-I FEL Apparatus," QIANG JIGUANG YU LIZI SHU [HIGH-POWER LASER AND PARTICLE BEAMS]

in Chinese Vol 2, No 3, Aug 90 p 257 [translated in full and published in JPRS-CST-91-014, 24 Jun 91 pp 1-23].

18. Yang Zhenhua [2799 7201 5478] et al., "Theoretical Design of a 3.5 MeV Millimeter-Wave FEL," Proceedings of the Fourth Annual FEL Meeting of CAEP, 1989, pp 5-18.

19. D. Sullivan, "Application of Virtual Cathode in Relativistic Electron Beams," Proceedings of the Third International Conference on High Power Electron and Ion Beam Research and Technology, Novosibirsk, Soviet Union, Vol 2, 3-6 July 1979, p 769.

20. Wang Pingshan [3769 1627 1472], "Microwave Emission From a Virtual Cathode Source," QIANG JIGUANG YU LIZI SHU [HIGH-POWER LASER AND PARTICLE BEAMS] in Chinese Vol 2, No 3, 1990, p 319 [abstracted in JPRS-CST-91-011, 31 May 91 pp 20-21].

VIRCATOR-Generated High Power Microwave Particle Simulation

92FE0092B Chengdu QIANG JIGUANG YU LIZI SHU [HIGH-POWER LASER AND PARTICLE BEAMS] in Chinese Vol 3 No 3, Aug 91 pp 315-322

[Article by Shu Ting [5289 2185], Wang Min [3769 7044], Chen Deming [7115 1795 2494], and Li Chuanlu [2621 0278 5251] of the Department of Physics, National University of Defense Technology, Changsha, a project funded by the National Natural Science Foundation: "VIRCATOR-Generated High Power Microwave Particle Simulation"; MS received 12 Aug 90, revised 15 Nov 90]

[Text] Abstract

A cylindrically symmetric, 1 1/2D relativistic electromagnetic plasma particle simulation code with non-periodic boundary has been developed. It is used to study the high power microwaves (HPM) produced from virtual cathode oscillation by injecting an intense relativistic electron beam into a waveguide with one end open and the other end closed. Very clear and reasonable physical pictures are obtained. Virtual cathode oscillation frequency is in agreement with the empirical expression $(1 - \sqrt{2\pi})\omega_{peb}$. Microwave efficiency is as high as 10 percent. In addition, by way of simulation, the dependence of radiation frequency and radiation efficiency on the external guiding magnetic field, electron beam intensity, electron beam energy and electron beam radius is investigated. Some valuable patterns are obtained.

I. Introduction

Production of an HPM output by virtual cathode oscillation generated by the injection of an intense relativistic electron beam into a waveguide has attracted widespread attention and research efforts on a considerable scale. The principle is as follows. When a relativistic electron beam is transported through space, because the electron carries a negative charge, a negative potential well is created in space which hinders the transport process. When the electron-beam density transported is greater than the space-charge-limited current density,^{1,2} some electrons are reflected by the space charge well. This negative potential region which reflects electrons is the virtual cathode, which varies with space and time in a periodic fashion.^{3,4} An intense current oscillation can be excited to produce coherent HPM through waveguide coupling. A theoretical model⁷ and computer

simulations^{5,6} indicate that there is a certain relation between virtual cathode oscillation frequency ω_{VC} , i.e., excited microwave frequency, and plasma electron beam frequency ω_{peb} . The authoritative empirical equation is

$$\omega_{VC} = (1 \sim \sqrt{2\pi}) \omega_{peb} \quad (1)$$

Here, the plasma electron beam frequency is:

$$\omega_{peb} = \sqrt{\frac{4\pi n_b e^2}{\gamma_0 m_e}} \quad (2)$$

where n_b is the electron beam density and γ_0 is the relativistic factor for the initial electron velocity.

When an annular relativistic electron beam is injected into a cylindrical waveguide of infinite length, the expression for space-charge-limited current is:⁸

$$I_{SCL} = \frac{m_e c^3}{e} \frac{(\gamma_0^{2/3} - 1)^{1/2}}{\frac{\Delta r_b}{r_b} + 2 \ln \frac{R}{r_b}} \quad (3)$$

where c is the speed of light, Δr_b and r_b are the thickness and radius of the electron beam, and R is the radius of the waveguide.

As far as injecting a relativistic electron beam into a cylindrical waveguide of finite length is concerned, so long as the following equation is valid

$$\frac{L}{R} \geq 2.58 \left(\frac{r_b}{R} \right)^{0.1333} \quad (4)$$

the space-charge-limited current of this waveguide can be calculated using equation (3).⁹

When the current injected into a waveguide, I_0 , is greater than I_{SCL} , it forms a stable virtual cathode oscillation to generate microwaves.

Compared to other HPM sources, a VIRCATOR has the following advantages:
 (1) Its requirement for a high-quality electron beam is less stringent which makes it easier to obtain. (2) Its electron-beam utilization rate is high. Therefore, unlike other devices, in order to get a high-quality electron beam, most of the electron beam is lost as a result of waveform shaping. Hence, it is easier to obtain HPM. Usually, a VIRCATOR can reach GW power level. (3) The device is simple in structure and easy to build. (4) The microwave frequency is continuously tunable. The coefficient in equation (1) is dependent upon I_0/I_{SCL} . Therefore, by varying the injected current I_0 , changing the geometric size of the device to vary I_{SCL} , varying the beam density n_b and beam energy γ_0 , it is possible to continuously affect the microwave radiation frequency. This is why using a VIRCATOR as an HPM source has received so much attention and in-depth research.

Virtual cathode oscillation is a strong nonlinear plasma process. Therefore, rigorous theoretical analysis becomes very difficult. Especially during oscillation, a portion of the electron beam is transmitted and the rest is reflected. This makes it difficult to describe with fluid equations. In this work, the entire process is studied by computer simulation, specifically plasma particle simulation. A computer is used to track the motion of a large number of charged particles in an electromagnetic field and the associated electromagnetic field generated. The information provided is more accurate than the approximation derived from fluid dynamics.

II. Computational Model

The model involved is shown in Figure 1. The device is cylindrically symmetric. A hollow (or solid) intense relativistic electron beam (REB) is injected into a cylindrical waveguide of finite length from the left. The left end is closed and the right end is open. The length of the waveguide is L , its radius is R , the beam radius is r_b , and the beam thickness is Δr_b . The entire waveguide is submerged in an axially homogeneous magnetic field B_{z0} .

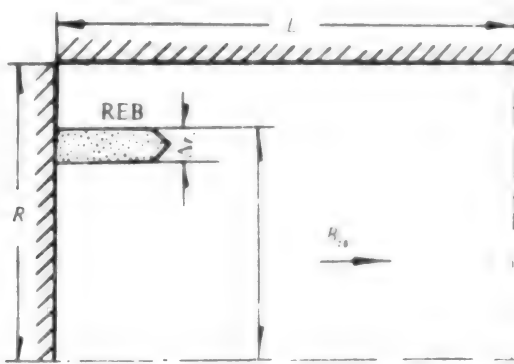


Figure 1. Configuration of the Model

The model includes the following assumptions:

1. The function of the guiding magnetic field B_{z0} is to confine any large-scale radial motion of injected electrons. Hence, there is no change in the radial coordinate; there are only axial coordinate changes. There is no angular coordinate change as well. However, electrons are allowed to move radially and angularly so that the velocities in these two directions contribute to the radiation electromagnetic field. This one-directional coordinate and three directions of velocity is the 1 2/2D assumption.
2. The left end of the waveguide is metallic. It, like the other sides of the waveguide, is an ideal conductor; it is capable of absorbing electrons and reflecting electromagnetic waves completely. The right end can completely absorb electrons and emit microwaves. Electromagnetic waves are not reflected at this end surface.
3. Single-energy electrons are injected from the left. The electron beam is cold and has an axial velocity component only.

If the one-dimensional beam current traveling along the axial magnetic field exceeds the limiting current, a virtual cathode is created which continues to oscillate axially. As a result, an oscillating axial electric field $E_z(t)$ is produced. By way of waveguide coupling, an axially symmetric transverse waveguide mode $TM_{0n}^{10,11}$ is produced. Thus, the major field variables are E_r , E_z and B_ϕ . The Maxwell equations to be solved are:

$$\left. \begin{aligned} \frac{\partial E_r}{\partial t} &= \frac{c}{r} \frac{\partial}{\partial r} (r B_\phi) - 4\pi J_r \\ \frac{\partial E_z}{\partial t} &= -c \frac{\partial B_\phi}{\partial z} - 4\pi J_z \\ \frac{\partial B_\phi}{\partial t} &= -c \left(\frac{\partial E_r}{\partial z} - \frac{\partial E_z}{\partial r} \right) \end{aligned} \right\} \quad (5)$$

Let $t = 0$ when electron injection begins. At that moment, the waveguide is in vacuum. Therefore, the initial conditions are

$$\left. \begin{aligned} E_r(r, z, t)|_{t=0} &= 0 \\ E_z(r, z, t)|_{t=0} &= 0 \\ B_\phi(r, z, t)|_{t=0} &= 0 \end{aligned} \right\} \quad (6)$$

Based on the assumptions described earlier, the boundary conditions are

$$\left. \begin{aligned} E_r(r, z, t)|_{z=R} &= 0 \\ E_z(r, z, t)|_{z=0} &= 0 \\ B_\phi(r, z, t)|_{z=0} &= 0 \end{aligned} \right\} \quad (7)$$

As for the open end, in order to ensure that the electromagnetic waves travel outward without any reflections, the waveguide is artificially lengthened a bit. Furthermore, it is assumed that the inside dielectric has a constant electrical conductivity to become an absorption layer. All waves traveling to the right are absorbed without any reflection.

The electron equation of motion in the system is:

$$\frac{dp_i}{dt} = -e(E_i + \frac{v_i \times B_i}{c}) \quad (8)$$

where p_i and v_i represent the momentum and velocity of particle i ; E_i and B_i represent the electric field and magnetic field of particle i in space at time i . All equations are converted into the center difference format. Each particle contributes to current and charge distribution in its surrounding cells. The magnitude is inversely proportional to its distance from the cell point. Once the current density is obtained, it is possible to solve the difference equations to calculate the electromagnetic field. By means of interpolation, the electric and magnetic field at every point where a particle

is located can be obtained. Each particle is a "finite-size particle."¹² This means that all particles are treated as "super particles," which are charges of a certain size distributed in space when we consider the effect of force exerted on them and how they contribute to the spatial electromagnetic field. Their effect is taken into account in R space after a fast Fourier transform.^{12,13}

III. Simulation Results

The entire model involved the tracking of a total of 60,000 particles. The system constantly maintains approximately 8,000 particles. The waveguide is divided into 56 cells radially and 256 cells axially. The time step is $0.06 \omega_{peo}^{-1}$, where ω_{peo} is the plasma frequency when the electron beam is not moving. The result of a simulation exercise is presented below as an example to discuss the physical process of generating HPM with a VIRCATOR. The parameters used are: $R = 1.2$ cm, $L = 5.52$ cm, $r_b = 0.9$ cm, $\Delta r_b = 0.1$ cm, $\gamma_0 = 7.0$, $I_0 = 500$ kA and $B_{z0} = 90$ kGs. In this example, the calculations show that $I_{SCL} = 106$ kA. It is obvious that a virtual cathode can be formed; energy conservation is maintained throughout the entire simulation process. Figure 2 shows the electron phase diagram, i.e., distribution of momentum p_z as a function of particle location z , at $t = 124 \omega_{peo}^{-1}$. This diagram clearly shows the virtual cathode in the waveguide. Charged particles are reflected in a specific region in the z direction, i.e., p_z is zero or negative. The virtual cathode is located in the $(2.6-6.6)\Delta z$ range, which is very close to the left end surface where electrons are being injected. Under the influence of this negative potential, some electrons penetrate the barrier and some are reflected. This reflection and oscillation of current in the area serves as a current source to generate intense microwaves inside the waveguide. The current penetrating the potential barrier is $I_t = I_0/7.0$, which is less than the limiting current. Hence, it will not form another virtual cathode. Simulation shows that there is only one virtual cathode formed inside the waveguide. Penetrating electrons generate several velocity peaks under the influence of spatial electromagnetic waves. Nevertheless, overall velocity is always positive, providing a stable beam transport; it does not contribute much to the microwave radiation.

Figure 3 shows trajectories of charged particles. The reentry points fall within the virtual cathode region. Because the electron beam does not exist at the beginning, it takes some time for the virtual cathode to form and stabilize. Therefore, electron penetration and reflection are even when $t < 120 \omega_{peo}^{-1}$. The virtual cathode remains essentially at the same position. However, when $t > 120 \omega_{peo}^{-1}$, sometimes there is more reflection and sometimes more penetration. The reentry point, i.e., position of the virtual cathode, oscillates with time. This indicates that a stable oscillation has been achieved.

Figure 4 shows the radial distribution of electric field E_z at $z = 5.52$ cm and $t = 620 \omega_{peo}^{-1}$. Because there are seven points below 0, the primary electromagnetic field mode in the waveguide is TM_{07} . E_r and B_ϕ have similar radial distributions.

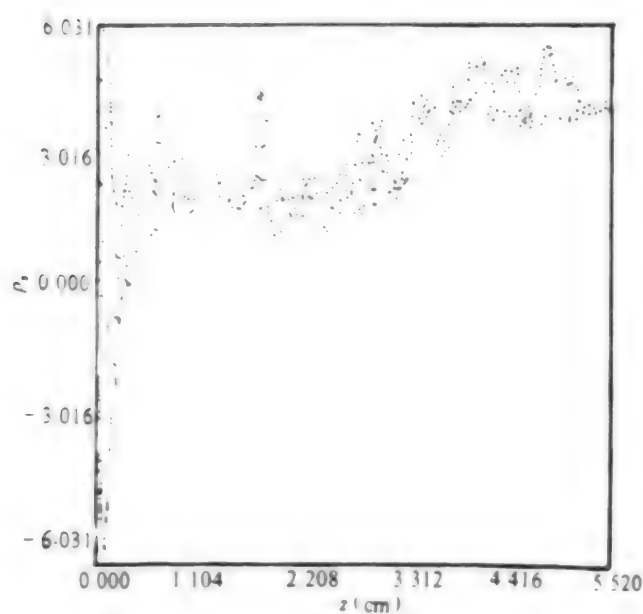


Figure 2. Phase Diagram of Charged Particles ($L = 128\Delta z$)

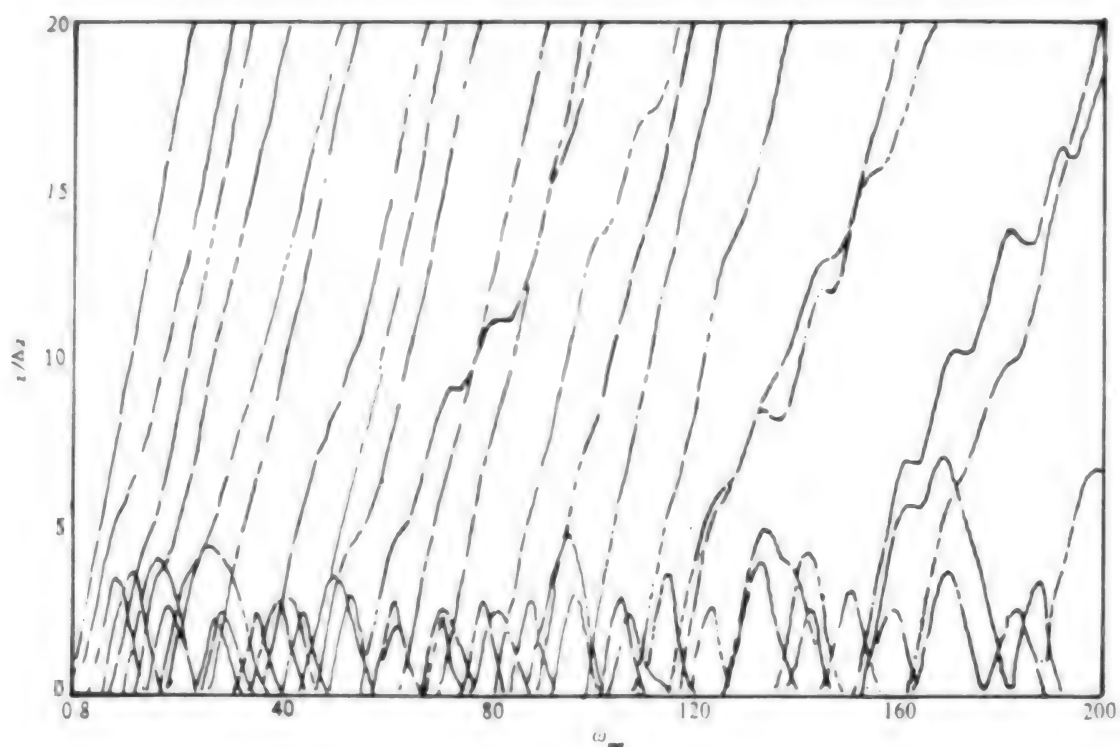


Figure 3. Orbits of Charged Particles

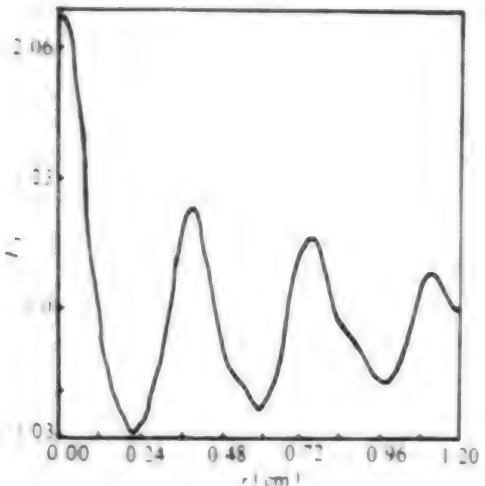


Figure 4. Electrical Field E_z Versus Radius

Figure 5 shows electric field component E_z versus axial location at $r = 1.0$ cm at the same moment. There are five waves along the axial length of the waveguide.

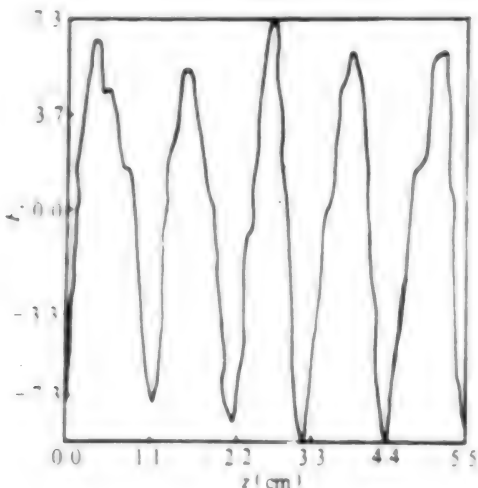


Figure 5. Electrical Field E_z Versus Axial Location

Looking at E_z versus time at $r = 0.64$ cm and $z = 5.52$ cm, one can see that E_z oscillates periodically in a stable fashion with time. A frequency analysis is shown in Figure 6. The main frequency of the microwave is $0.7 \omega_{peo}$. Since $\omega_{peo} = (4\pi n_b e^2/m_e)^{1/2}$, the fundamental microwave frequency is $1.85 \omega_{peo}$ which is within the frequency range shown in equation (1). In addition, it was found that the radial wave vector k_{r07} shown in Figure 4 and k_z shown in Figure 5 basically meet the dispersion relation for the TM_{01} waves at this fundamental microwave frequency:

$$\frac{\omega^2}{c^2} \approx k_{r07}^2 + k_z^2$$

This indirectly verifies the reliability of the model.

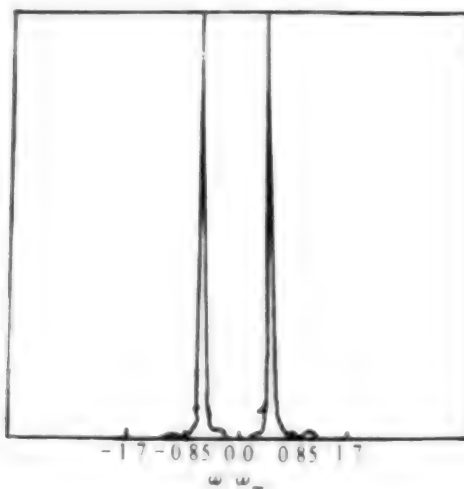


Figure 6. Power Spectrum of Electrical Field E_r

The current density versus time function was found to oscillate periodically near the virtual cathode at $r = 0.9$ cm and $z = 0.35$ cm. Figure 7 shows its frequency spectrum. Its fundamental frequency is also $0.7 \omega_{peo}$, consistent with the fundamental microwave frequency. This indicates that the intense VIRCATOR current is the primary source for generating the microwaves. Nevertheless, there are many other branch frequency current components. Due to the frequency selection effect of the waveguide, these side frequencies do not generate intense electromagnetic waves. The results also show that the intensity of J_z oscillation near the virtual cathode is much higher than that of J_r (approximately 10^2 different in magnitude). Hence, J_z oscillation is the principal mechanism for microwave radiation.

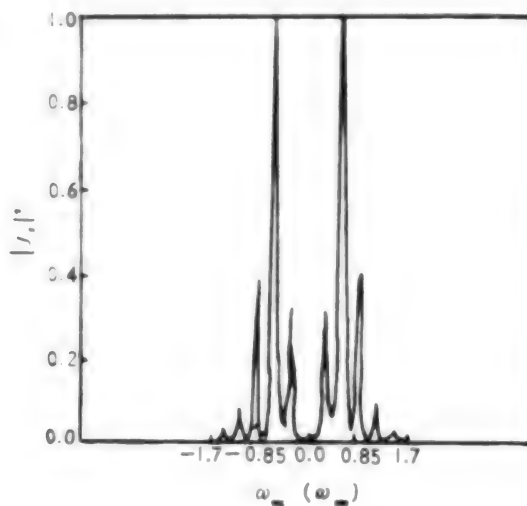


Figure 7. Power Spectrum of Current Density J_z

V. Factors Affecting Microwave Radiation

In order to investigate the impact of waveguide structural parameters and electron-beam characteristics on the frequency and radiation efficiency of VIRCATOR-generated microwaves, computations were made with a variety of parameters to explore a pattern. The conclusions obtained are as follows.

A. Effect of Guiding Magnetic Field B_{z0}

Let us use the same structural parameters as those in the above example, but change the axial guiding magnetic field B_{z0} . The relation between guiding magnetic field and microwave radiation efficiency is shown in Figure 8. Microwave radiation is the mean ratio of microwave radiation energy to total energy of electron injection over a certain period of time. Microwave energy is the time integral of the integral of the wave vector at the outlet of the waveguide with respect to area. The stronger the magnetic field is, the more it confines the transverse motion, i.e., v_r and v_θ , of the electron. It also affects microwave radiation, which lowers microwave radiation energy. Figure 8 also shows that microwave radiation frequency is independent of the external axial guiding magnetic field. This is because virtual cathode oscillation primarily takes place along the z-axis, which is the same as that of the guiding magnetic field. Oscillation would not be affected by the magnetic field.

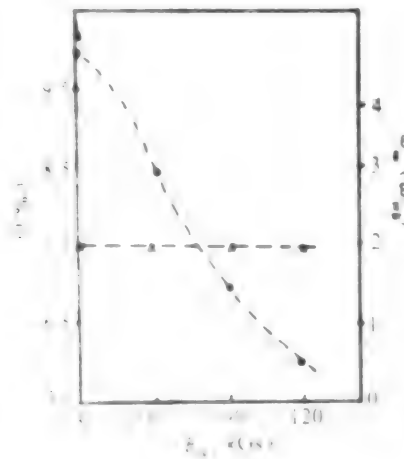


Figure 8. Relation Between Microwave Radiation Efficiency, Frequency and Guiding Magnetic Field
(● efficiency, ■ frequency)

B. Effect of Injected Electron Beam Intensity I_b

Let us use the following parameters: $R = 3.0$ cm, $L = 6.0$ cm, $r_b = 2.25$ cm, $r_{rp} = 0.047$ cm, $v_0 = 3.0$, $B_{z0} = 90$ kGs, and vary the injected electron beam intensity. Figure 9 shows that both frequency and efficiency of VIRCATOR-generated microwaves are raised with increasing intensity. A qualitative analysis of the physical mechanism of virtual cathode oscillation would reveal that this conclusion is reasonable. When an electron beam is

transported through space, the space potential is reduced because of the negative charge carried by the electrons. The larger the density of electrons, the more this potential is lowered. When the current to be transported reaches the limiting value, some electrons are reflected due to the falling potential; this forms the virtual cathode. Because of electron transport and reflection, electron density in the virtual cathode area drops. As a result, the potential rises in the area, which allows more electrons to enter the area. As more electrons are transported into the area, the potential falls again and more electrons are reflected. This process is continuously repeated to become a periodic oscillation of the virtual cathode. Hence, the higher the beam intensity compared to the limiting current, the faster the virtual cathode oscillation process repeats itself, i.e., the higher the frequency becomes. In addition, the larger I_0/I_{SCL} is, the lower the probability for electrons to penetrate the virtual cathode becomes (which was proven by simulation). This means the probability for electrons to be "captured" by the virtual cathode is higher, which also means higher efficiency for VIRCATOR-generated microwave radiation.

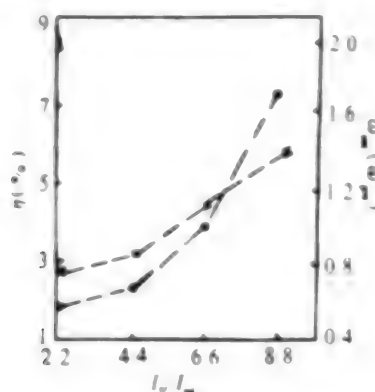


Figure 9. Relation Between Microwave Radiation Efficiency, Frequency and Beam Current
(\bullet efficiency, \times frequency)

3. Effect of Electron Beam Energy γ_0

Figure 10 shows that the microwave radiation frequency, ω_{OSC} , declines with increasing electron beam energy γ_0 . From equation (3), as γ_0 increases, I_{SCL} also rises. Hence, when I_0 is fixed, I_0/I_{SCL} decreases. Therefore, the virtual cathode oscillation process is weakened. The parameters used in this figure are identical to those used in the section above.

4. Effect of Relative Radius of Electron Beam

Microwave radiation frequency increases as relative radius, r_b/R , decreases (see Figure 11). This is probably due to equation (3) where I_0/I_{SCL} decreases as I_{SCL} increases with increasing r_b/R . Therefore, virtual cathode oscillation weakens and its associated oscillation frequency falls. However, microwave radiation efficiency exhibits a maximum at r_b/R equal to 0.55. This is a more complex problem which is dependent upon electron-beam

coupling with the waveguide. Different-size electron beams have different sensitivities to various waveguide modes. Other parameters used are the same as those in the previous example.

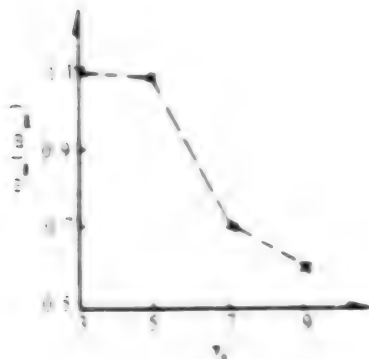


Figure 10. Relation Between Microwave Frequency and Electron Energy

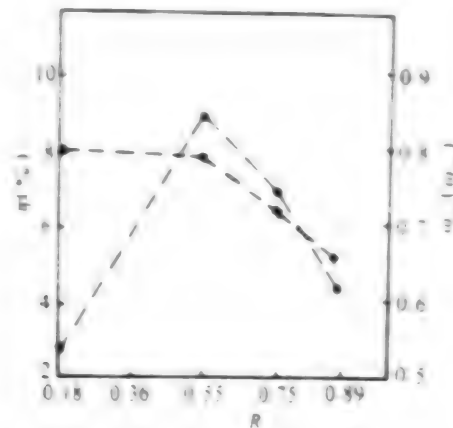


Figure 11. Relation Between Microwave Efficiency, Frequency and Beam Radius
● efficiency, x frequency)

There are other factors affecting microwave radiation, including the primary mode of excitation in the waveguide. Different parameters such as waveguide structure and electron-beam size would produce different waveguide modes. The patterns are still yet to be further investigated.

Acknowledgement

The authors wish to acknowledge Professor Cheng Kaijia [4453 7030 3946] for his guidance and assistance.

References

1. C.D. Child, PHYS. REV., Vol 32 (Ser I), 1911, p 492.
2. I. Langmuir, PHYS. REV., Vol 20, 1913, p 450.
3. C.K. Birdsall and W.B. Bridge, J. APPL. PHYS., Vol 32, No 12, 1961, p 2611.
4. W.B. Bridge and C.K. Birdsall, J. APPL. PHYS., Vol 34, No 10, 1963, p 2946.
5. T.J.T. Kwan, PHYS. FLUIDS, Vol 27, No 1, 1984, p 226.
6. T.J.T. Kwan and L.E. Thode, PHYS. FLUIDS, Vol 27, No 7, 1984, p 1570.
7. A. Kadish, R.J. Faehl and C.M. Snell, PHYS. FLUIDS, Vol 29, No 12, 1986, p 4196.

8. R.B. Miller and D.C. Straw, J. APPL. PHYS., Vol 47, 1976, p 1897.
9. L.E. Thode, B.B. Godfrey and W.R. Shanahan, PHYS. FLUIDS, Vol 22, No 4, 1979, p 747.
10. S.C. Burkhardt, R.D. Scarpelli and R.L. Lundberg, J. APPL. PHYS., Vol 58, No 1, 1985, p 28.
11. J.D. Jackson, translated by Song Peiyu [1345 1014 6276], "Classical Electrodynamics," Higher Education Publishing House, 1983, p 379.
12. J.M. Dawson, REV. OF MODERN PHYS., Vol 55, No 2, 1983.
13. E.O. Brigham, translated by Liu Qun [2692 5028], "Fast Fourier Transforms," Shanghai Science and Technology Publishing House, 1979.

Flash-II: Relativistic Electron-Beam Accelerator

92FE0092C Chengdu QIANG JIGUANG YU LIZI SHU [HIGH-POWER LASER AND PARTICLE BEAMS] in Chinese Vol 3 No 3, Aug 91 pp 340-348

[Article by Qiu Aici [6726 1947 1964], Li Yuhu [2621 3768 5406], Wang Zhiguang [3769 4249 1639], Shen Zhikang [3088 1807 1660], Zhang Yongmin [1728 3057 3046], Zeng Zhengzhong [2582 2973 0022], Zhang Jiasheng [1728 0857 3932], and Gai Tongyang [5556 0681 7122] of Northwest Institute of Nuclear Technology, P.O. Box 69, Xian 710024, PRC: "Flash-II: Relativistic Electron-Beam Accelerator"; MS received 28 Mar 91, revised 27 May 91]

[Text] Abstract

A low-impedance pulsed electron-beam accelerator, Flash-II, developed at Northwest Institute of Nuclear Technology is described. It is primarily used in nuclear radiation effects simulation. The accelerator consists of three major components--i.e., a Marx generator, a water-dielectric coaxial line and a diode--and more than a dozen pieces of auxiliary equipment. Testing and operating results at two charging voltages, i.e., ± 55 kV and ± 70 kV, are presented. The maximum output current is 600 kA and the diode voltage is 1.2 MV. This accelerator is used for electron-beam and X-ray experiments.

I. Introduction

Flash-II is a low-impedance pulsed relativistic electron-beam accelerator. The electron beam produced can be used in the study of materials destruction and structural effects, as well as in research on high-power microwave (HPM) generation and excimer laser pumping. In addition, by means of a conversion target, Bremsstrahlung can be generated to develop radioactive-ray measurement technology and to study instantaneous gamma-ray radiation effects on electronic components.

Based on its primary applications, Flash-II has to be a low-impedance, intense-current accelerator. Therefore, it was designed to have an impedance of 1 ohm. However, since it is technically difficult to build a low-impedance water-dielectric accelerator and the technology is not available in China, it was decided that the development would be completed in two phases. The impedance is 2 ohms in the first phase.^{1,2}

Flash-II is 17 m long, 6.5 m wide and 5.2 m high. A picture [photograph not reproduced] is shown in the inside back cover. Figure 1 is a schematic diagram of the entire accelerator. The accelerator consists of a Marx generator, water-dielectric coaxial line (including pulse-forming line, main switch, transmission line, pre-pulse switch, output line) and diode, as well as more than a dozen pieces of auxiliary equipment such as a 180-ton oil filtering facility, 15-ton water purifying device, ± 120 -kV high-voltage dc power supply, 1.8-T pulsed magnetic field system, triggers, controls, etc. Figure 2 shows the equivalent circuit diagram of Flash-II. Based on output requirements, electrical parameters can be calculated. Our computations show that the maximum energy storage capacity is 224 kJ and the maximum nominal voltage is 6.4 MV. At a 2-ohm impedance, the overall energy transfer efficiency is 30 percent and the voltage transfer efficiency is 20 percent.

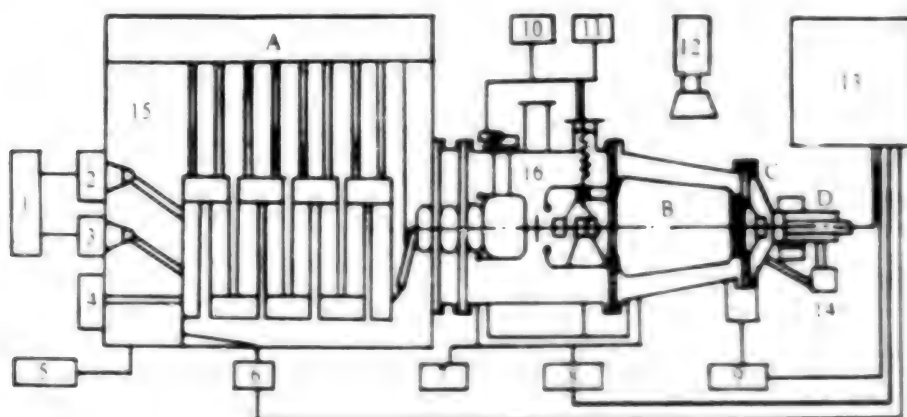


Figure 1. Flash-II Accelerator System

(A) Marx generator; (B) Water-dielectric coaxial line; (C) Diode;
(D) Pulse magnetic field and drift room ($B = 1.8$ T)

1. Control system; 2. Trigger; 3. H.V. power supply; 4. SF₆ filling and venting installation; 5. Oil filtering system (180t); 6. Im monitor; 7. Water purifying system (15t); 8. U_p, U_T, U_{O1} monitor; 9. I_p, U_{O2} monitor; 10. Hydraulic actuator; 11. SF₆ filling tank; 12. Industry T.V.; 13. 120 kV shield room; 14. Vacuum system; 15. Oil; 16. Water

II. Marx Generator

The Marx generator has 64 capacitors connected in S shape in eight rows. Each row contains eight 100-kV, 0.7- μ F capacitors and four 3-electrode air-spark switches with triggering disks in the middle. It is suspended over the oil tank by two 160-cm-long nylon lines. Figure 3 shows this capacitor configuration in a single row. The insulation distance between capacitors is 8 cm within the same row, the distance between rows is 30 cm, and the minimum distance to ground is 90 cm. The first three switches in the first row are triggered by a TG-125 trigger. The rest are triggered by intercalation of a grounded resistor.

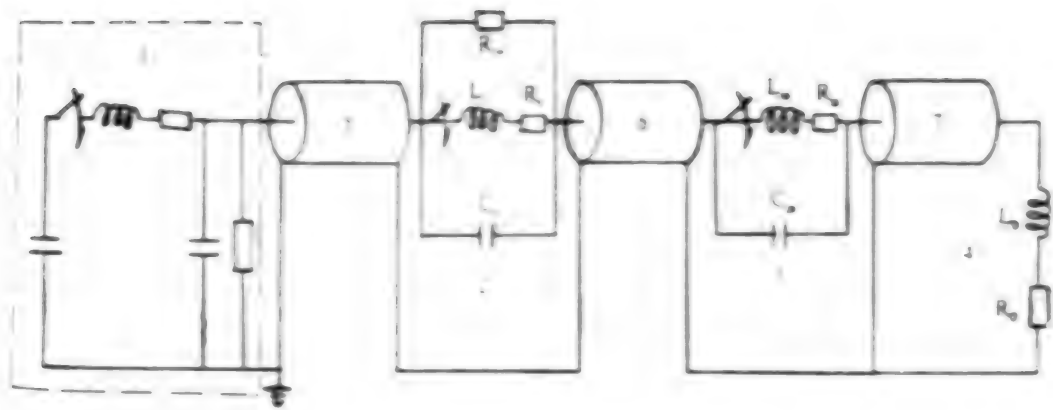
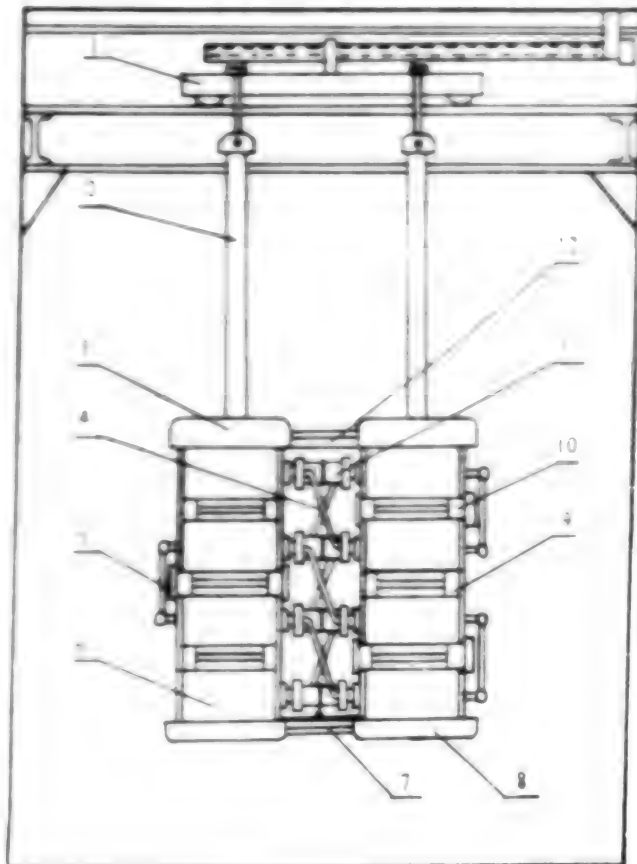


Figure 2. Electrical Model of Flash-II

1. Marx generator; 2. Output switch; 3. Pre-pulse switch; 4. Diode;
 5. $R_p = 5.0\Omega$ $T_p = 40$ ns; 6. $L_p = 1.25$ $T_p = 40$ ns; 7. $Z_1 = 1.0\Omega$
 $T_1 = 60$ ns



1. Travel machinery
2. Insulated straps
3. Upper shield covers
4. Charge resistors
5. Grounding resistors
6. Capacitors
7. Trigger resistors
8. Lower shield covers
9. Metal spacers
10. Insulation spacers
11. Spark switches
12. Insulation connect plates

Figure 3. Configuration of Single Row of Capacitors in Marx Generator

Table 1 shows the measured equivalent parameters based on the short-circuited current waveform of the generator and the charging voltage waveform. At a dc charging voltage of ± 70 kV, 120 pulses were continuously generated. Self-discharge occurred 3.3 percent of the time. The buildup time is 419 ns and the jitter is 60 ns.

Table 1. Marx Generator Equivalent Parameters

Generator parameters	Measured value	Designed value
Series inductance L_m	11.7 μH	12 μH
Buildup or capacity C_m	11.25 nF	11 nF
Resistance in series R_m	3.0 Ω	4.0 Ω
Parallel resistance R_p	0.58 k Ω	1.9 k Ω
Stray capacitance vs ground C_j	0.2 nF	<0.64 nF

III. Water-Dielectric Coaxial Line

The water-dielectric coaxial line includes the pulse-forming line, main switch, transmission line, pre-pulse switch and output line. Deionized water is used as the insulating dielectric. Two pieces of 220-diameter insulating plates are placed between the water-dielectric coaxial line and Marx generator to separate water from oil. Figure 4 shows the radial electric field at the water-oil interface. The electric field at the intersection of metal, water and insulating plate is less than 30 kV/cm, while the maximum field is 125 kV/cm. The pulse-forming line has an impedance of 5 ohms. The diameter of the outer conductor is 186 cm and that of the inner conductor is 88 cm; its length is 184 cm. The maximum operating voltage of the pulse-forming line is \sim MV. The ratio of operating field strength between outer and inner conductor to the breakdown field strength is 0.49.

The transmission-line impedance is 3.2 ohms. Its inner-conductor diameter is 113.6 cm and its length is 134 cm. A pre-pulse suppression inductor is installed between inner and outer conductor. It not only lowers pre-pulse voltage and operating voltage of the pre-pulse switch, but also brings the hydraulic line, control circuit and pneumatic line to control the main switch distance into the inner conductor of transmission line to ensure electrical safety. The output line has an impedance of 2 ohms and is 200 cm long. The outer conductor is tapered from 186 cm to 114 cm.

The main switch is a water-dielectric field-distortion switch. The pre-pulse switch consists of two SF₆-filled switches in parallel. They are secured on a 10-cm-thick Plexiglass plate. This 10-cm-thick Plexiglass plate is used to support the inner cylinders of the transmission line and output line. A 100-ohm resistor serves as the load for the water-dielectric switch to simulate the operating conditions of the main switch and

pre-pulse switch. When the main switch is automatically triggered, the trigger disk position is the main factor affecting switching. At $N = 7$, 5 ~ 6 channels were formed based on discharge photos taken. Theoretical forming-line waveform is found to agree with that measured. When the switching distance is 135 mm, the equivalent inductance and resistance of the sparking channel are 120 nH and 0.5 ohm, respectively. Presently, because the inductance selected for the trigger circuit is not large enough, the output waveform is less than ideal; it is expected to improve after inductance is raised.³ In the automatic breakdown mode, switching distance is the primary factor affecting the main switch. In this case, the breakdown field is relatively high (approximately 250 kV/cm). However, it can only form 1-2 channels. When the distance is 135 mm, the equivalent inductance and resistance of the switch are 300 nH and 0.5 ohm, respectively, when the switch is turned on. The behavior of the pre-pulse switch has a major impact on the output voltage. Higher voltage transfer efficiency can be obtained by choosing a suitable gas pressure to steepen up the output pulse.

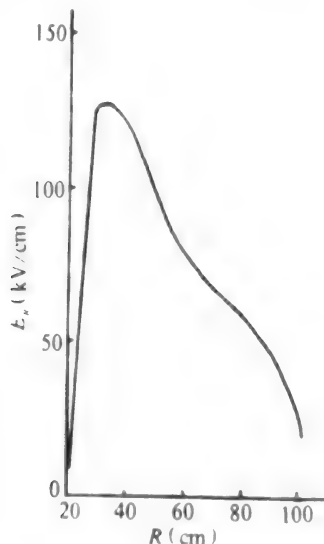


Figure 4. Radial Electric Field Distribution at Interface of Oil-Water Diaphragm

Major output parameters of the accelerator are listed in Table 2 under conditions that the dc charging voltage is ± 60 kV, main switch gap is 145 mm and pre-pulse switch pressure is 0.35 MPa.

Under the load of the diode, when the dc charging voltage is ± 70 kV and main switch gap is 151 mm, statistical analysis involving dozens of runs shows that the breakdown voltage of the main switch is 3739 kV \pm 5 percent, breakdown time is 692 ns, jitter is 29 ns, and pre-pulse switch breakdown time jitter is 67.5 ns. Figure 5 shows the pulse-forming-line (upper) and transmission-line (lower) voltage waveforms measured. Figure 6 shows the output-line waveforms (upper = pre-pulse, lower = main pulse).

Table 2. Accelerator Parameters With Dummy Load

d.c. charge voltage	U_s	$\pm 60\text{kV}$
breakdown time of main switch	t_m	700ns
output line voltage	U_{out}	969kV
rise time of output line voltage	t_{out}	42ns
steepening of output pulse	t_s, t_{tr}	58%
ratio of prepulse and main pulse voltage		1
half width of output pulse	T_{OH}	88ns
total voltage transmission efficiency G_v		25.2%
total energy transmission efficiency G_e		34.7%

t_{tr} , rise time of transmission line voltage.

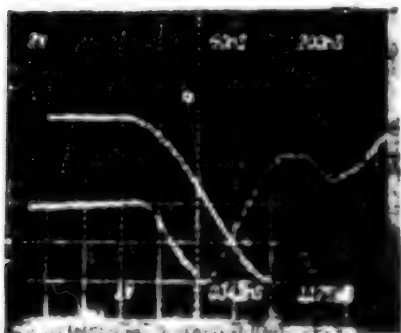


Figure 5. Forming-Line Voltage (upper)
Transmission-Line Voltage (lower)

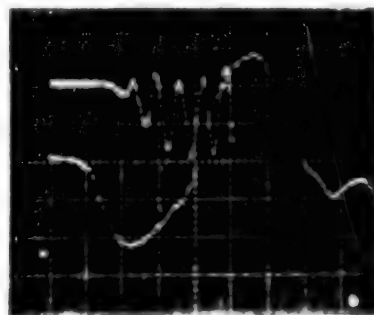


Figure 6. Output-Line Pre-pulse
(upper) and Main Pulse (lower)

IV. Low-Impedance Diode and Its Output Characteristics

The structure of the diode is shown in Figure 7. It includes a radial insulation Plexiglass diaphragm, double-cone vacuum line, and coaxial cathode shank and anode area. The radial field at the two triple joint points is less than 20 kV/cm and the insulation gap is 40 cm. The mean radial electric field is 37 kV/cm. The angle between the electrode and the diaphragm is 8° at the anode and 76° at the cathode. Insulation in the vacuum area was designed to meet ceramic insulation conditions. Furthermore, the field strength is held at below 350 kV/cm at the surface of the anode shank. The cathode of the diode is a 220-mm-diameter graphite plate and the anode is an aluminum-plated foil (1 μm Al + 12 μm PET). In order to meet energy-flux and beam-uniformity requirements, an axial pulse magnetic field is added and the drift tube is filled with a low-pressure gas (133-266 Pa).⁴ The pulse magnetic field is created by a system comprised of a 10-kV, 180-kJ pulsed power supply, magnetic field coil and drift tube. At a charging voltage of 7 kV, the peak magnetization intensity generated is 1.8 T.⁵ Synchronization of magnetic field and accelerator is achieved by using the dB/dt signal generated by the magnetic field to trigger the Marx generator. The rise time of the magnetic field pulse is 8.4 ms, and the accelerator takes 1.77 μs to shoot out an electron beam. Under normal operating conditions, the two can be reliably

synchronized so that the electron beam arrives when the magnetic field is at its maximum. A statistical analysis of 115 runs shows that synchronization is 96 percent effective.

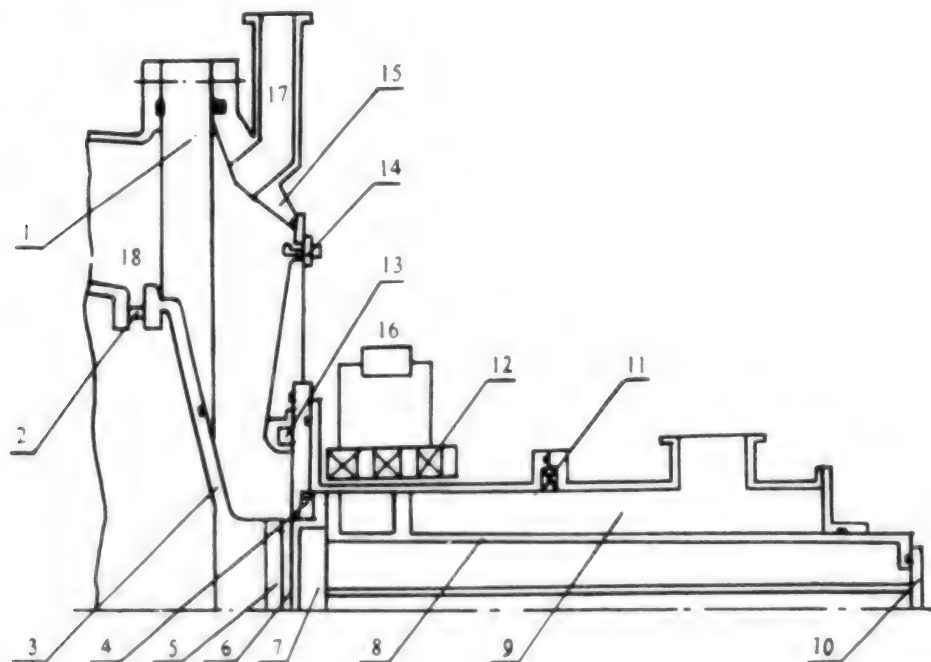


Figure 7. Diode Configuration

1. Insulation diaphragm; 2. Electric contacts; 3. Cathode shank;
4. Press foil machinery; 5. Cathode; 6. Anode foil; 7. Target;
8. Target support; 9. Drift region; 10. Signal output;
11. Rogowski coil; 12. Magnetic field coil; 13. Rogowski coil;
14. B probe; 15. Anode flange; 16. Water; 17. Vacuum; 18. Power supply

Table 3 shows the diode output parameters at different charging voltages. The parameters reported at ± 55 kV and ± 70 kV are statistical results after 30 and 59 runs, respectively. Those presented for charging voltages ± 80 kV and 85 kV are results of 90249 and 90250 runs, respectively. The length-to-width ratio (i.e., cathode radius to anode-cathode distance ratio) has a significant effect on its output parameters. When the ratio is 14.7 and charging voltage is ± 70 kV, the diode current reached as high as 606 kA at 1.1 MV. Diodes using a graphite cathode have a shorter startup time (i.e., lag time between diode current and voltage) than those using a stainless cathode. Statistically, startup time is 1.2 ns \pm 4.7 ns after several dozen runs.

Table 3. Measured Diode Parameters for Different Voltage Levels

charge voltage	U_c (kV)	± 55	± 70	± 80	± 85
main switch distance	S_a (mm)	120	151	161	171
prepulse switch gas-pressure	P_p (MPa)	0.3	0.42	0.46	0.48
cathode radius	R_c (mm)	90	110	110	110
A - K gap	d_{AK} (mm)	11 ~ 12	8 ~ 8.5	8.1	8.1
diode voltage	U_d (kV)	$936 \pm 5.8\%$	$1072 \pm 6.8\%$	1302	1638
gap voltage	U_g (kV)	$903 \pm 6.7\%$	$902 \pm 9.8\%$	1113	1529
diode current	I_d (kA)	$196 \pm 8.2\%$	$466 \pm 6\%$	589	511
total beam energy	E_b (kJ)	11	$32.5 \pm 21\%$	52.2	66
diode impedance	R_d (Ω)	5.1	$2.1 \pm 10.9\%$	2.1	3.1

Diode current parameters are measured with two Rogowski coils and a B probe. As shown in Figure 7, they are installed between cathode and anode in the coaxial region and the double-cone region to measure the current reaching the anode as a function of time. The integrated B-probe signal is the overall current of the diode. A differential capacitor divider at the end of the output line is used to measure the diode voltage. Three signals are time-correlated and then recorded on a digital oscilloscope. Voltage across the anode and cathode of the diode, $U_k = U_D - LdI/dt$ where L is the inductance of the diode (approximately 36 nH), can be calculated by a computer by a short-circuit method. Subsequently, it is possible to obtain output power, impedance curve, electron energy spectrum, total beam energy, and mean electron energy. Typical single-run parameters are shown in Figures 8, 9 and 10.

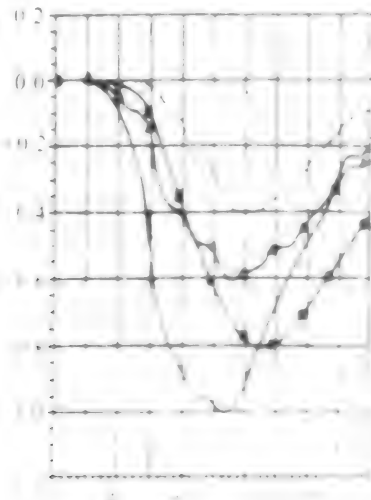


Figure 8. Current and voltage waveforms versus time for different voltage levels.

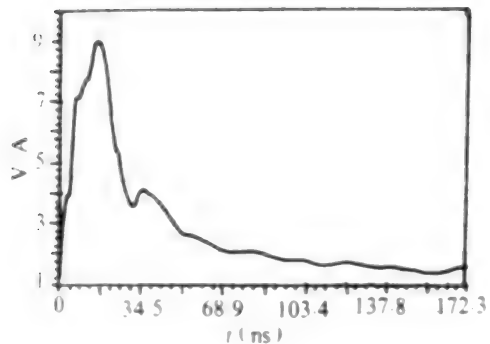


Figure 9. Diode Impedance
(90249 runs)

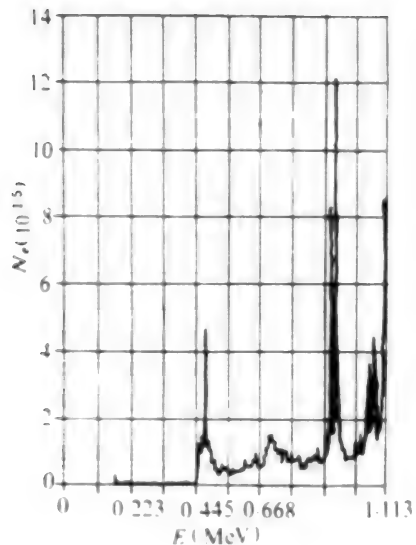


Figure 10. Electron Spectrum
Mean electron energy 8.52×10^5 eV
Total beam energy 3.25×10^{23} eV

After penetrating the thin foil anode, the electron beam enters the drift tube. The beam parameters are dependent upon factors such as state of the diode, cathode size, magnitude of the magnetic field, pressure inside the drift tube, and transport distance. Under conditions of ± 70 kV charging voltage, 1.8 T magnetization at the center of the magnetic field, 220 mm cathode diameter and 146-186 Pa drift-tube pressure, preliminary measurements of beam current parameters were made. Electron-beam waveform and charge transfer efficiency were measured with a Faraday cup.⁶ Figure 11 shows the beam waveform obtained 24 cm away from the anode with a 0.12-mm-thick aluminum foil absorber. The peak current is 408 kA and the half width is 89 ns. The overall energy of the electron beam is measured with a graphite calorimeter.⁷ At 17.5-24 cm away from the anode, the beam energy is 18-28 kJ (corresponding to 30.5 kJ of average overall diode energy). The diameter of the electron beam ranges from 120 to 147 mm. The uniformity of the electron beam was measured with a graphite calorimeter array, Faraday-cup array and pinhole camera. Within a 118-mm-diameter cross section, the uniformity is 80 per cent.⁸

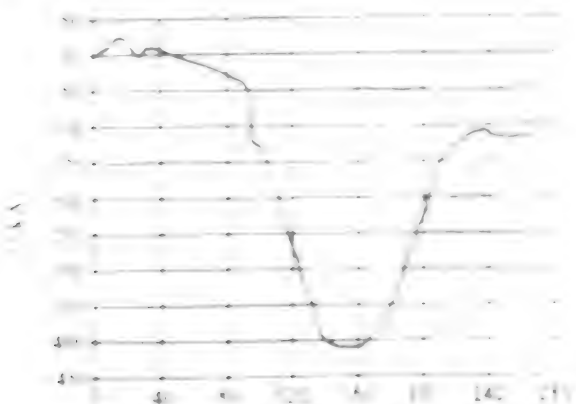


Figure 11. F.C. Current

X-rays are produced when an electron beam is brought out by a 30- μ m Ti foil to bombard a tungsten target, creating Bremsstrahlung. At this time, the equivalent impedance of the diode is approximately 2-2.5 times that of the output line. At a charging voltage of ± 55 kV, the X-ray radiation 23 cm away from the target was measured by a lithium-fluoride exothermic dosimeter to be $3.5 \times 10^{-2} \pm 0.56$ C/kg. Using a photo-tube, the half width of the X-ray tube was measured to be 50 ns at 7×10^5 C/kg·s.

V. Conclusions

Flash-II was fired over 100 times at ± 55 kV and ± 70 kV. When certain conditions and parameters were controlled well, the accelerator could operate in a stable manner. Output voltage and peak current had better than 90 percent reproducibility. The reproducibility for total beam energy is 79 percent. Further improvement is necessary. Beam current parameters were measured on a preliminary basis. Measurement techniques need to be perfected, and accuracy improved. Because of an urgency to use the accelerator in certain experiments, no attempts have been made to continue testing at higher voltages beyond ± 85 kV. The charging voltage will be raised in the future and efforts will be made to achieve design objectives for phase two.

During the accelerator development phase, guidance was provided by Lu Min [0712 2404], Ye Lirun [0673 4539 3387], Qiao Dengjiang [0829 4098 3068], and Huang Bao [7806 6283]; support was given from different levels of leadership; and cooperation was offered by many other organizations. More than 30 people were involved at one point or another and some have left the institute. They worked diligently toward the development of the accelerator. The authors wish to express their gratitude to all those people and organizations who supported and participated in this effort.

References

1. Qiu Aici, "Proof of Feasibility of REB Accelerator," Internal Information, January 1982.
2. Qiu Aici et al., "Technical Design Scheme for REB Accelerator," Internal Information, June 1983.
3. Han Xiaofan [7281 1420 5571] and Qiu Aici, "Theoretical Simulation of REB Accelerator Field-Distortion Switch," Proceedings of the Fourth National High-Power Particle Beam Conference, November 1990.
4. Qiu Aici and Liu Guozhi [0491 0948 3112], "Feasibility of Using an Applied Magnetic Field to Control Homogeneity of Electron Beam Energy," Internal Information, November 1986.
5. Liu Guozhi, Qiu Aici and Su Jiankang [5685 1696 0211], "Development of Pulse Magnet Field Device to Control Energy Flux and Uniformity of Intense Relativistic Electron Beam," Proceedings of the Fourth National High-Power Particle Beam Conference, November 1990.

6. Cheng Zhigang [4453 0037 0474], "Development of Faraday Cup To Measure Intense Beam Current," Proceedings of the Fourth National High-Power Particle Beam Conference, November 1990.
7. Fan Yajun [2753 0068 6511], "Experimental Study of Total Absorption Graphite Calorimeter for Measurement of REB Electron Beam Energy," Proceedings of the Fourth National High-Power Particle Beam Conference, November 1990.
8. Rao Junhong [7435 0193 7703], "Development of Faraday Cup To Measure Intense Beam Current," Proceedings of the Fourth National High-Power Particle Beam Conference, November 1990.

LASERS, SENSORS, OPTICS

Satellite-Borne Remote Sensing System With CCD Camera, Data Transmission Link

92FE0001A Beijing ZHONGGUO KONGJIAN KEXUE JISHU [CHINESE SPACE SCIENCE AND TECHNOLOGY] in Chinese Vol 11 No 2, Apr 91 pp 1-7

[Article by Wang Mingyuan [3769 2494 6678] and Lin Kexiang [2651 0668 4382] of Xian Institute of Space Radio Technology: "Satellite-Borne Remote Sensing System With CCD Camera and Data Transmission"; MS received 14 Apr 90]

[Text] Abstract

A CCD camera remote sensing and data transmission system was successfully flight-tested in October 1986. High-quality preprocessed panchromatic and multispectral false-color photos were obtained. The design, construction, characteristics, technical specifications, operating principle, and hardware development of the system are introduced. The test flight and the results are described and analyzed.

I. Introduction

The advent of the observation satellite with transmission link provides a more effective means for real-time observation of the earth. This type of remote sensing satellite has a large coverage area, capable of covering the entire globe. It has excellent capability to monitor dynamic changes by repeated observation of the same area. It is capable of monitoring around-the-clock in any kind of weather and of obtaining information in a timely manner. It has a reasonable lifetime, and brings considerable social and economic benefits. To this end, satellite remote sensing technology was developed in the 1970's and 1980's in countries such as the United States, the Soviet Union, and France. Furthermore, Japan, the European Space Agency, India, and Brazil are also actively developing transmission observation satellites. China is a huge country, and needs remote sensing photos for survey of resources, geological survey, agriculture, forestry and water resource planning, environmental monitoring, oceanic development, and weather observation. Therefore, we must develop satellite telemetry techniques to satisfy the needs for satellite remote sensing photos. The CCD-camera remote sensing system with data transmission link described here serves as a foundation in the development of earth observation satellites.

II. Design Specifications

1. Orbit Parameters

The satellite follows a near-circular sun-synchronous orbit in order to ensure that pictures are taken at essentially the same solar altitude angle. The orbit parameters are as follows:

orbit altitude $H = 400$ km;
orbital angle of inclination $i = 96.4^\circ$;
satellite period $T = 92.4$ min;
subsatellite-point velocity $v_g = 7.219$ km/s.

2. Technical Specifications of the CCD Camera

The CCD camera uses the same lens for panchromatic and multispectral pictures. The same camera can simultaneously take panchromatic and multispectral photos of objects on earth. The panchromatic picture takes one band and the multispectral pictures take three bands. Each band employs three 2048-element CCD143A devices for optoelectronic conversion. In the multispectral mode, two elements are used as one. The parameters of the CCD panchromatic and multispectral camera are as follows:

camera focal length $F = 400$ mm;
relative aperture $D/F = 1/4$;
field-of-view angle $2\omega = 11.5^\circ$;
panchromatic band (P_a) $0.5\text{--}0.75 \mu\text{m}$;
multispectral band (B_1) $0.5\text{--}0.6 \mu\text{m}$, (B_2) $0.6\text{--}0.7 \mu\text{m}$, (B_3) $0.8\text{--}0.9 \mu\text{m}$;
total number of pixels $N = 3 \times 2048$ elements;
pixel size $d^2 = 13 \mu\text{m} \times 13 \mu\text{m}$;
ground pixel resolution $\Delta R = 13 \text{ m (Pa)}$,
 $\Delta R = 26 \text{ m (B}_1, B_2, B_3)$;
ground scan (swath) width $L = 80 \text{ km}$;
optoelectronic integration time $t_{in} = 1.8 \text{ ms (Pa)}$,
 $t_{in} = 3.6 \text{ ms (B}_1, B_2, B_3)$;
video bandwidth $B = 1.8 \text{ MHz (Pa)}$,
 $B = 1.5 \text{ MHz (B}_1, B_2, B_3)$;
sampling rate $f_B = 3.6 \text{ MHz (Pa)}$,
 $f_B = 3.0 \text{ MHz (B}_1, B_2, B_3)$.

3. Data Transmission Parameters

modulation: panchromatic 2-bit PCM, multispectral 6-bit PCM
code rate: $R = 16 \text{ kbit/s}$
modulation: QPSK quadrature phase-shift keying
carrier frequency: $f_c = 4037 \pm 3 \text{ MHz}$
transmitter power: $P_t = 15 \text{ W}$
link margin: error rate: $P_e = 10^{-3}$ when $P_e/N_0 = 4.7 \text{ dBHz}$

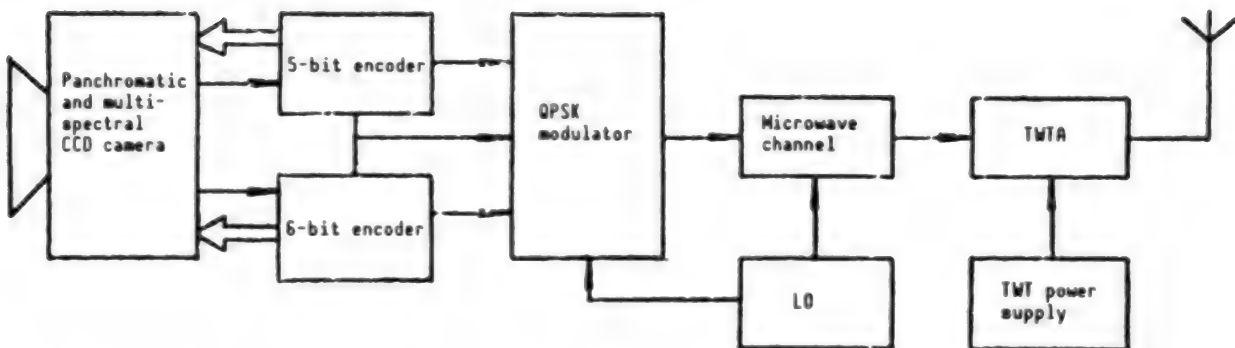


Figure 1. Satellite-Borne CCD Remote Sensing Data Transmission System

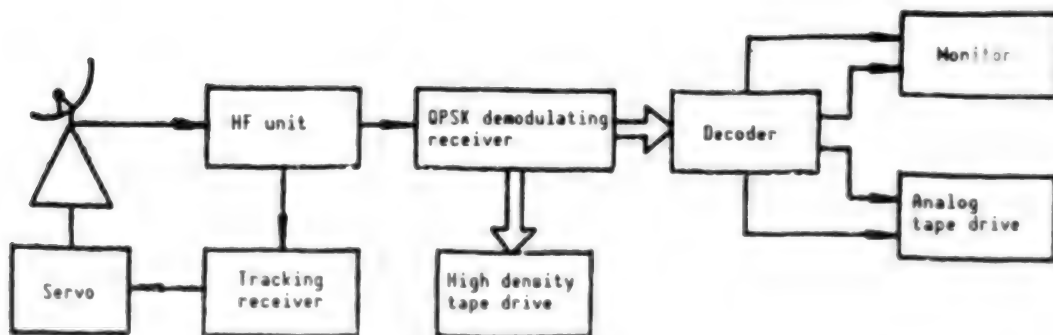


Figure 2. Block Diagram of the Ground Detection System

III. Composition of the CCD Remote Sensing Data Transmission System

The CCD remote sensing data transmission system consists of satellite-borne remote sensing data transmission equipment and ground detection equipment. The satellite-borne part includes a CCD camera, encoder, QPSK modulator, local oscillator (LO), microwave channel, traveling-wave-tube amplifier (TWT), traveling-wave-tube (TWT) power supply, and transmission antenna. Figure 1 is a block diagram of the satellite-borne equipment.

The ground equipment includes the reception antenna, high-frequency (HF) box, intermediate-frequency (IF) QPSK demodulation receiver, high-density tape drive, decoder, analog tape drive, monitor, and analog video signal source. Figure 2 is a block diagram of the ground equipment.

IV. Design of Subsystem and Hardware Development

As a whole, satellite-borne and ground-based, the CCD remote sensing data transmission system can be divided into five subsystems, i.e., the panchromatic and multispectral CCD camera, PCM coding and decoding, the QPSK modulation and demodulation receiver, the microwave channel between satellite and ground and the video terminal. They are described as follows:

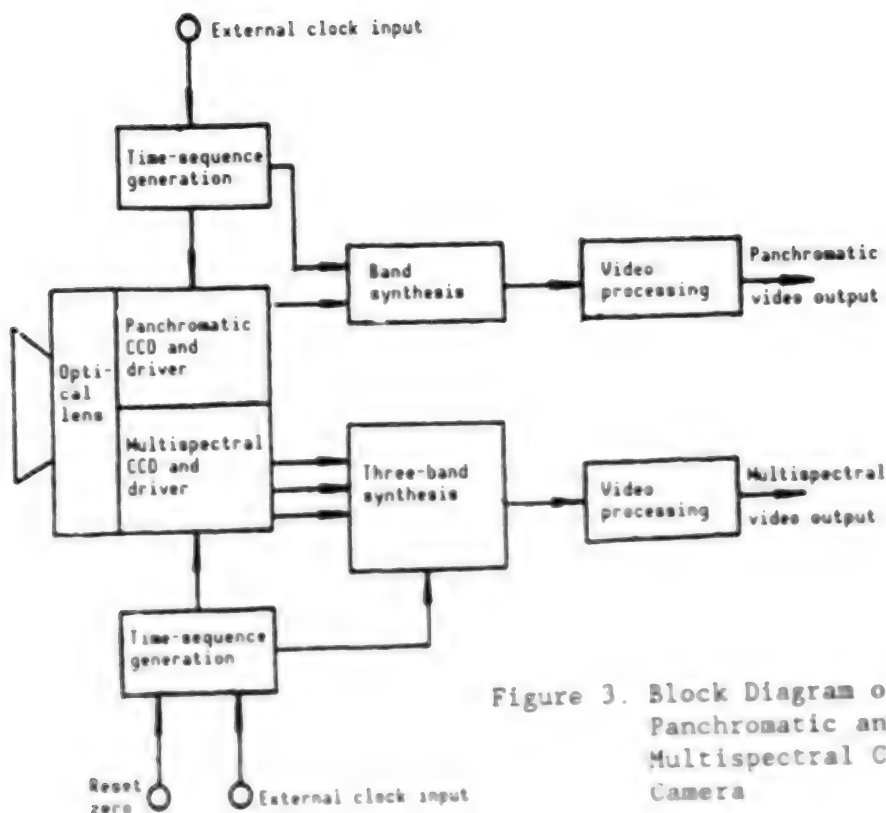


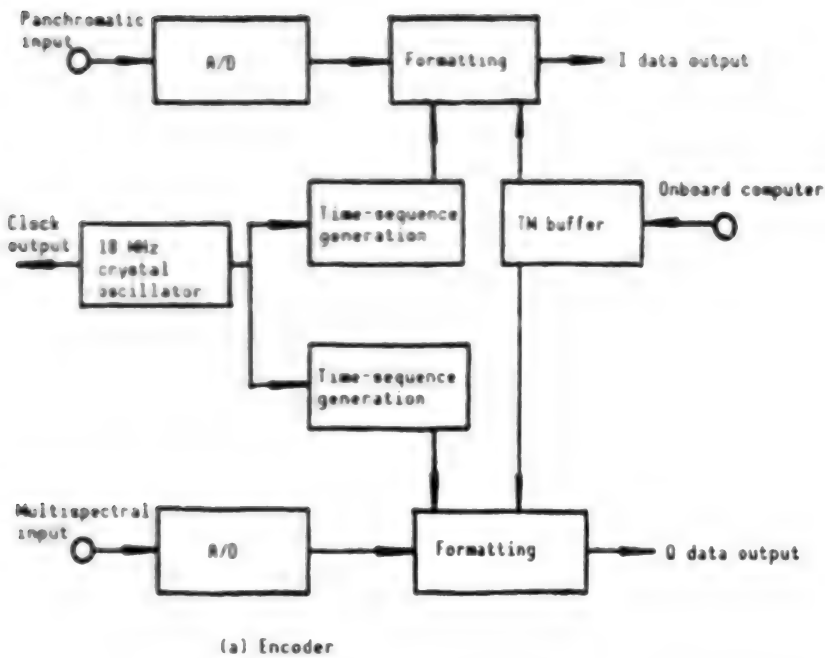
Figure 3. Block Diagram of the Panchromatic and Multispectral CCD Camera

1. Panchromatic and Multispectral CCD Camera

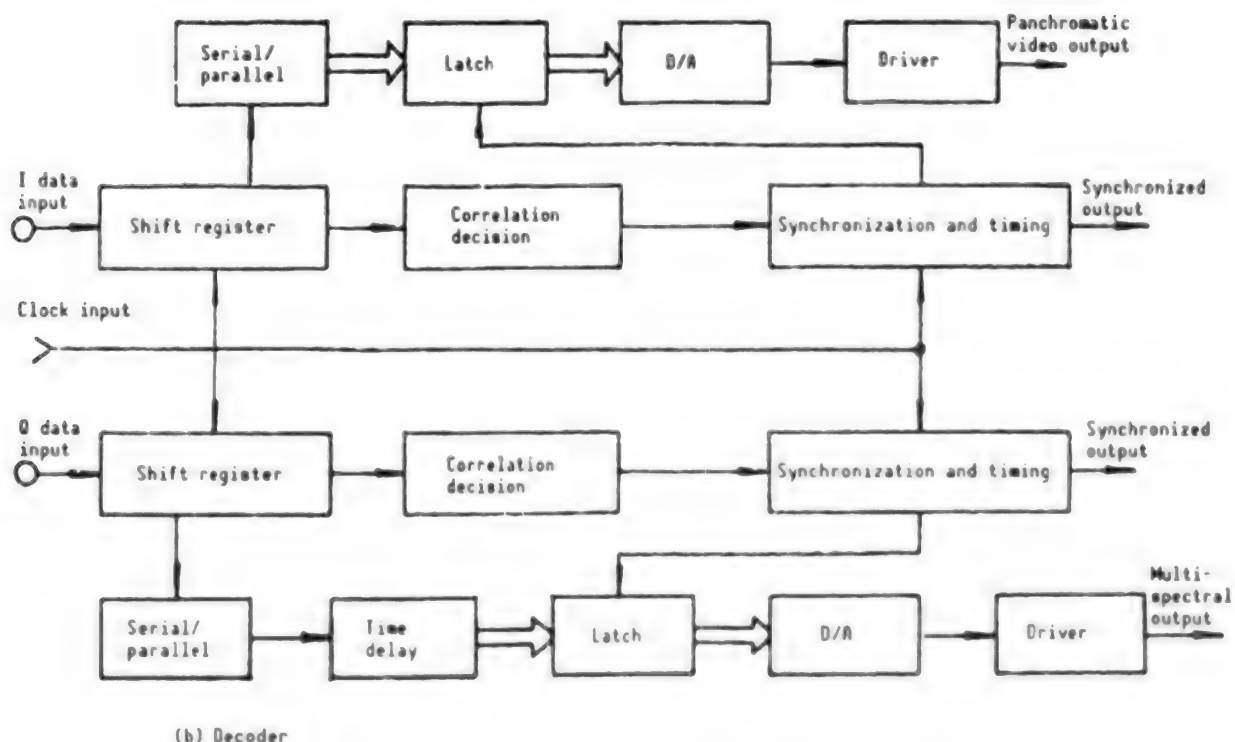
The CCD camera uses a single lens for taking both panchromatic and multispectral photos simultaneously. There is one panchromatic band and three multispectral bands. CCD143A photosensitive receivers manufactured by the U.S. company Fairchild are used. Each CCD has 2048 elements. The pixel size is $11.2\mu\text{m} \times 13\mu\text{m}$. Each band uses three CCDs and they are optically connected into an array by using semireflective prisms. In order to make the scan width equal ($11.2\mu\text{m}$) for both panchromatic and multispectral photos, two multispectral elements are used as one element. The pixel resolutions for the panchromatic camera and multispectral camera are 11 m and 16 m , respectively. The CCD camera is primarily composed of an optical lens, splitting and splicing prism, CCD and its driving circuit, time-sequence generator, and video signal processing circuit. A block diagram of the operative principle of the CCD camera is shown in Figure 3.

2. PCM Coding and Encoding

The encoder is comprised of a satellite-borne encoder and a ground-based encoder. The satellite-borne encoder includes a panchromatic encoder and a multispectral encoder. The primary function of the encoder is to perform A/D and digital-digital conversion from the video signal sent from the CCD camera and a digital signal. It then processes the remote sensing data, synchronization, coding code and self-test signal to create two data streams, I [in-phase, 400 Hz quadrature]. In addition, the encoder also generates an 18-MHz clock signal and maintains a unified clock and a variety of timing sequences to synchronize the operation of the entire remote sensing data transmission system.



(a) Encoder



(b) Decoder

Figure 4. Block Diagram of the Encoder/Decoder Subsystem

The decoder synchronously decodes the I and Q data streams from the QPSK demodulator and restores the analog signals for the panchromatic and multispectral photos. Moreover, it provides a variety of synchronization pulses for video terminals and recorders such as monitors and analog tape drives.

Figure 4 is a block diagram of the encoding and decoding subsystem.

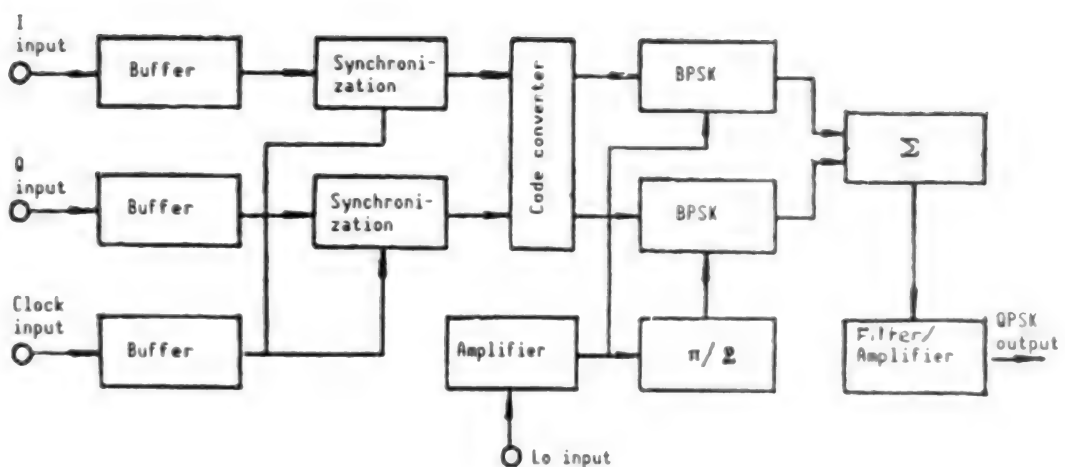


Figure 5. Block Diagram of the QPSK Modulator

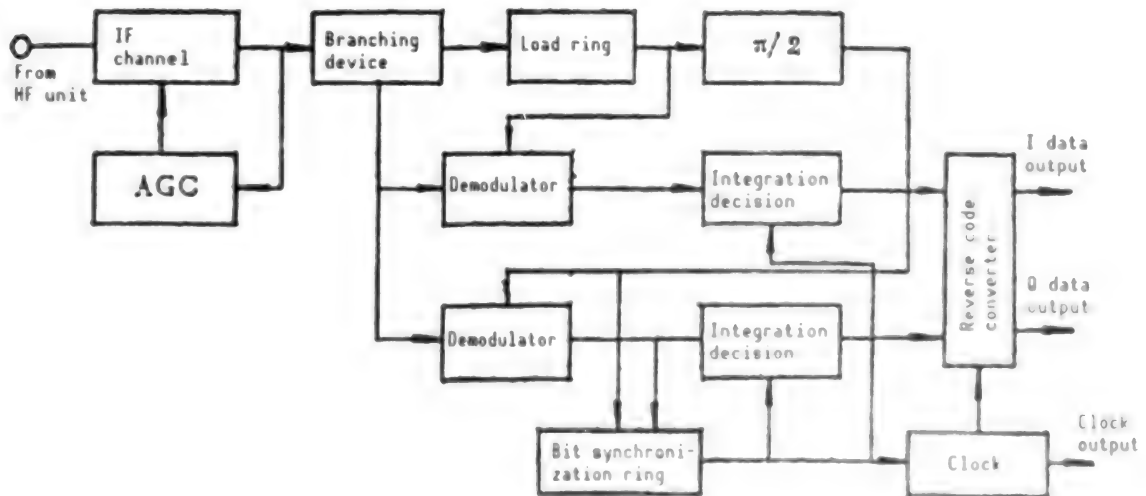


Figure 6. Block Diagram of the QPSK Coherent Demodulation Receiver

3. QPSK Modulation and Demodulation

The QPSK modulator orthogonally modulates the two 18 Mbit/s data streams I and Q from the encoder to the unified 177.3 MHz carrier wave in order to compress the transmission bandwidth by one-half. The overall transmission rate is 36 Mbit/s. In order to overcome phase blur during demodulation on the ground, an absolute/relative code transformation is done prior to modulation. In the circuit design of the modulator, an emitter coupled logic [ECL] exclusive OR gate is used instead of a common ring modulator which significantly simplifies the hardware. Figure 5 shows a block diagram of the onward QPSK modulator.

The QPSK coherent demodulator receives the 125 ± 20 MHz modulated IF signal from the HF unit and demodulates it by coherent detection. Because a signal with frequency and phase identical to those of the received carrier wave is required for demodulation, this demodulator employs a primary local oscillator

the reference carrier wave. The reference carrier wave thus obtained is sent to the demodulator for coherent demodulation. The demodulator outputs a data stream to the synchronous access circuit and the integration-decision circuit. Then, the converter restores video and clock signals in data streams I and Q. These signals are recorded by a high-density tape drive and processed by the decoder. The operating principle of the QPSK coherent demodulation receiver is shown in Figure 6.

4. Satellite/Earth Microwave Channel

The satellite/earth microwave channel includes an onboard microwave channel and a ground HF unit. The onboard microwave channel consists of a frequency up-converter, LO, filter, TWTA, TWT power supply, and transmitting antenna. The ground HF unit is comprised of a low-noise FET amplifier (LNA), frequency down-converter, image filter, dielectric oscillator, preamplifier, and middle-stage amplifier. The operating principle of the satellite-to-ground microwave channel is shown in Figure 7.

5. Video Terminal Subsystem

The video terminal subsystem is comprised of monitors, analog and digital tape drives, and video analog signal sources. The main function of the video terminal subsystem is to record and monitor images captured from remote sensing. The monitor has a geometric resolution of 2200 TVL [television lines], eight gray levels, and a nonlinear distortion of less than 3 percent. There are two kinds of tape drives: One is a high-density digital tape (HDDT) drive which records graphic data of panchromatic and multispectral pictures to be transmitted to a computer for further processing to obtain high-quality panchromatic and multispectral remote sensing photos. The other is an analog tape drive. Video analog signal sources are used as test signal sources in onboard encoders and ground monitors.

V. Results and Analysis of Flight Test of the CCD Remote Sensing Data Transmission System

Figure 8 shows the airborne and ground-station equipment used in the flight test.

The entire CCD remote sensing data transmission system was tested in flight. The overall airborne and ground-based system was proven to meet design requirements after six test flights. A large number of black-and-white photos and some multispectral photos were obtained. Target pictures were obtained after playing the HDDT back and preprocessing the signal. The panchromatic resolution goes down to the seventh black-and-white strip group and corresponds to a geometric resolution of 0.45 m; this is approximately twice that of the theoretical pixel resolution. The resolution of the multispectral photos can get down to the fifth stripe group, which corresponds to a geometric resolution of 0.63 m; this is approximately 1.5 times that of its theoretical pixel size. Its radiation resolution has essentially met the design objectives. During these test flights, real-time color temperature and illumination tests were also performed. Pictures obtained were used to study

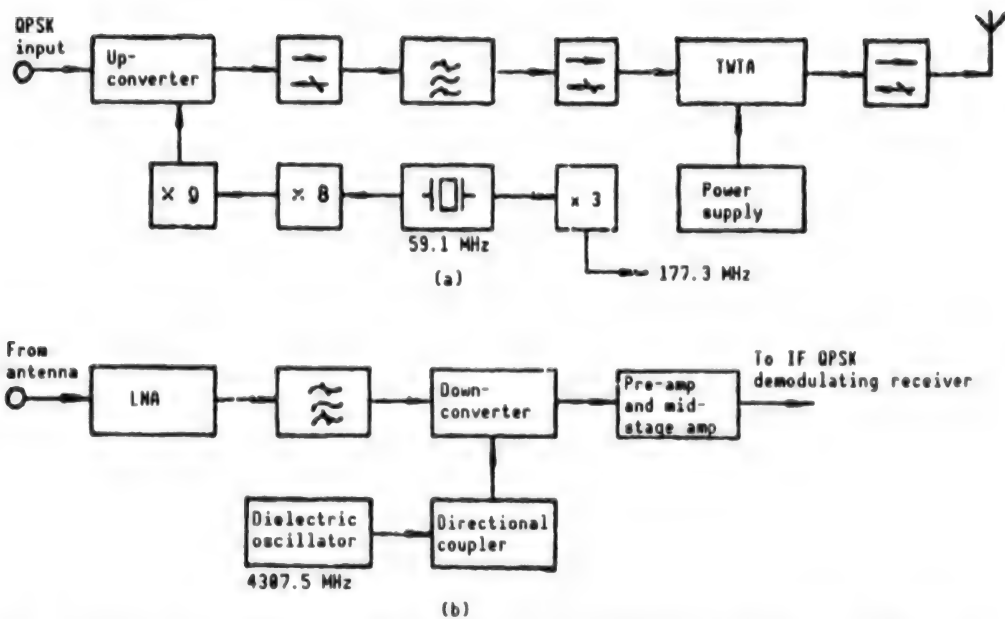


Figure 7. Block Diagram of the Satellite-To-Earth Microwave Channel

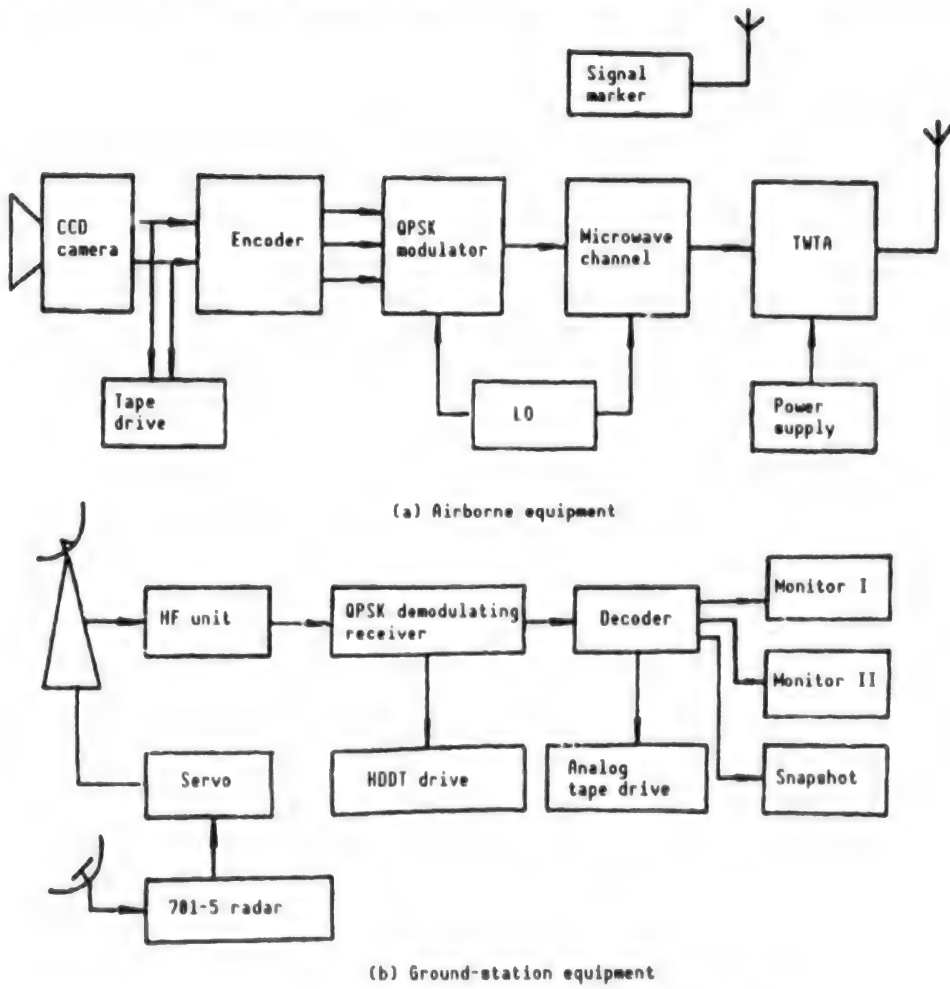


Figure 8. Block Diagram of Flight-Test Equipment

the spectral response and dynamic range. This served as a basis for development of the CCD camera system.

In addition special experiments were done to test the performance of the data transmission system. Based on calculation, good pictures can still be received even when the intensity of the signal varies by as much as 24 dB. This indicates that the receiver has an excellent automatic gain control (AGC). Furthermore, error characteristics of the data transmission system were tested. The results showed that the overall error rate is less than 10^{-6} during normal reception. It is consistent with the design requirement.

References

1. Ferrel, G.S., "Introduction to Communication Systems," Addison-Wesley, 1982.
2. Lin Kexiang and Wang Mingyuan, "Analysis and Experimental Study of Pseudo-Random-Code QPSK Modulation Power Spectra," ZHONGGUO KONGJIAN KEXUE JISHU [CHINESE SPACE SCIENCE AND TECHNOLOGY], Vol 2, 1986.

Gain-Guided GaAlAs/GaAs Phase-Locked Diode Laser Array

92FE0058A Shanghai ZHONGGUO JIGUANG [CHINESE JOURNAL OF LASERS] in Chinese
Vol 18 No 8, Aug 91 pp 561-564

[Article by Tu Yuzhen [1458 3768 3791], Jin Zhiliang [6855 1807 5328], Gu Deying [7357 1795 5391], Feng Weizhong [1409 0251 1813], Lin Yueming [2651 2588 2494], Liu Bin [0491 2430], and Fang Zujie [2455 4371 2212] of Shanghai Institute of Optics and Fine Mechanics (SIOFM) of the Chinese Academy of Sciences: "Gain-Guided GaAlAs/GaAs Phase-Locked Diode Laser Array"; MS received 13 Dec 90]

[Text] Abstract

The fabrication technique and characteristics of a gain-guided GaAlAs/GaAs phase-locked laser array comprised of multiple stripes prepared by Zn diffusion with oxide mask are described. Typically, the threshold current is below 200 mA and the output power is more than 240 mW. Far-field measurements also show excellent phase-locking characteristics.

Key words: semiconductor laser, phase-locked array.

I. Introduction

Semiconductor lasers have several advantages, such as compactness, high efficiency and ease of use. However, compared to gas and solid lasers, they are low in power and have a large divergence angle. The phase-locked laser array provides a way to overcome these problems; it has demonstrated abilities indicating a very encouraging future^{1,2} in areas such as solid-state lasers, space optical communications, high-speed optical recording and laser medicine.

The earliest phase-locked array consists of a number of parallel stripes.³ Phase-locking between lasers is accomplished by the overlapping coupling of the optical fields of the stripes (evanescent wave). This type of structure is simple to fabricate and is very efficient. Therefore, despite the development of a number of other phase-locking mechanisms and structures, such as Y-cross-coupling and diffraction coupling,^{4,5} the evanescent-wave coupling mechanism is still the best in terms of performance and it is the most widely used in mass production. This paper describes the experimental results of

gain-guided GaAlAs/GaAs laser arrays prepared by oxide-masked Zn diffusion stripes.

II. Device Structure and Fabrication Technique

Figure 1 shows a schematic diagram of the device. It is a planar double heterojunction (DH) laser grown on an n-GaAs substrate by conventional liquid phase epitaxy. A thin layer of SiO₂ was grown on the epitaxial layer by CVD. After opening several stripes of window by photoetching, Zn was diffused across the n-GaAs top layer to form p⁺-p-n junctions. The n-p-n junction between the stripes has a current-limiting effect. Each device consists of 10 lasers. Each stripe is 5 μm wide and the stripes are 8 μm apart center-to-center. The wavelength of emission can be adjusted by varying the aluminum content (y) in the active layer. Two points must be noted to obtain good phase-locked laser arrays. First, the active layer should be as thin as possible; at the same time, the potential barrier between the active layer and limiting layer should be sufficiently high and steep to result in the lowest possible threshold. Next, every layer should be as homogeneous as possible, especially in terms of composition and thickness.

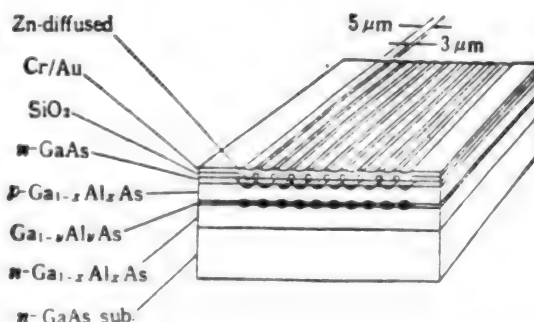


Figure 1. Schematic Diagram of the Array

After Zn diffusion, wafers were trimmed and ohmic contacts were attached. The wafers were cut into chips approximately 250 μm in cavity length, which were then bonded to a copper heat sink for testing.

III. Device Characteristics

3.1 Power/Current Characteristics

Figure 2 shows the typical dc power/current curve measured at room temperature. It shows that the threshold current is 170 mA. It remains linear at an output power of up to 200 mW. Figure 3 shows the linear power output ranges and power conversion efficiencies of a number of devices. The power for device #B-7 was measured at the maximum current output of 1 A. (It is estimated that its power output may exceed 250 mW if the power supply is capable of delivering more current.) The single-face differential quantum efficiency of such devices is in the 25-30 percent range.

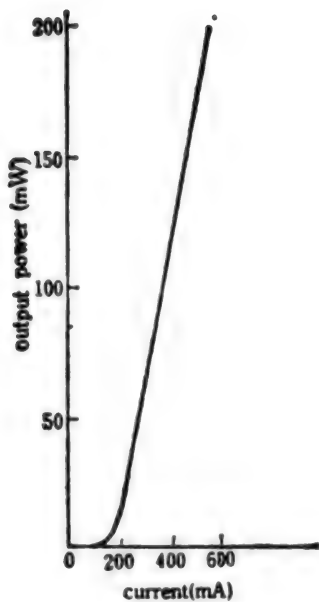


Figure 2. Typical Light-Current Characteristics of the Device

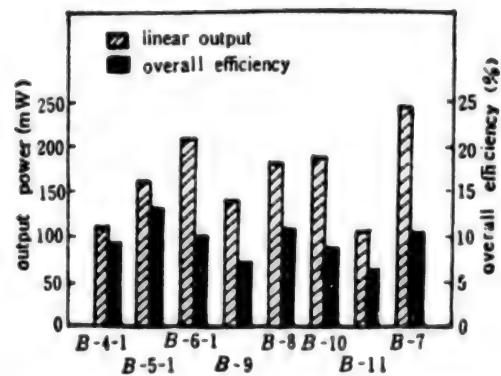


Figure 3. Linear Output and Overall Efficiencies of Eight Devices

3.2 Far-Field Distribution

Figure 4 shows a typical far-field distribution parallel to the junction surface. As one can see, it is a double-lobe beam. Each lobe is $1.7\text{--}1.8^\circ$ wide and the angular spacing between the two lobes is 7.9° . A few devices exhibited only a single lobe, approximately $5\text{--}8^\circ$ in width. In the direction perpendicular to the junction surface, the far-field distribution is similar to that of other conventional semiconductor lasers. The angle of divergence is around 35° .

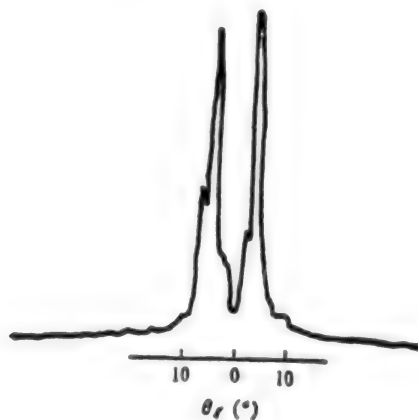


Figure 4. Typical Far-Field Pattern of the Array

3.3 Spectral Characteristics

The wavelength of these GaAlAs/GaAs laser arrays is controlled within a range between 800 and 880 nm. Figure 5 is a typical spectrum. It belongs to multi-mode oscillation as a result of having a gain-guided structure. As the injected current increases, complicated fine structures can be seen for every longitudinal mode. This is related to the competition between modes.

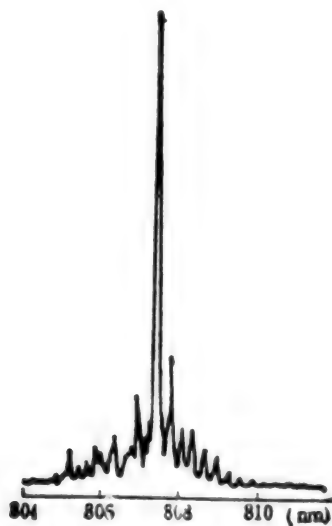


Figure 5. Typical Spectrum of the Array

3.4 Temperature Behavior

Power/current curves were measured at different temperatures, as shown in Figure 6. It was found that the device could still provide more than 100 mW of power output at 80°C. From the data shown in Figure 6, one can also derive that the temperature dependence on threshold current is essentially $I_{th} \propto \exp(T/T_0)$, where $T_0 = 167$ K. If junction temperature rise is taken into account, then the actual characteristic temperature is even higher.

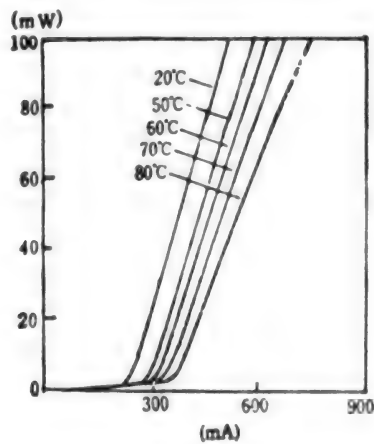


Figure 6. L-I Curves of a Typical Device at Temperature Ranging From 20°C to 80°C

Thermal resistance of these devices were measured spectroscopically and a typical value of 20 K/W was obtained. This number is still too high for a multi-stripe device. Improvement is in progress.

IV. Discussion

The far-field characteristic of an array device is the most apparent and important factor in reflecting its phase-locking behavior. The phase-locked laser arrays tested in this work have a double-lobe far-field distribution. Based on mode-coupling theory of laser arrays, it belongs to the classical Nth-order supermode. This indicates that excellent phase locking has been accomplished between all elements in the array.

Based on mode-coupling theory, the angular spacing between the two lobes for the Nth-order supermode is $\Delta\theta \approx \lambda/w$, where w is the stripe width, which is equivalent to the divergence angle of each individual laser. It was measured that $\Delta\theta \approx 8^\circ$, which is slightly smaller than the divergence angle of a single laser stripe ($10\text{--}12^\circ$). This indicates that each laser has a relatively wide side mode, which favors high-power output. The supermode theory also points out that the beam width for each lobe is $\delta\theta \approx \lambda/W$, where W is the total width of N laser stripes. It was determined to be $\delta\theta \approx 1.7^\circ$. Although it is still not quite at the diffraction limit, compression due to phase locking is already obvious. This shows that there is excellent homogeneity among all elements.

The laser array developed in this work has already been used to pump Nd:YAG and Nd:glass lasers which generated laser pulses at $1.06\text{ }\mu\text{m}$, corresponding to threshold pumping power of 4 and 9 mW, respectively. The laser arrays emit at 808 nm and 800 nm, respectively. The laser pulse was compressed eight times by gain-switching, resulting in a laser pulse of 150 ns in pulse width and 200 mW in peak power.⁷

Some data reported in this paper was supplied by the Joint Optoelectronics Laboratory of Beijing Institute of Semiconductors. The authors wish to thank Zhuang Wanru [8369 1238 1172] and Pan Guisheng [3382 6311 3932] for their contribution. The solid-state laser pumping work was done at the Joint High-Power Laser Laboratory of SIOFM. The authors wish to thank Zhou Fuzheng [0719 1788 2973], Shen Liqing [3088 7787 7230], Fan Dianyuan [5400 7787 7230], and Zheng Guizhen [6774 2710 3791] for their contribution.

References

1. W. Streifer et al., IEEE J. QUANT. ELECTR., QE-24(6), 883-894 (1988).
2. G. Forrest, LASER FOCUS/ELECTRO-OPTICS LASER REVIEW, (2), 4 (1988).
3. D. Scifres et al., IEDM, 82, 354-356 (1982).
4. W. Streifer et al., IEEE J. QUANT. ELECTR., QE-23(6), 744-756 (1987).
5. T. Chen et al., APPL. PHYS. LETT., 43(2), 136 (1983).

6. Lin Yueming et al., JILIN DAXUE ZIRAN KEXUE XUEBAO [JILIN UNIVERSITY JOURNAL OF NATURAL SCIENCES], 1990 Special Issue, 148, 1990.

7. Zhou Fazheng et al., THE REVIEW OF LASER ENGINEERING, 18, 16 (1990).

Principle, Application of Twyman-Green Shearing Interferometer

92FE0164A Shanghai ZHONGGUO JIGUANG [CHINESE JOURNAL OF LASERS] in Chinese
Vol 18 No 10, Oct 91 pp 739-742

[Article by He Anzhi [6320 1344 0037], Wang Hailin [3769 3189 2651], Miao Pengcheng [5379 7720 4453], and Yan Dapeng [7051 1129 7720] of the Department of Applied Physics, East China Institute of Technology: "Principle, Application of Twyman-Green Shearing Interferometer"; MS received 29 Oct 90]

[Text] Abstract

The operating principle of a new lateral shearing interferometer is presented. It uses a Twyman-Green interferometer as a beam splitter, a grating as a detector, and real-time Moire difference method to eliminate system error. The advantages of this interferometer include adjustable sensitivity, high resistance against vibration, and ease of manufacture of large aperture. This interferometer was used to measure flow fields in supersonic wind tunnels and rocket exhaust plumes. Some important results were obtained.

Key words: shearing interferometer, flow visualization.

I. Introduction

A lateral shearing interferometer is a common optical path interferometer. It does not have very stringent requirements with regard to coherence of light source, temperature variation of the environment and vibration. It can be used to measure certain transient flow fields. A transient flow field is varying rapidly, such as the supersonic flow field inside a wind tunnel, or the rocket exhaust plume field. Conventional shearing interferometers include the parallel plate type,¹ Wollaston prism type,² grating type,³ etc. This paper presents the operating principle and applications of a long range, large aperture, high accuracy lateral shearing interferometer. It was constructed by modifying a large aperture fringe interferometer using a small aperture Twyman-Green interferometer as the beam splitter and a grating as a detector element. Real-time Moire difference method is used to eliminate system error. Shearing fringe patterns representing flow fields in a supersonic ($M = 10.29$) shock wave wind tunnel and rocket exhaust plume have been obtained using this interferometer.

II. Principle

The optical layout of the Twyman-Green lateral shearing interferometer is shown in Figure 1. Two flat reflective mirrors M_1 and M_2 and a beam splitter BS form the Twyman-Green interferometer. M_1' is equivalent to M_1 . The angle between M_1' and M_2 is $\theta/2$. When a collimated beam with wavelength λ passes through the phase object (PO) to be measured to enter the Twyman-Green interferometer, lateral shearing interference takes place in an encountering areas between the two beams reflected by M_1 and M_2 after penetrating and reflected by BS. Based on the coordinate system shown in Figure 1, M_1 and M_2 are located at the original. The observation screen (ground glass) P is at plane $z = z_p$. The light reflected by M_1 is parallel to the z axis. Let us assume that the complex amplitude of this beam on the observation screen is $A_0 \exp[i(2\pi/\lambda)g(x, y, z_p)]$. The axis between the beam reflected by M_2 and the z axis on plane XZ is θ . Obviously, the complex amplitude of this light beam on P is $A_0 \exp\left\{i \frac{2\pi}{\lambda} [\theta x + g(x - \theta z_p, y, z_p)]\right\}$. Hence, the total complex amplitude on P is

$$U(x, y, z_p) = A_0 \exp\left[i \frac{2\pi}{\lambda} g(x, y, z_p)\right] + A_0 \exp\left\{i \frac{2\pi}{\lambda} [\theta x + g(x - \theta z_p, y, z_p)]\right\} \quad (1)$$

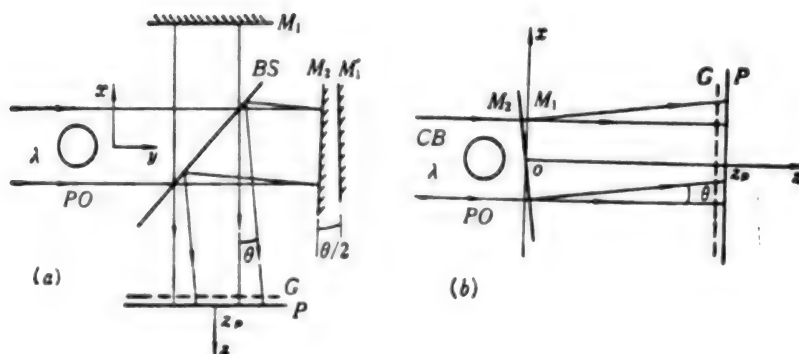


Figure 1. (a) Layout of the Twyman-Green Lateral Shearing Interferometer; (b) Equivalent Optical Layout of (a)

When $g(x, y, z_p)$ varies slow with the coordinate and θz_p is relatively small, we have

$$g(x - \theta z_p, y, z_p) \approx g(x, y, z_p) - \frac{\partial g(x, y, z_p)}{\partial x} \theta z_p,$$

Therefore, the light intensity distribution on P is

$$I(x, y, z_p) = U(x, y, z_p) U^*(x, y, z_p) \approx 2A_0^2 + 2A_0^2 \left\{ \frac{2\pi\theta}{\lambda} \left[x - z_p, \frac{\partial g(x, y, z_p)}{\partial x} \right] \right\}. \quad (2)$$

In the absence of PO, i.e., $\partial g(x, y, z_p)/\partial x = 0$, the above equation is a series of interference fringes with a period $d = \lambda/\theta$. If PO is present, we will notice a displacement of $z_p \frac{\partial g(x, y, z_p)}{\partial x}$.

Let us assume that there is a detecting grating G on the $z = z_p$ plane (i.e., in coincidence with P) and its transmittance is

$$t(x, y) = \frac{1}{2} [1 - \cos \frac{2\pi}{d'} (x + y + ga)] \quad (3)$$

Here, $d' = d/\cos \alpha$ and α is the angle between the grating line and the interference fringe without PO. Hence, the intensity distribution on P is the product of (2) and (3), i.e.,

$$\begin{aligned} I'(x, y, z_p) &= I(x, y, z_p) t(x, y) \\ &= A_0^2 + A_0^2 \cos \frac{2\pi}{d'} (x + y \tan \alpha) + A_0^2 \cos \left\{ \frac{2\pi}{d} \left[x - z_p \frac{\partial g(x, y, z_p)}{\partial x} \right] \right\} \\ &\quad + \frac{A_0^2}{2} \cos 2\pi \left\{ x \left(\frac{1}{d} - \frac{1}{d'} \right) - \left[\frac{z_p}{d} \frac{\partial g(x, y, z_p)}{\partial x} + \frac{y}{d'} \tan \alpha \right] \right\} \\ &\quad + \frac{A_0^2}{2} \cos 2\pi \left\{ x \left(\frac{1}{d} + \frac{1}{d'} \right) - \left[\frac{z_p}{d} \frac{\partial g(x, y, z_p)}{\partial x} - \frac{y}{d'} + ga \right] \right\} \end{aligned} \quad (4)$$

When $\partial g(x, y, z_p)/\partial x$ and α are small, the spatial frequencies of the terms on the right hand side of (4), are $f_1 = 0$, $f_2 \approx 1/d$, $f_3 \approx 1/d$, $f_4 \ll 1/d$, and $f_5 \approx 2/d$. The first and fourth terms have lower spatial frequencies. They are Moire fringes (which can be recognized by the naked eye).⁴ Other terms are considered background on (not recognizable by the naked eye) because of high spatial frequency. Therefore, the intensity distribution of Moire fringes is

$$I_M(x, y) = A_0^2 + \frac{A_0^2}{2} \cos \left\{ \frac{2\pi}{d} \left[x(1 - \cos \alpha) - z_p \frac{\partial g(x, y, z_p)}{\partial x} - y \sin \alpha \right] \right\}. \quad (5)$$

From equation (5), the equation for Moire (bright) fringe is

$$J = \frac{1 - \cos \alpha}{\sin \alpha} x - \frac{z_p}{\sin \alpha} \frac{\partial g(x, y, z_p)}{\partial x} - \frac{d}{\sin \alpha} m, \quad m = 0, \pm 1, \pm 2, \dots \quad (6)$$

Based on equation (6), the displacement of Moire fringes directly reflects the rate of change of the wave front function to be measured. The sensitivity of the interferometer is dependent upon z_p and α .

III. Experiment and Results of Applications

Figure 2 shows the layout of a shearing interferometer for transient flow visualization. L_1 is a beam expander, L_2 and L_3 are large-aperture spherical concave mirrors, and W is the protective window or vessel wall which contains PO. L_3 and lens L_4 form a beam reducing system. A small-aperture (60 mm diameter) Twyman-Green interferometer is used as a beam splitter, which is

installed on a 10-mm-thick 250 mm x 250 mm steel plate to provide better vibration resistance. P_0 and P are arranged to have a conjugate object-image relation. This means that $g(x, y, z_p)$ is the wave front equation (not considering linear magnification between object and image) of a collimated beam after passing through P_0 .

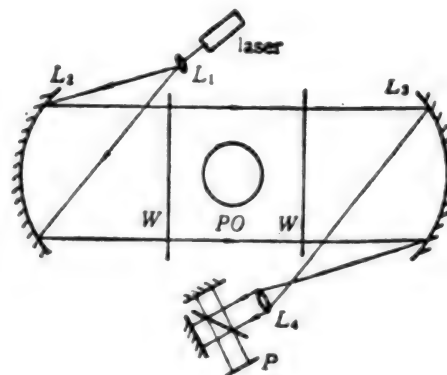


Figure 2. Layout of the Lateral Shearing Interferometer for Flow Visualization

If P_0 is an axial symmetric flow field (symmetric with respect to the y axis), the index of refraction distribution of P_0 from the basic equation of light propagation is:⁵

$$n(r, y) - n_f = \frac{-n_f}{n} \int_r^{r_f} \frac{\frac{\partial g(x, y, z_p)}{\partial x}}{(r^2 - x^2)^{1/2}} dx \quad (7)$$

Here, n_f is the index of refraction of the environment and r_f is the radius of P_0 . Therefore, it is very easy to calculate the distribution of index of refraction of the axial symmetric P_0 based on the Moire fringe equation (6) and equation (7).

Normally, the quality of W is relatively poor. When the aperture of the interferometer becomes too large, as a result of cost consideration, the quality of L_2 and L_3 may deteriorate. In order to eliminate system error, the detecting grating may be prepared as follows. In the absence of P_0 , place a holographic plate on plane $z = z_p$. After exposure by the interference fringes (at a density of 10-30 per mm), the plate is processed and used as the detecting grating (amplitude type). When this grating is accurately placed (manually without the need of any special equipment), the Moire fringes produced, which represent the difference between the interference fringes with P_0 and those of the grating, are free of system error. This is real-time system error elimination.⁶ The density and direction of Moire fringes can be varied by adjusting M_1 or M_2 .

The apparatus shown in Figure 1(a) was first used to measure an alcohol flame field. The Moire fringes obtained are shown in Figure 3. Figure 3(a) shows the Moire fringes without eliminating system error and Figure 3(b) shows the

Moire fringes with elimination of system error. The apparatus shown in Figure 2 was used to measure some transient flow fields. Figure 4 shows the Moire fringes of the flow field inside a supersonic wind tunnel ($M = 10.29$) (only half is shown due to axial symmetry). Figure 5 is the Moire fringes of real rocket exhaust plumes.

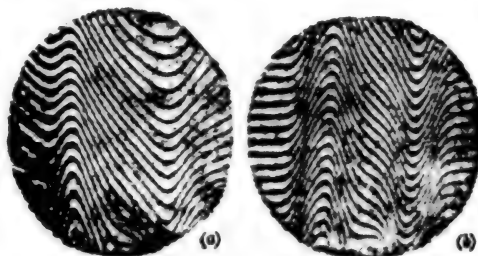


Figure 3. Moire Fringes of an Alcohol-Lamp Flame
(a) without eliminating system errors; (b) eliminating system errors

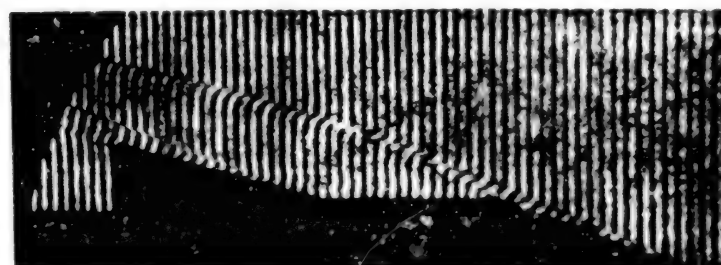


Figure 4. Moire Fringes of a Flow Field in a Supersonic Wind Tunnel

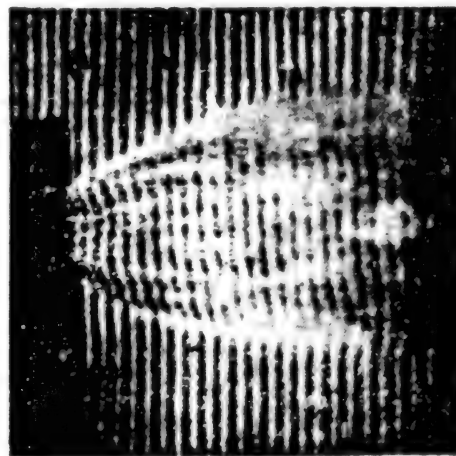


Figure 5. Moire Fringes of a Rocket Exhaust Plume

With some improvement, the apparatus shown in Figure 2 can be tested in an optical workshop.

References

1. L.H. Tanner, J. SCI. INSTRUM., 42, 834 (1965).
2. R.D. Small et al., APPL. OPT., 11, 858 (1972).
3. D.E. Silva, APPL. OPT., 11, 2613 (1972).
4. S. Yokozeiki et al., APPL. OPT., 9, 1011 (1970).
5. E. Keren et al., APPL. OPT., 20, 4263 (1981).
6. Yu Meiwen [0060 5019 2429], "Holography and Optical Information Processing," Defense Industry Publishing Co., 1984.

PE-Calorimeter With Broad Spectra, High Sensitivity, and Fast Response

92FE0164B Shanghai ZHONGGUO JIGUANG [CHINESE JOURNAL OF LASERS] in Chinese
Vol 18 No 10, Oct 91 pp 743-748

[Article by Zhou Fuzheng [0719 1788 2973] and Shen Liqing [3088 7787 7230] of
Shanghai Institute of Optics and Fine Mechanics of the Chinese Academy of
Sciences: "PE-Calorimeter With Broad Spectra, High Sensitivity, and Fast
Response"; MS received 6 Apr 90, revised 3 Dec 90]

[Text] Abstract

A pyroelectric-material-based PE-calorimeter with high sensitivity and fast response covering infrared-visible-X-ray has been designed and constructed. Operating parameters of the calorimeter are calculated. Energy measurements for 1.06 μm and 0.53 μm laser and 0.1-10 keV soft X-ray are made. The sensitivity is 300 mV/ μJ and the response time is less than 2 ns.

Key words: pyroelectric calorimeter.

I. Introduction

A new pyroelectric photo-energy (PE) calorimeter has been designed and constructed to detect weak photon energy signals ranging from the infrared, visible to X-ray band. In addition, it has a fast response time. It has significantly expanded the capability and useful range of conventional calorimeters.¹⁻⁴

Pyroelectric materials are fast responding thermistor elements. When a material is heated due to light irradiation or absorption, a temperature change takes place which causes the thermo-electric dipole to vary. This leads to a change of its surface charge and the intrinsic rate of change is of the order of picosecond. When it is connected to a load, a voltage signal is generated. If the incident light pulse width is far less than the thermal time constant of the pyroelectric material and the electric time constant of the detection circuit, then the peak voltage is proportional to the total energy of the incident photons. The principle is shown in Figure 1. In this work, a calorimeter is designed with parameters to maximize the temperature rise and fast response time upon total absorption of the incident light. In order to expand the spectral response of the detector, carbon or gold black

is chosen as the absorber from IR to UV. In order to raise its resistance against destruction, darkened aluminum oxide was also used. As for soft X-ray, silver is selected as the absorber. If the visible light background is very weak, gold is a more suitable absorber.

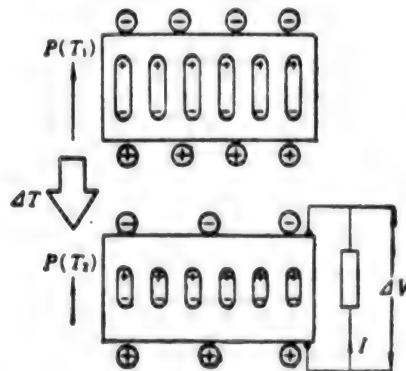


Figure 1. Pyroelectric Effect Irradiated by a Pulsed Light Source

II. Calculation of Parameters

After an absorber is irradiated by a pulse of light, if radiation loss is neglected, under ideal conditions, the temperature rise and voltage variation of a pyroelectric material should be:

$$T_t = \frac{A}{C_T} \int_0^t P_{(t)} dt$$

$$V_t = \frac{A^2 \lambda^*}{CC_T} \int_0^t P_{(t)} dt$$

where C_T is the heat capacity of the material, A is the area of the electrode, C is the total capacitance between pyroelectric elements and the capacitance of the load, λ^* is the pyroelectric coefficient, and $P(t)$ is the power of the light source. The maximum temperature rise and peak voltage can be expressed as:

$$\Delta T = E_a / C_T$$

$$U_{\max} = \xi E_a C_s / A C$$

where $\xi = \lambda^*/\epsilon C_p$ is the pyroelectric constant of the material, ϵ is the dielectric constant, C_p is the volumetric specific heat, E_a is the absorbed incident photo-energy, and C_s is the capacitance between pyroelectric elements. It is apparent that the maximum temperature rise and peak voltage are proportional to the total energy of the incident light. Afterward, temperature and voltage decay according to the following equations:

$$T_t = \frac{E_a}{C_T} e^{-t/\tau_T} / a_T$$

$$V_t = \frac{A \lambda^* E_a}{C C_T} \cdot \frac{1}{\tau_T - \tau_e} \left[\frac{\tau_T}{a_e} e^{-t/\tau_e} - \frac{\tau_e}{a_T} e^{-t/\tau_T} \right]$$

where $a_T = 1 - e^{-T_1/\tau_T}$, $a_e = 1 - e^{-T_1/\tau_e}$, T_1 is the repetition frequency of the incident light source, and τ_T is the overall hot time constant of the calorimeter. The hot time constant of the absorber determines the rise time of the calorimeter.

$$\tau_{th} = \rho C_p d^2 / K,$$

where ρ , K_p and d are the density, thermal conductivity and thickness of the absorber, respectively. In order to achieve total absorption, its thickness must be at least $d = (\ln 100)/\alpha$, where α is the absorption coefficient of the absorber. τ_e is the time constant of the calorimeter:

$$\tau_e = (R_1 // R_2) \cdot (C_1 // C_2)$$

where R_1 is the resistance of the pyroelectric material, $C_1 = k\epsilon_0 A/d$ is the electrode capacitance, and $k\epsilon_0$ is the dielectric constant of the pyroelectric material. R_2 and C_2 are the input impedance and capacitive reactance, respectively. Since the electric time constant of the calorimeter is far less than its thermal time constant, the recovery time of the calorimeter is determined by the discharge time of the electric circuit. Usually $R_2 \ll R_1$, $C_2 \ll C_1$, therefore, the maximum frequency for the calorimeter to receive light pulses is

$$f_c = 1/2\pi\tau_e \approx 1/2\pi R_2 C_1$$

A 10-mm-diameter calorimeter was designed. The pyroelectric material is lithium tantalate (LiTaO_3), $\xi = 4600$, incident light pulse energy is of the order of a few microjoules, pulse width is less than 50 ns, and repetition frequency of the calorimeter is 100 Hz. The calculated parameters of this calorimeter are shown in Table 1. In the IR-UV region, its sensitivity is 400 mV/ μJ . In the soft X-ray band, its sensitivity is 40 mV/ μJ . Its rise time is 0.5 μs , fall time is 2 ms(1/e). Its temperature and voltage variations are shown in Figure 2.

Table 1. Parameters of PE-Calorimeter

Crest voltage	$V_{max} = 200 \text{ mV}$
Sensitivity	400 mV/ μJ (IR-V); 40 mV/ μJ (X-ray)
Rise time	$T_r = 0.1 \mu\text{s}$
Electrical time constant	$\tau_e = 2 \text{ ms}$
Repetition frequency	$f_c = 100 \text{ Hz}$
Signal-to-noise ratio	$N = 100$ (IR-V); $N = 40$ (X-ray)
Hot time constant of absorption body	$\tau_{th} = 20 \text{ ns}$
Hot time constant of PE	$\tau_{th,PE} = 170 \text{ s}$
Temperature increment of single pulse	$\Delta T = 0.014 \text{ K}$

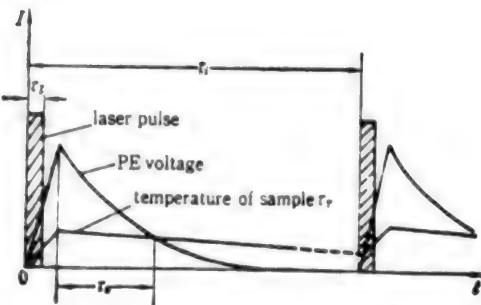


Figure 2. Changes of PE Voltage and Temperature Versus Time

III. Spectral Response

From IR, visible to UV, the pyroelectric material has excellent spectral response. With a thin layer of highly absorbant gold or carbon black, total absorption could be attained (see Figure 3). This paper focuses on the response of the calorimeter to soft X-ray. Between 0.1 keV and 10 keV, gold absorbs well and is used by many soft X-ray detectors. However, in a laser plasma, in addition to X-ray from the target, there are also scattered laser and a wide band of radiation from nonlinear effects associated with ions and electrons. To this end, polished silver is a suitable absorber because it not only absorbs soft X-ray⁵ to a great extent but also reflects visible and IR highly.⁶ At 0.1-10 keV, $\bar{\alpha}_{Ag} \approx 2 \times 10^5 \text{ cm}^{-1}$, and the minimum silver thickness is 230 nm.

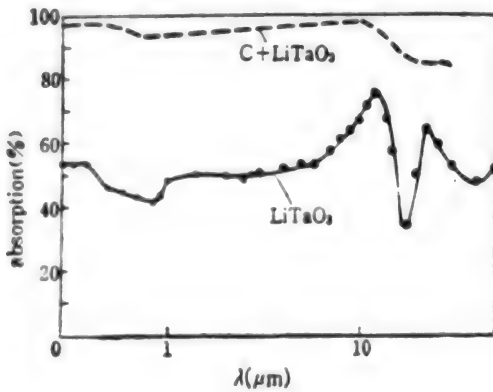


Figure 3. Absorption of C Coated on LiTaO₃ Versus Wavelength

With the addition of an aluminum-plated thin Mylar film window to allow X-rays to penetrate and to block ions and to further reflect light, at 0.1-10 keV, $\bar{\alpha}_{Al} \approx 1 \times 10^5 \text{ cm}^{-1}$, $\bar{\alpha}_{Mylar} \approx 5 \times 10^3 \text{ cm}^{-1}$. Assuming one-third of the X-rays penetrates, then the minimum aluminum thickness is

$$d_{Al} = [\ln 3 - \alpha_M d_M] / \alpha_{Al} = 80 \text{ nm}$$

The intensity of normal incident and small incident angle IR-visible light is reduced to 10^{-3} after double reflection by aluminum and silver. As for

large angle scattered light, only 0.1 percent is absorbed. The calculated signal to noise ratio, i.e., X-rays absorbed at the absorber surface to light noise, $S/N \leq 40$. The spectral response to 0.1-10 keV soft X-rays of a calorimeter with 1- μm -thick silver absorber and 0.5- μm -thick Parylene window plated with a 0.2- μm layer of aluminum is calculated and shown in Figure 4. At the center of the band, i.e., 1 keV, it is designed to absorb up to 94 percent.

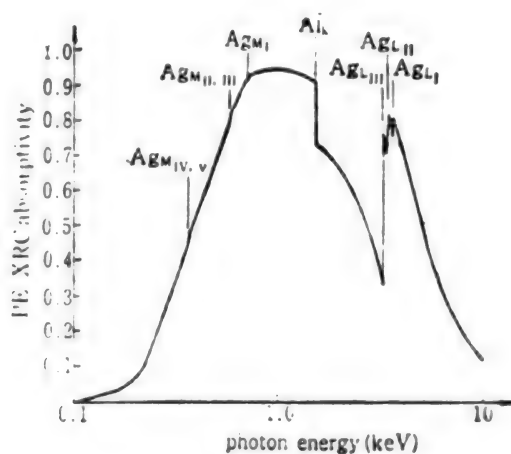


Figure 4. Spectral Response of Soft X-Ray Calorimeter XRC Spectral Response, Absorber: 1 μm Ag; Filter: 0.2 μm Al

IV. Experimental Results

Figure 5 shows the structure of the calorimeter. The LiTaO_3 crystal is 50 μm thick and $14 \times 14 \text{ mm}^2$ in area. Both sides are gold plated. The absorber is 5- μm -thick gold black. The effective light reception aperture is 10 mm in diameter. The pyroelectric voltage output is coupled to a field effect transistor (FET) for impedance matching. After going through amplification and peak preservation, it is directly displayed digitally. In order to adapt to multi-channel laser automatic measurement, microprocessor technology is also employed. A 1.06- μm -wavelength, 5-ns-pulse-width, 5-mJ laser was used for calibration. A calibrated calorimeter is connected to the primary laser path. It enters the pyroelectric calorimeter after a factor of 10^3 - 10^4 of attenuation. The energy is held 0.1-10 μJ for calibration. A frequency doubler KTP crystal can be plugged into the main optical path for calibration at 0.53 μm .

Figure 6 shows a typical waveform of the pyroelectric calorimeter. The rise time is 0.02 ms and the fall time is 1.2 ms. Complete recovery takes approximately 4 ms. It can be used to measure individual laser pulse energy at a repetition frequency of 200 pps of the average energy of a device. The result of calibration experiments is shown in Figure 7. The sensitivity is 310 mV/ μJ between 0.1 μJ and 5 μJ . It is linear with respect to the energy output of the laser. This calorimeter has been successfully used to measure the weak laser energy of forward Raman scattering less than 50 ps in pulse width at 1.5 μm .

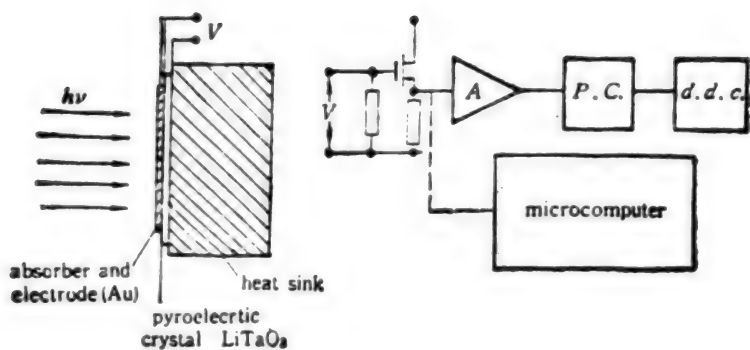


Figure 5. Mechanical Construction of PE-Calorimeter

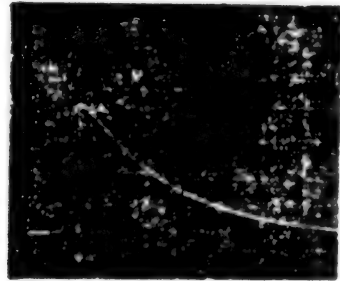


Figure 6. Typical PE-Calorimeter Signal

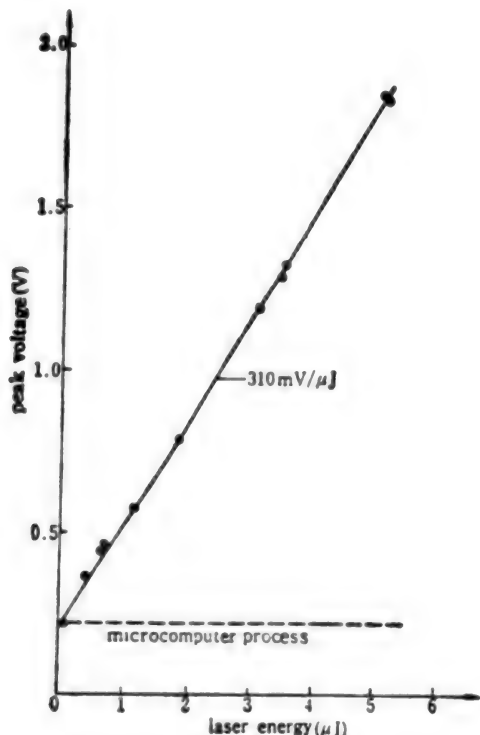


Figure 7. Calibration Curve of PE-Calorimeter

The absorber of the soft X-ray calorimeter is a 1- μm -thick silver film. Two window materials, 3.6- μm -thick aluminum and 0.2- μm -thick aluminum on 0.5- μm -thick Parylene, are used. It is identical in construction as the light calorimeter. Figure 8 shows the schematic diagram of the calorimeter for laser plasma generated soft X-rays. The energy output of the laser is 10 J, the pulse width is 20 ns, and the repetition frequency is 1 pps. Medium Z targets such as copper and iron are used to obtain higher soft X-ray emission. The target surface power density is $10^{12-13} \text{ W/cm}^2$. In order to identify the X-rays emitted by laser plasma, the probe matching load was lowered to improve response time. A series of waveforms have been obtained, as shown in Figure 9. (a) is the PE-IRC signal, (b) is the PE-XRC signal, (c) is the

superposition of these two signals, and (d) is a typical PE-XRC signal which consists of three parts. First is the transient pressure wave^{7,8} and it is followed by X-ray energy integration signal. At the same time, it is superimposed with low-frequency elastic photoacoustic wave and thermal electric noise. The sensitivity of the calorimeter is 30 mV/ μ J, which is one order of magnitude lower than that of the light calorimeter. This decrease in sensitivity is due to higher heat capacity of the soft X-ray absorber and lower impedance circuit. Figure 10 shows the result of using this calorimeter to monitor laser plasma X-ray emission. It was found that X-ray emission is essentially linear with respect to the driving laser source. The threshold to produce X-rays is approximately 0.3 J. This is in agreement with theoretical calculation and other X-ray diagnostic experiments.^{9,10}

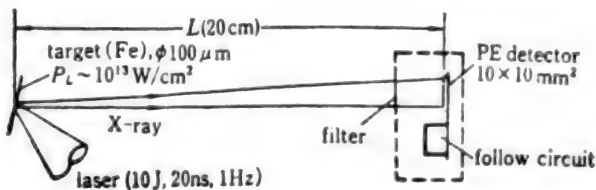


Figure 8. Schematic Diagram of Soft X-Ray Detection

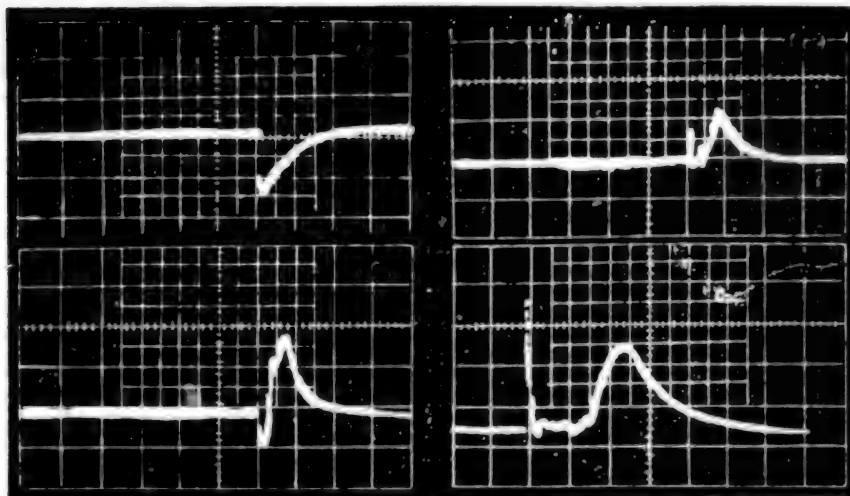


Figure 9. Pyroelectric Signals

(a) PE-IRC signal, 0.1 V/div, 5 $\mu\text{s}/\text{div}$; (b) PE-XRC signal, 0.2 V/div, 5 $\mu\text{s}/\text{div}$; (c) Complex signal, 0.2 V/div, 5 $\mu\text{s}/\text{div}$; (d) Typical PE-XRC signal, 0.2 V/div, 2 $\mu\text{s}/\text{div}$

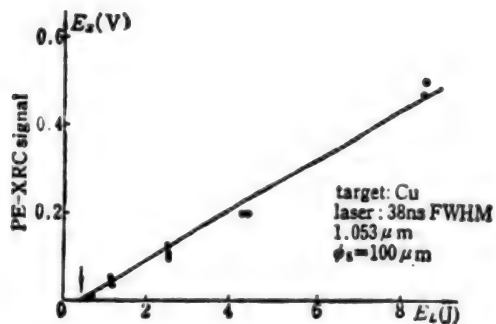


Figure 10. Dependence of PE-XRC Signal on Laser Energy

A portion of the experiments was done at Osaka University in Japan. The authors wish to thank Professor C. Yamanaka, Director S. Nakai, and Professor T. Yamanaka for their support and T. Jitsuno and M. Takahashi for their collaboration.

References

1. Wang Ruihua [3769 3843 5478] and Zhou Fuzheng, JIGUANG [LASERS], Vol 5, No 11, 1984, p 201.
2. Lin Kangchun [2651 1660 2504] and Zhou Fuzheng, HE JUBIAN YU DENGZI WULI [NUCLEAR FUSION AND PLASMA PHYSICS], Vol 1, 1983, p 41.
3. S.R. Gunn et al., REV. SCI. INSTRUM., 48, 1375 (1977).
4. H. Nishimura et al., REV. SCI. INSTRUM., 56, 1128 (1985).
5. H.J. Hageman et al., JOSA, 65(6), 742 (1975).
6. Dar-Yuan Song et al., APPL. OPT., 24(8), 1164 (1985).
7. A.C. Tam, REV. MOD. PHYS., 58(2), 381 (1986).
8. Zhou Fuzheng et al., European Materials Society, France, Strasbourg, 1989.
9. T.N. Lee et al., APPL. PHYS., 46, 3789 (1975).
10. D.J. Nagelet et al., APPL. OPT., 23(9), 1428 (1984).

Development of High-Density Energy Storage Pulsed Capacitor

92FE0164C Shanghai ZHONGGUO JIGUANG [CHINESE JOURNAL OF LASERS] in Chinese
Vol 18 No 10, Oct 91 pp 788-789

[Article by Yuan Cunde [6678 1317 1795], Han Aimei [7281 1947 1188], Xu Zhenhua [1776 2182 5478], Huang Donghai [7806 2639 3189], Lin Xianping [2651 6343 1627], and Chen Haoliang [7115 6275 2733] of Shanghai Institute of Optics and Fine Mechanics, the Chinese Academy of Sciences: "Development of High-Density Energy Storage Pulsed Capacitor"; MS received 12 Feb 91]

[Text] Abstract

A high-density energy storage pulsed capacitor was developed to match the operating characteristics of the power supply system for the Shen Guang laser facility. Its energy storage density is 0.218 J/cm^3 and has a minimum life of 40,000 cycles.

Key words: energy storage density, operating life.

Introduction

A pulsed capacitor was developed in 1982 to be used in the power supply for the first high-power laser in China. It was appraised to have an energy storage density of 0.145 J/cm^3 . It is the leader among similar pulse capacitors made of pure paper dielectric materials. As the development of the high-power laser progressed, its power level continued to elevate. As a result, its power supply requirements also stepped up accordingly. The power supply must be compact and have a high energy storage capacity. Hence, the energy storage density of the capacitor must be raised.

From the energy storage density equation for a pulsed capacitor

$$W/V = \frac{1}{2} \epsilon_0 \epsilon_r E^2 \quad (\text{J/cm}^3)$$

we can see that the field strength of the dielectric E is the key parameter to improve the energy storage density of a pulsed capacitor. The next parameter is the relative dielectric constant ϵ_r . Based on the operating characteristics of pulse capacitor and operating conditions of the No. 12 laser's

power supply, a paper-membrane composite dielectric soaked with a suitable insulating oil was employed to raise the operating field strength. After over 70,000 charge and discharge cycles with smaller prototype capacitors, we found that the field strength of this dielectric is substantially higher.

Based on the structure of the smaller prototype capacitors, practical pulsed capacitors were designed. Over 40,000 25 kV oscillation discharge tests (16 percent anti-peak voltage) were done at a charge/discharge frequency of two times/minute without any signs such as bulge, leakage and partial discharge. In addition, we also measured the capacitance and dielectric loss $\text{tg}\delta$ at every 5,000 cycles. The data is as follows:

Item		Times								
		0	5×10^3	10^4	1.5×10^4	2.0×10^4	2.5×10^4	3×10^4	3.5×10^4	4×10^4
Data										
1*	C (μF)	8.947	8.957	8.953	8.957	8.963	8.973	8.966	8.961	8.970
	$\text{tg}\delta$ (%)	0.3041	0.3749	0.4131	0.3887	0.3631	0.3165	0.3768	0.3700	0.3691
2*	C (μF)	9.100	9.123	9.117	9.123	9.131	9.148	9.187	9.131	9.147
	$\text{tg}\delta$ (%)	0.3087	0.3667	0.4200	0.4024	0.3687	0.3387	0.3900	0.3800	0.3862
3*	C (μF)	9.090	9.109	9.101	9.111	9.118	9.135	9.126	9.118	9.134
	$\text{tg}\delta$ (%)	0.2927	0.3599	0.4001	0.3864	0.3462	0.3144	0.3700	0.3609	0.3666
4*	C (μF)	9.072	9.088	9.085	9.082	9.090	9.097	9.090	9.088	9.094
	$\text{tg}\delta$ (%)	0.3187	0.3986	0.4364	0.4171	0.3869	0.3895	0.4024	0.4000	0.3929
Climate	fine	fine	foggy	fine	cloudy	drizzling	fine	fine	cloudy	

From the table, considering measurement error and effect of residual charge, humidity and temperature, capacitance and dielectric loss are very stable.

In order to further test the insulation strength of the dielectric to understand the operating margin above the rated voltage, three voltage endurance tests were conducted consecutively after the 40,000-cycle test. The test voltage is 1.1 times that of the rated voltage, i.e., 27.5 kV. The duration is 1 minute. All three tests passed. After the voltage endurance tests, capacitance and dielectric loss were measured again and the results are shown in the following:

Item	1*		2*		3*		4*		Climate	
	C (μ F)	tg δ (%)	C (μ F)	tg δ (%)	C (μ F)	tg δ (%)	C (μ F)	tg δ (%)		
Data										
Case	Before voltage endurance	8.960	0.3741	9.132	0.3900	9.118	0.3677	9.086	0.3998	drizzling
	After voltage endurance	8.970	0.3691	9.147	0.3863	9.134	0.3666	9.094	0.3929	drizzling

Based on the above experimental results, the capacitance and dielectric loss of the pulsed capacitor meet the design criteria, and its minimum operating life is 40,000 cycles. In a power supply, it may last 10 years. Its nominal capacitance is 9.6 μ F and the energy storage density is 0.218 J/cm³. This is 1.5 times of that of the capacitor in the No. 12 laser facility. It can reduce the area of the power supply and high voltage cable by one-third. The overall economic benefit is substantial.

Furthermore, this pulsed capacitor can also be used as an ordinary pulsed capacitor.

Picosecond Optical Pulse Generation at High Repetition Rate by Gain-Switched Semiconductor Laser

92FE0047A Beijing BANDAOTI XUEBAO [CHINESE JOURNAL OF SEMICONDUCTORS] in Chinese Vol 12 No 9, Sep 91 pp 575-577

[Article by Sun Wei [1327 0251], Yi Maobin [5902 5399 2430], Wang Yanhui [3769 5333 6540], and Liu Zongshun [0491 1350 7311] of the Department of Electronics Science, Jilin University: "Picosecond Optical Pulse Generation at High Repetition Rate by Gain-Switched Semiconductor Laser"; MS received 23 Mar 91, revised 23 Apr 91]

[Text] Abstract

The generation of ps optical pulses with a gain-switched 1.3 μm InGaAsP semiconductor laser is reported. The pulse width (FWHM) varies between 16 and 23 ps depending upon frequency. Its repetition rate is continuously tunable in the 1-5 GHz range.

I. Introduction

The generation of ps optical pulses by a semiconductor laser is of great importance to high-speed, high-volume fiber-optic communications and high-speed optical information processing. In recent years, optoelectronic sampling systems using semiconductor lasers as light sources have appeared. Among various techniques to produce ultrashort light pulses with a semiconductor laser, direct modulation gain-switching is most attractive because of its simplicity, compactness, high modulation frequency and continuous tunability. On the basis of our past work,^{1,2} by selecting devices with a high-quality current-confinement layer and improving the conditions to generate ultrashort optical pulses, 16-ps-wide (FWHM) pulses have been obtained. Moreover, the repetition frequency of such ultrashort light pulses has been raised to 5 GHz. It becomes a light source for the ultra-high-speed optoelectronic sampling device currently under development.

II. Experiment

Through a T bias device, amplified microwave signals from the microwave source are applied, simultaneously with a dc bias, to the laser. A power meter is used to monitor the microwave energy applied to the laser. The pulse width

of ps optical pulses generated by the gain-switched laser at a repetition of several GHz is monitored with an intensity autocorrelator. A high-speed detector and a wide-bandwidth oscilloscope (Tek 7104 with S₄ sampling probe) are used to determine the repetition rate and waveform. Figure 1 is a block diagram which shows the principle of generating and measuring ps optical pulses by direct modulation.

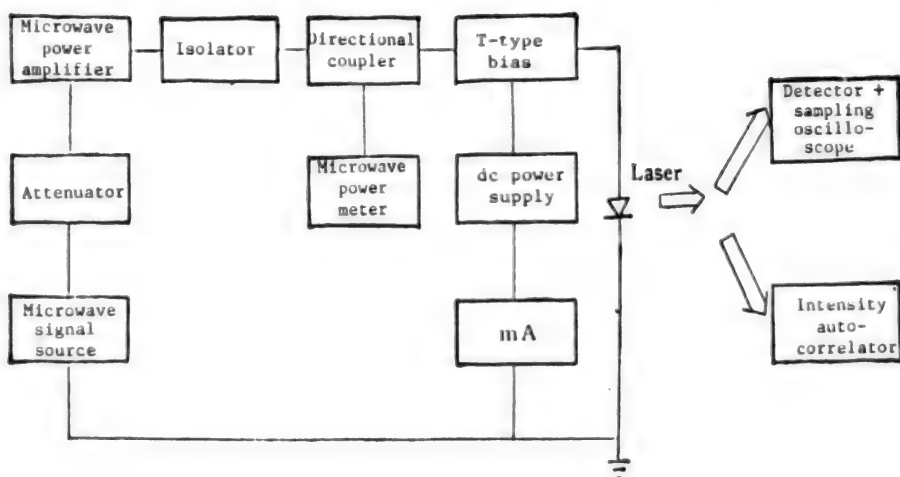


Figure 1. Block Diagram of Generation and Measurement of ps Optical Pulses by Direct Modulation of a Laser

The semiconductor laser used in this experiment to generate ultrashort light pulses is a buried crescent-shaped InGaAsP/InP laser. At room temperature, its wavelength is 1.3 μm and its threshold current is approximately 20-25 mA. The laser cavity is approximately 200 μm in length. The core is sealed with microwave packaging to suit high-frequency operation. A direct modulation gain-switching method was used to generate ultrashort optical pulses. The bias current is between 1 and 2 times that of the threshold current. The microwave power was controlled at approximately 0.5 W. The autocorrelation function of the intensity of these ultrashort pulses is measured by a 1.3 μm intensity autocorrelator which was developed at our laboratory. The intensity autocorrelation system belongs to a second-harmonic collinear type with background. The peak to background ratio is typically 3:1. The frequency doubler is a lithium-iodate crystal. It is transparent in the 0.3-3.5 μm range, which covers the 1.3- μm fundamental frequency and 0.65- μm second harmonic.

III. Results and Discussion

Using a direct modulation gain-switching method, the ps optical pulses generated by a InGaAsP laser is continuously tunable over a repetition-rate range of 1-5 GHz. The FWHM of the intensity autocorrelation function varies between 22.6 and 33 ps depending upon frequency. When calculating the measured intensity autocorrelation curve based on a Gaussian model, the FWHM of the corresponding light pulse is 16-23 ps. Table 1 lists the operating conditions and pulse parameters of the shortest pulses obtained at several important frequencies. Figure 2 shows the intensity autocorrelation curve

of the ultrashort pulse at 5 GHz. Figure 3 [photo not reproduced] shows the light pulse repeating at 4 GHz as measured with a detector (Ge photodiode) and a Tek 7104 sampling oscilloscope (with S₄ probe). The width (FWHM) is limited to 80 ps due to the response of the detector.

Table 1. Operating Conditions and Light Pulse Parameters at Several Frequencies

Repetition rate (GHz)	Bias current I/I _{th}	Microwave power (mW)	Intensity autocorrelation function FWHM (ps)	Optical pulse FWHM (ps)
1.3	1.0	400	22.6	16
2.1	1.5	400	22.9	16
3.0	1.5	400	27	19
4.0	1.8	500	31	22
5.0	1.8	500	33	23

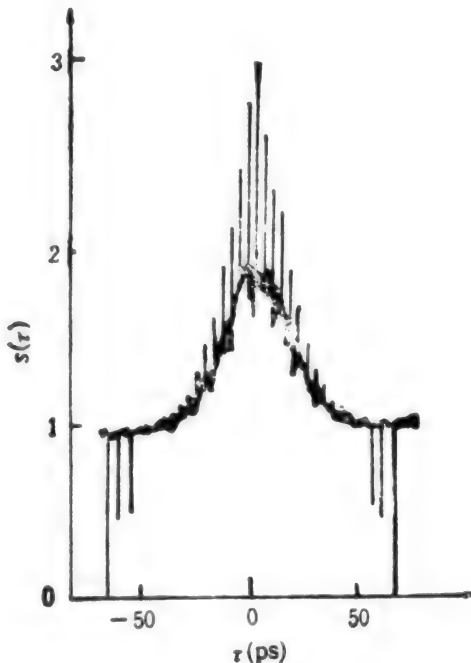


Figure 2. Intensity Autocorrelation Curve for the 5-GHz Ultrashort Optical Pulse

The operating conditions to generate ultrashort optical pulses at different repetition rates have been determined experimentally. When the dc bias of the laser is set between 1 and 2 times the threshold current, the single pulse generated is very narrow. At a fixed repetition rate, there is an optimal match between microwave power and dc bias at which the pulse width is the narrowest. With increasing frequency, in order to obtain the shortest

possible pulse, the dc bias must also rise. In addition, the quality of the p-n junction confinement layer of the laser would also affect the generation of light pulses. When the current-confinement layer is satisfactory, current can be effectively injected into the source, which favors the generation of ultrashort optical pulses, during large-signal operation. More work is underway to further reduce the pulse width and increase the repetition rate.

References

1. Jia Gang [6328 0474], Sun Wei, Yi Maobin, and Gao Dingsan [7559 7307 0005], JILIN DAXUE ZIRAN KEXUE XUEBAO [JILIN UNIVERSITY JOURNAL OF NATURAL SCIENCES], 3, p 42, 1990.
2. Jia Gang, Sun Wei, Yi Maobin, and Gao Dingsan, HONGWAI YANJIU [CHINESE JOURNAL OF INFRARED RESEARCH], 9, p 389, 1990.

GaInAs/InP Quantum-Well Structures Grown by Low-Pressure MOVPE

92FE0047B Beijing BANDAOTI XUEBAO [CHINESE JOURNAL OF SEMICONDUCTORS] in Chinese Vol 12 No 9, Sep 91 pp 578-582

[Article by Duan Shukun [2451 2885 0981], Xiong Feike [3574 7378 0344], Li Xuebin [2621 1331 2430], Li Jing [2621 2533], Wang Yutian [3769 3768 3944], Jiang Desheng [3068 1795 3932], Xu Junying [1776 0193 5391], Wan Shouke [8001 1108 4430], and Qian Jiajun [6929 1367 7486] of the Institute of Semiconductors of the Chinese Academy of Sciences: "GaInAs/InP Quantum-Well Structures Grown by Low-Pressure MOVPE"; MS received 28 Jan 91, revised 9 Apr 91]

[Text] Abstract

The growth of a lattice-matched $\text{Ga}_{1-x}\text{In}_x\text{As}/\text{InP}$ quantum well material by low-pressure metallorganic vapor phase epitaxy (LP-MOVPE) is reported. X-ray double crystal diffraction and transmission electron microscope measurements show excellent periodicity in the multi-quantum-well structure and interfacial quality. The shift of bandgap transition toward higher energy due to quantum-size effect is observed in both photoluminescence (PL) and absorption spectra.

$\text{Ga}_{1-x}\text{In}_x\text{As}$ is an important tertiary semiconductor. $\text{Ga}_{0.47}\text{In}_{0.53}\text{As}$ lattice-matched to InP has been used in optoelectronic components and high-speed devices, such as detectors in long-wavelength fiber optic communications. In recent years, the emission and reception wavelength of $\text{Ga}_{1-x}\text{In}_x\text{As}/\text{InP}$ quantum-well material can be varied between $1.6 \mu\text{m}$ and $1.1 \mu\text{m}$, covering the two windows at $1.3 \mu\text{m}$ and $1.55 \mu\text{m}$ for long-wavelength fiber optic communications, using "band-gap engineering design" based on the quantum-size effect. Compared to ordinary heterojunction structures, a quantum-well laser has a series of advantages such as low threshold, tunability, weak temperature dependence, narrow spectral width and high relaxation oscillation frequency.

$\text{Ga}_{1-x}\text{In}_x\text{As}/\text{InP}$ quantum wells may be grown by LP-MOVPE,¹⁻³ normal-pressure MOVPE,⁴⁻⁷ hydride VPE,⁸ chloride VPE,⁹ vapor-phase suspension epitaxy,¹⁰ MBE,¹¹ MOMBE,^{12,13} GSMBE,¹⁴ and CBE.¹⁵ LP-MOVPE was selected in this work because compared to other techniques it not only can produce an ultra-thin-layer steep heterojunction structure but also has the potential for mass production. The growth of single-layer $\text{Ga}_{1-x}\text{In}_x\text{As}/\text{InP}$ quantum wells by LP-MOVPE has been reported by Seifert.³

It is much more difficult to grow $\text{Ga}_{1-x}\text{In}_x\text{As}/\text{InP}$ quantum-well material than $\text{GaAs}/\text{Ga}_{1-x}\text{Al}_x\text{As}$ quantum-well material because not only the x of the $\text{Ga}_{1-x}\text{In}_x\text{As}$ potential-well layer must be precisely controlled to minimize possible lattice mismatch and stress caused by solid solution composition variation, but Group III and V sources must be rapidly introduced to the reaction chamber alternately to achieve a steep heterojunction interface. In this work, GaInAs/InP was grown in a horizontal LP-MOVPE device with a rectangular cross section. The pressure in the reaction chamber is 50 mbar. A zero-dead-space Vent-run switch valved mixer was used to rapidly switch reactants in and out of the reaction chamber. The carrier gas is H_2 purified by diffusion across Pd. The total gas flow rate is 10 l/min [liters/minute]. The linear gas velocity inside the reaction chamber is approximately 400 cm/s (room temperature). The temperatures of the containers for Group III sources trimethyl germanium (TMG) and trimethyl indium (TMI) are fixed at -10°C and 17°C, respectively. Their pressures are set at 1,050 mbar and 300 mbar, respectively. Group V sources are pure PH_3 and pure AsH_3 . The substrates are S or Fe doped pure (100) InP single crystals.

Three types of GaInAs/InP quantum-well-structure materials were prepared: 1) single quantum well, 2) multiple single quantum wells of different widths, and 3) multi-quantum-well. Using the growth of multiple single quantum wells as an example, the process is as follows:

Before epitaxy, the InP substrate is heat treated in an atmosphere of PH_3 containing H_2 . It is annealed for 10 minutes at 700°C before proceeding with epitaxial growth at 600°C. The first layer to be grown is a 250-nm-thick InP buffer layer. The next is a $\text{Ga}_{1-x}\text{In}_x\text{As}$ reference layer, followed immediately by a 10-nm-thick InP layer as the potential barrier between wells. Then, five $\text{Ga}_{1-x}\text{In}_x\text{As}$ potential wells are grown and their growing time periods are 20, 10, 5, 3, and 1 seconds, respectively. The growth conditions are identical to those for the reference layer. There is a 2-second interruption between the carrier and the well due to switching to allow the gas composition inside the reaction chamber to thoroughly change over. In addition, when we begin to grow the potential wells, TMI and PH_3 are shut off. AsH_3 is turned on after 1 second and TMG and TMI are let in 1 second after that. When the well is done and the barrier is about to be grown, the opposite steps are taken. There is also a 2-second interruption. After the entire quantum-well structure is completed, a 250-nm layer of InP is deposited as the cover. Similar procedures are used to prepare a multi-quantum-well structure. However, it is not necessary to grow the GaInAs reference layer. Moreover, the number of wells and the time of growth are different. After epitaxy is completed, the sample is cooled in an atmosphere of PH_3 containing H_2 . Analyses such as X-ray double-crystal diffraction, transmission electron microscopy (TEM), photoluminescence (PL), and absorption spectroscopy were performed on $\text{Ga}_{1-x}\text{In}_x\text{As}/\text{InP}$ quantum wells prepared.

The radiation source for the X-ray double crystal diffraction analysis is a $\text{CuK}\alpha_1$ source. The first crystal (monochromator) uses high-purity Si (422) for diffraction. The first slit is 0.05 mm and the second slit is 0.02 mm.

Two transmission electron microscopes, an EM-420 and a JEM-200cx, were used at 120 KV and 200 KV, respectively. Dual-beam diffraction measurements were made along the 000 and 002 directions. High-resolution electron micrographs (HR-EM) were taken over 17 beams near the transmitted beam. All specimens have a <110> cleavage direction. The sample wafer was glued together face-to-face and then mechanically ground and optically polished with $\text{Br}_2\text{CH}_3\text{OH}$ to 30-40 μm . It was then bombarded with an Ar^+ beam of 3.5-4.0 kV until reaching a thickness that is electronically transparent.

PL measurements were done using an Ar^+ laser (5145 Å) as the excitation source, which typically has a power of 20 mW. Photoluminescence goes through a grating monochromator and then reaches a liquid-N₂-cooled Ge detector. The signal is amplified by a lock-in amplifier and then recorded. Samples are placed in liquid helium, on the cold finger of a refrigeration unit and in the air to be measured at 4.2 K, 10 K and room temperature, respectively. The light-absorption experiment is done at 10 K. The light source is a chopped 50-W tungsten-iodide lamp which shines on the specimen after passing through a monochromator. Transmitted light is received by a Ge photodiode and amplified by a lock-in amplifier. The entire measurement system is computer-controlled. The transmittance curve is normalized by dividing the measured response curve with a sample to that obtained without a sample.

X-ray double crystal diffraction analysis shows that along the direction of growth the lattice mismatch strain of the three types of $\text{Ga}_{1-y}\text{In}_x\text{As}/\text{InP}$ quantum-well materials described earlier is of the order of 10^{-4} . This is in agreement with the lattice mismatch strain of $< 5 \times 10^{-4}$ when growing a 1- μm -thick $\text{Ga}_{1-x}\text{In}_x\text{As}$ on an InP substrate under identical conditions. When measuring multi-quantum-well specimens, the Pendellösung effect¹⁶ was observed on the X-ray double-crystal diffraction oscillation curve, which is an indication of crystal perfection. This is consistent with the fact that no defects were found with TEM (200 nm x 200 nm).

Figure 1 shows the X-ray double-crystal diffraction pattern of a $\text{Ga}_{1-x}\text{In}_x\text{As}/\text{InP}$ specimen with seven identical wells in the vicinity of the (400) Bragg peak of InP. In addition to the peak of the substrate, there are a series of satellite peaks which proves the presence of a superlattice. From the angular distance between the satellite peaks, one can find the period D of the superlattice (i.e., the sum of potential-well thickness (D_Z) and barrier thickness (D_B)):

$$D = \frac{\lambda}{2 \cos \theta_B} \cdot \frac{1}{\Delta\theta}, \quad (1)$$

where λ is the X-ray wavelength and $\Delta\theta$ is the angular distance between two neighboring peaks. Based on equation (1), the superlattice of this specimen has a period of 23 nm.

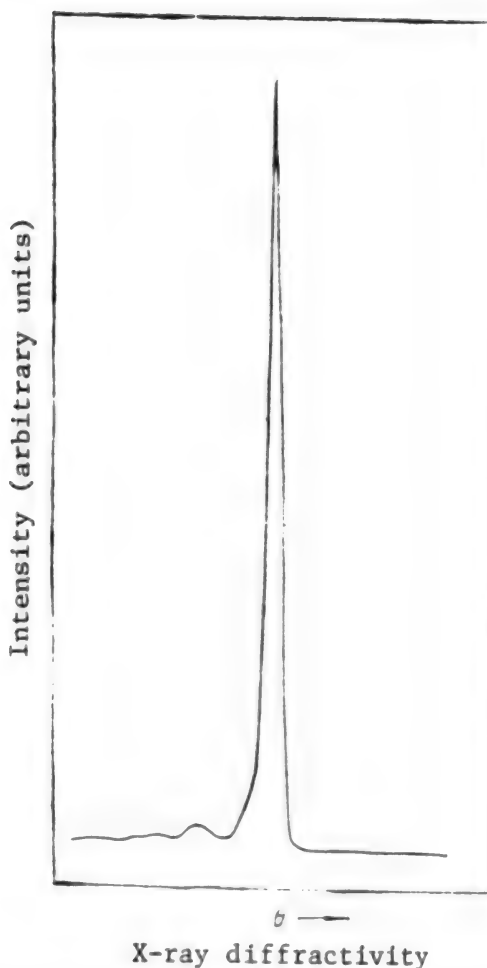


Figure 1. X-Ray Double-Crystal Diffraction Oscillation Curve for Specimen MIP-0592 of $\text{Ga}_{1-x}\text{In}_x\text{As}/\text{InP}(100)$

PL measurements were taken at 4.2 K, 10 K and room temperature. In all three types of quantum-well structures, bandgap transition has been found to move toward high energies due to the quantum-size effect. The smaller the well width, the larger the shift. Figure 2 shows the 4.2 K PL spectra of five single-quantum-well structures of different widths. Their structures are shown in the insert in Figure 2. The different well widths were measured by TEM. The thicknesses of these wells are 17 ML (1 ML = 2.93 Å) for well 1, 10 ML for well 2, 7 ML for well 3, and 6 ML for wells 4 and 5 (despite different growing times of 3 and 1 seconds, respectively). The figure shows different emission peaks corresponding to different well widths, as well as the spectral line of the $\text{Ga}_{1-x}\text{In}_x\text{As}$ reference layer on the low-energy side. It is obvious that light emission from wells 4 and 5 is near 1.123 eV. The peaks of narrower wells such as 2, 3, 4, and 5 consist of two to three peaks. This is due to the fluctuation across the width of the well.¹⁰ The narrower the well is, the easier it is to observe this fluctuation effect.

Figure 3 shows the room-temperature PL spectrum of the same specimen. Not only different emission peaks corresponding to different well widths are seen

but also the intensities are stronger. Peak I at near 1,500 nm is the strongest emission peak, with a FWHM of 28 meV. The figure shows the PL spectra of four points spaced 4 mm apart on the $5 \times 20 \text{ mm}^2$ specimen. The energy peaks and intensities are more or less consistent. This indicates that the material is very homogeneous.

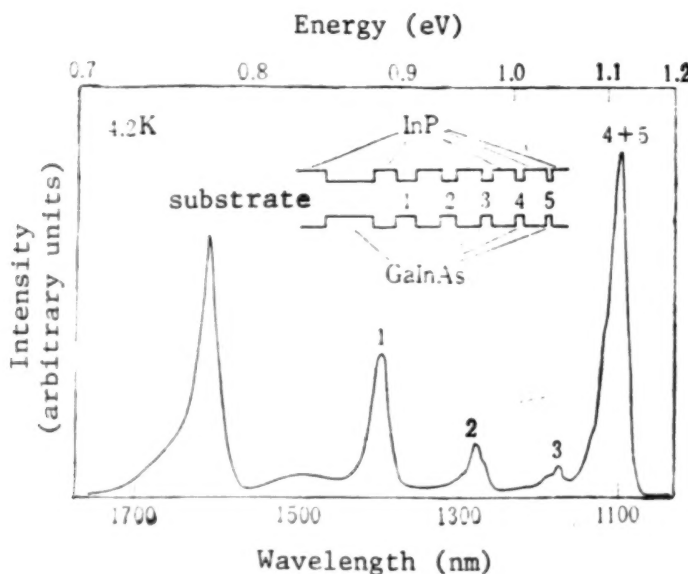


Figure 2. PL Spectrum of $\text{Ga}_{1-x}\text{In}_x\text{As}/\text{InP}$ With Multiple Single Quantum Wells (4.2 K)

PL measurements were made at 10 K with varying excitation power levels. When excitation intensity varies from 4 mW to 200 mW, light intensity increases with rising excitation intensity. Furthermore, the peak moves toward higher energies. This might be explained by the filling effect of photon-induced carriers in the sub-energy band.

Figure 4 shows the 4.2 K PL spectrum of a $\text{Ga}_{1-x}\text{In}_x\text{As}/\text{InP}$ multi-quantum-well structure with seven 21-ML-wide potential wells. It shows a heavy-hole transition with $n = 1$ (1hh). In addition, possibly due to the presence of impurities or well-width fluctuation, the spectrum also shows a weak peak and a tail on the lower-energy side. Furthermore, at room temperature the peak moves toward lower energies. However, the energy is still significantly higher than the bandgap of bulk $\text{Ga}_{1-x}\text{In}_x\text{As}$. We also measured the transmission spectrum of the same specimen at 10 K and found very sharp exciton peaks. The transition peak moves toward higher energies to 0.895 eV, in agreement with the results obtained from the PL spectra. Perhaps because the number of quantum wells is low, the classical mesa characteristic is not very apparent.

We also obtained the PL spectra of single quantum wells at 4.2 K, 10 K and room temperature and observed exciton behavior.

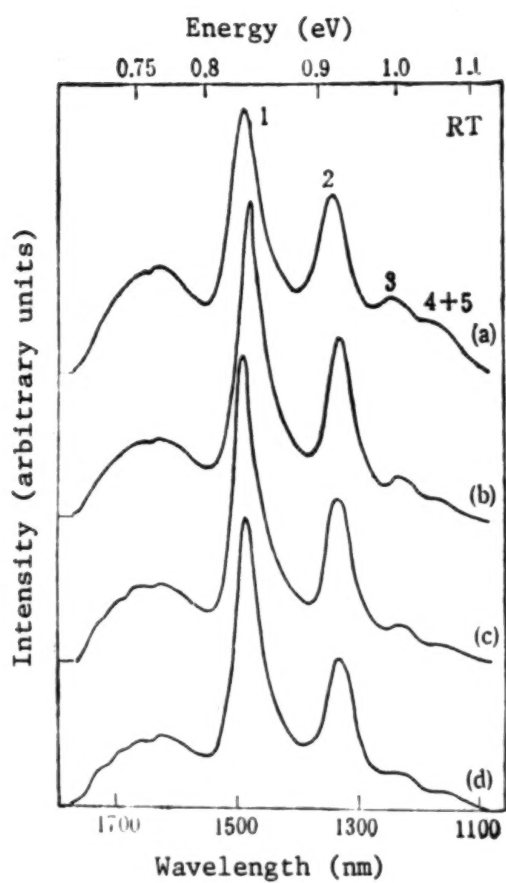


Figure 3. PL Spectra (Room Temperature) of $\text{Ga}_{1-x}\text{In}_x\text{As}/\text{InP}$ With Multiple Single Quantum Wells

Detailed analysis of the surface characteristics and optical properties of these three types of quantum well structures is in progress.

In conclusion, $\text{Ga}_{1-x}\text{In}_x\text{As}/\text{InP}$ quantum-well structures were prepared at 50 mbars using LP-MOVPE. From X-ray double-crystal diffraction, TEM, PL, and absorption measurements, these structures were found to have excellent periodicity and interface quality. Both PL and absorption spectra showed a bandgap shift toward higher energies due to the quantum-size effect.

The authors wish to thank Professor Wang Qiming [3769 0796 2494] for his encouragement and concern, the National Consolidated Laboratory for Integrated Optoelectronics, the Laboratory for Semiconductor Materials and the National Superlattice Laboratory for their support, and Wang Zhanguo [3769 0594 0948], Kong Meiyang [1313 2734 1758], Wu Ronghan [0702 2837 3352], and Zhang Jingming [1728 2417 2494] for their beneficial discussions.

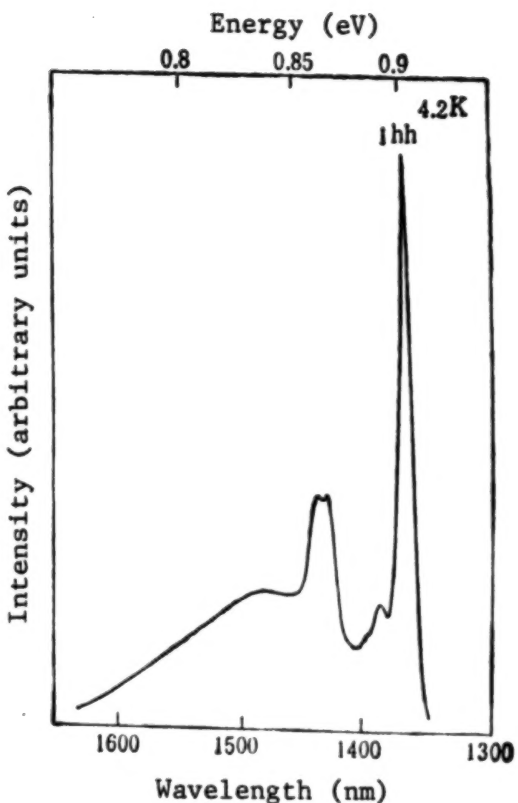


Figure 4. PL Spectrum (4.2 K) of Multi-Quantum-Well $\text{Ga}_{1-x}\text{In}_x\text{As}/\text{InP}$

References

1. M. Razeghi, J.P. Hirtz, U.O. Ziemelis, C. Delaland, B. Etienne, and M. Voos, APPL. PHYS. LETT., 43, 585 (1983).
2. D. Grutzmacher, K. Wolter, H. Jurgensen, Balk, and C.W.T. Bulle Liewma, APPL. PHYS. LETT., 52, 872 (1988).
3. W. Seifert, J.-O. Fornell, and L. Ledebo, APPL. PHYS. LETT., 56, 1128 (1990).
4. C.P. Kuo, K.L. Fry, and G.B. Stringfellow, APPL. PHYS. LETT., 47, 855 (1985).
5. B.I. Miller, E.F. Schubert, U. Koren, A. Ourmazd, A.H. Dayem, and R.J. Capik, APPL. PHYS. LETT., 49, 1384 (1986).
6. M.S. Skolnick, P.R. Tapster, S.J. Bass, N. Apsley, A.D. Pitt, N.G. Chew, A.G. Cullis, S.P. Allred, and C.A. Warwick, APPL. PHYS. LETT., 48 1455 (1986).
7. K.W. Carey, R. Hull, J.E. Fouquet, F.G. Kellert, and G.R. Trott, APPL. PHYS. LETT., 51, 910 (1987).
8. M.A. DiGiuseppe, H. Temkin, L. Petricolas, and W.A. Bonner, APPL. PHYS. LETT., 43, 906 (1983).
9. K. Kodama, M. Ozeki, and J. Komono, J. VAC. SCI. TECHNOL., B1, 696 (1983).
10. P.C. Morais, H.M. Cox, P.L. Bastos, D.M. Hwang, J.M. Worlock, E. Yablonovitch, and R.E. Nahory, APPL. PHYS. LETT., 54, 442 (1989).
11. J.H. Marsh, J.S. Roberts, and P.A. Claxton, APPL. PHYS. LETT., 46, 1161 (1985).
12. Y. Kawagnchi and H. Asahi, APPL. PHYS. LETT., 50, 1243 (1987).
13. Ph. Maurel, Ph. Bove, J.C. Garcia, and M. Razeghi, SEMICOND. SCI. TECHNOL., 5, 638 (1990).
14. H. Temkin, M.B. Panish, P.M. Petroff, R.A. Hamm, J.M. Vandenberg, and S. Sumski, APPL. PHYS. LETT., 47, 394 (1985).
15. W.T. Tsang and E.F. Schubert, APPL. PHYS. LETT., 49, 220 (1986).
16. W.T. Stacy and M. M. Janssen, J. CRYST. GROWTH, 27, 282 (1974).

- END -

END OF

FICHE

DATE FILMED

5, May 1992